ONE-DIMENSIONAL PSEUDO-HOMOGENEOUS PACKED BED REACTOR MODELING INCLUDING NO-CO KINETICS

By

Anand Srinivasan

Submitted to the graduate degree program in School of Engineering's Mechanical Engineering Department and the Graduate Faculty of University of Kansas in partial fulfillment of the requirements for the degree of Master of Science

Chairperson _____
Dr. Christopher Depcik

Committee Members _____
Dr. Ronald L. Dougherty

_____
Dr. Bedru Yimer

Date Defended: 06/30/2011

The Thesis Committee for Anand Srinivasan

Certifies that this is the approved version of the following thesis:

ONE-DIMENSIONAL PSEUDO-HOMOGENEOUS PACKED BED REACTOR MODELING INCLUDING NO-CO KINETICS

Chairperson _____
Dr. Christopher Depcik

Committee Members _____
Dr. Ronald L. Dougherty

_____
Dr. Bedru Yimer

Date Approved: 07/20/2011

ABSTRACT

The air pollution generated from mobile sources creates a large impact on the environment and on people's health. In order to meet the stringent emission regulations worldwide, aftertreatment devices are employed to reduce the toxic emissions emanating from the Internal Combustion engines in these mobile sources. In order to continually reduce emissions levels, it is essential to understand and develop more predictive aftertreatment models. Traditional devices are of the monolithic geometry consisting of small channels employing laminar flow. However, often the reaction rate expressions utilized in these models are derived from more conventional packed bed reactor experimental setups. The aim of this thesis is to develop a one-dimensional pseudo-homogeneous packed bed reactor model for this type of reactor setup built in collaboration with the Chemical and Petroleum Engineering Department at the University of Kansas. A brief summary of the pseudo-homogeneous model is presented in order to properly develop the chemical species and energy equations for dynamically incompressible flow in one-dimension. Furthermore, the chemical kinetics on the reduction reaction of nitric oxide by carbon monoxide over rhodium-alumina and platinum-alumina catalysts is investigated in detail. This is accomplished in order to validate the model using fundamentally correct reaction kinetics via a precise global reaction mechanism. Finally, parametric studies including the different model components are presented and the specific choice of model does not largely influence the conversion profiles because of the similar effective transport values. Also, it is found that a careful consideration of source terms is required to model reactions accurately.

TABLE OF CONTENTS

ABSTRACT iii

TABLE OF CONTENTS iv

ACKNOWLEDGEMENTS vii

LIST OF TABLES viii

LIST OF FIGURES ix

LIST OF APPENDICES x

NOMENCLATURE xi

CHAPTER 1 INTRODUCTION 1

1.0 MOTIVATION 1

1.1 INTRODUCTION TO PACKED BED REACTOR 2

1.2 THESIS OVERVIEW 6

CHAPTER 2 REDUCTION REACTION OF NITRIC OXIDE BY CARBON MONOXIDE OVER RHODIUM/ALUMINA CATALYSTS 9

2.0 INTRODUCTION 9

2.1 REACTION HISTORY 12

2.2 REACTION HISTORY SUMMARY 38

2.3 DETAILED REACTION MECHANISM 40

2.3.1 NO and CO Adsorption 41

2.3.2 NO Dissociation 41

2.3.3 N_2O Formation and Dissociation 42

2.3.4 CO_2 Formation 43
2.3.5 N_2 Formation 44
2.4 GLOBAL RATE EXPRESSION 44
2.5 CONCLUSION 47
CHAPTER 3 REDUCTION REACTION OF NITRIC OXIDE BY CARBON MONOXIDE OVER PLATINUM/ALUMINA CATALYSTS 49
3.0 INTRODUCTION 49
3.1 REACTION HISTORY 51
3.2 REACTION HISTORY SUMMARY 73
3.3 DETAILED REACTION MECHANISM 76
3.3.1 NO and CO Adsorption 77
3.3.2 NO Dissociation 77
3.3.3 CO_2 Formation 78
3.3.4 N_2O formation 78
3.3.5 N_2 formation 79
3.4 GLOBAL RATE EXPRESSION 80
3.5 CONCLUSION 84
CHAPTER 4 ONE-DIMENSIONAL PSEUDO-HOMOGENEOUS PACKED BED MODELING 85
4.0 HISTORY OF PSEUDO-HOMOGENEOUS CHEMICAL SPECIES EQUATION 85
4.1 CHEMICAL SPECIES EQUATION 92
4.2 HISTORY OF PSEUDO-HOMOGENEOUS ENERGY EQUATION 96

4.3 ENERGY EQUATION 102

4.4 MOLECULAR AND KNUDSEN DIFFUSIVITIES 106

4.5 EFFECTIVE DIFFUSIVITY 112

4.6 EFFECTIVE THERMAL CONDUCTIVITY 120

4.7 NUMERICAL MODELING 128

4.7.1 Stability Analysis 131

4.7.2 Initial and Boundary Conditions 134

4.7.3 Modeling Data 136

4.8 RESULTS AND PARAMETRIC STUDIES 141

4.9 CONCLUSION 152

APPENDICES 154

REFERENCES 176

ACKNOWLEDGEMENTS

First, I would like to thank, Dr. Christopher Depcik for his constant support, invaluable guidance and giving me the opportunity to work on this project. His confidence in my work and his passion towards our research drove me and influenced to accomplish my thesis.

I would also like to express my gratitude towards Dr. Ronald L. Dougherty and Dr. Bedru Yimer for serving on my graduate committee and providing valuable suggestions. Thank you very much for your constant support.

Especially, I would like to thank Sudarshan Loya for helping me in the research involved in this project and I thank my fellow lab mates Michael Magnus, Austin Hausmann, Colter Ragone, Charles Sprouse, and Eric Cecrle for their time to help me throughout my graduate studies.

Finally, I convey my gratitude to my parents, cousins and friends. I thank them for their love, unconditional support, inspiration and for all they have done for me. I dedicate this thesis to all my well wishers.

LIST OF TABLES

Table 1: Average concentrations of exhaust gas constituents during an FTP [35]..... 10

Table 2: Packed bed reactor properties and reactant properties [247-250]. 136

Table 3: Mass Biot number for packed bed reactor modeled 138

Table 4: Heat Biot number for packed bed reactor modeled 138

Table 5: NO-CO reaction kinetic parameters [248]..... 141

Table 6: Effect of discretization on the computational time and accuracy of the light-off temperature 144

Table 7: Comparison of computational time's average different diffusion models with the same effective thermal conductivity model (all models run using discretization value of six)..... 147

Table 8: Effective thermal conductivity values for different models and error percentage for NO with experimental light-off temperature 149

Table 9: Polynomial coefficients for the species in the packed bed reactor..... 154

Table 10: Values of collision diameter and epsilon ratio for calculating molecular diffusion coefficients..... 155

LIST OF FIGURES

Figure 1: Packed bed reactor illustrating pellets and active catalytic material. 3

Figure 2: TWC chemical species conversion characteristics based on A/F ratio [36] 10

Figure 3: Historical prices of platinum, palladium and rhodium adjusted for Consumer Price Index [37,38]. 11

Figure 4: Different CO bonding structures with Rh surface: (a) Single linear (b) Twin type and (c) Bridged [41]. 13

Figure 5: Different NO bonding structures with Rh surface: (a) Linear/Cationic: Rh-NO^+ (b) Bent/Anionic: Rh-NO^- (c) after introduction of oxygen to feed stream to bent form [49]. 14

Figure 6: Resulting bond structure when CO or NO is introduced to a rhodium surface covered by the other [49]. 16

Figure 7: Singular CO molecule bonded to two rhodium particles [51]. 17

Figure 8: Possible additional structures for adsorbed species over rhodium [58]. 20

Figure 9: Total emissions of NO_x worldwide from 1990 to 2000 [102]. 50

Figure 10: Historical prices of platinum per ounce based on yearly average from 1960-2010 in US dollars (plot reproduced based on the data provided) [34]. 51

Figure 11: Random pore model for a bidisperse porous solid [25]. 113

Figure 12: Heat exchange between adjacent pellets: I. Exchange by pure conduction, II. Exchange by fluid vortices in the larger interstices [176]. 123

Figure 13: Comparison between experimental and simulated (a) NO and (b) CO conversion curves vs. temperature over rhodium/alumina catalysts [Series Pore Diffusion Model and Parallel Flow Conductivity Model with discretization equal to six]. 142

Figure 14: Comparison between experimental and simulated (a) NO and (b) CO conversion curves vs. temperature over rhodium/alumina catalysts for a range of Pre-exponential factors

[Series Pore Diffusion Model and Parallel Flow Conductivity Model with discretization equal to six]..... 145

Figure 15: Comparison between experimental and simulated (a) NO and (b) CO conversion curves respectively, for Series, Parallel and Random Pore models vs. temperature over Rh/Al_2O_3 catalysts [Parallel Flow Conductivity model with discretization equal to six]..... 146

Figure 16: Comparison between experimental and simulated (a) NO and (b) CO conversion curves for Parallel, Zehner, Younis, Weighted G.M and Opris flow models vs. temperature over Rh/Al_2O_3 catalysts [Series Pore Diffusion model with discretization equal to six] 148

Figure 17: Comparison between experimental and simulated (a) NO and (b) CO conversion curves for various diffusion models versus temperature over Rh/Al_2O_3 catalyst at high SV conditions..... 150

Figure 18: Comparison between experimental and simulated (a) NO and (b) CO conversion curves for various thermal conductivity models versus temperature over Rh/Al_2O_3 catalysts at high SV conditions..... 151

LIST OF APPENDICES

APPENDIX A: CHEMKIN DATA..... 154

APPENDIX B: MOLECULAR DIFFUSION COEFFICIENT..... 155

APPENDIX C: MATLAB CODE FOR MODELING PACKED BED REACTOR 156

NOMENCLATURE

Variable	Description	Units
A	Avogadro's Number = 6.022142×10^{23}	[mol^{-1}]
A_{pb}	Surface area of packed bed	[m^2]
A_w	Reactor wall heat transfer area	[m^2]
A_1	Pre-exponential factor	[varies]
$\mathbf{Bi}_m$	Biot number for mass transfer	[-]
$\mathbf{Bi}_{w,h}$	Wall heat Biot number	[-]
$\mathbf{Bi}_{p,h}$	Pellet heat Biot number	[-]
C_m	Mean/volume averaged concentration	[mol m^{-3}]
$\bar{\mathbf{C}}$	Molar species concentration	[mol m^{-3}]
c	Constant pressure specific heat	[J kg^{-1} K^{-1}]
c	Advection number	[N m^{-2} K^{-1}]
C_r	Volumetric ratio of the heat capacities	[-]
d_b	Packed bed spherical material diameter	[m]
d_p	Pellet pore diameter	[m]
d	Diffusion number	[-]
D	Diameter of the reactor	[m]
$\mathbf{D}_m$	Molecular diffusion coefficient in a mixture	[m^2 s^{-1}]
$\mathbf{D}_{Kn}$	Knudsen diffusivity coefficient	[m^2 s^{-1}]
$\boldsymbol{D}_{ij}$	Binary molecular diffusion coefficient	[m^2 s^{-1}]
D_a	Macro pore diffusion coefficient	[m^2 s^{-1}]
D_i	Micro pore diffusion coefficient	[m^2 s^{-1}]
$\mathbf{D}_{Kn'}$	Effective Knudsen diffusion coefficient	[m^2 s^{-1}]
$\mathbf{D}_{m'}$	Effective molecular diffusion coefficient	[m^2 s^{-1}]
$\mathbf{D}_I^{eff}$	Effective dispersion coefficient	[m^2 s^{-1}]
$\mathbf{D}^{eff}$	Effective diffusivity of the species	[m^2 s^{-1}]

E_a	Apparent activation energy	[J mol^{-1}]
f	Flux of a component	[mol m^{-2} s^{-1}]
f_i	Adsorption pre-exponential constant	[atm^{-1}]
G_{ca}	Catalytic surface area per unit volume	[m^2 m^{-3}]
$\bar{\mathbf{h}}$	Molar specific enthalpy	[J mol^{-1}]
h_{fg}	Heat of vaporization of water	[kJ kg^{-1}]
h_w	Reactor wall heat transfer coefficient	[W m^{-2} K^{-1}]
h_∞	Heat transfer coefficient on outside of the reactor	[W m^{-2} K^{-1}]
ΔH	Heat of adsorption	[J mol^{-1}]
j_D , j_H	Mass transfer and heat transfer j-factors	[-]
$\boldsymbol{\kappa}$	Species mass transfer coefficient	[m s^{-1}]
k	Kinetic pre-exponent	[varies]
k_B	Boltzmann's constant	[J K^{-1}]
K	Adsorption equilibrium	[atm^{-1}]
L	Length of packed bed reactor	[m]
Lcb	Length of catalyst packed bed	[m]
L_m	Characteristic length of the pellets	[m]
L_B	Reactor bed length parallel to gas stream	[m]
Le	Length of diffusion path	[m]
L_t	Characteristic length of the reactor	[m]
MW	Molecular weight of the species	[g mol^{-1}]
Ma	Mach Number	[-]
$\dot{n}_{s\to p}$	Species mass transfer between gas and surface	[mol m^{-3} s^{-1}]
N	Diffusion rate	[mol s^{-1}]
Nu	Nusselt number	[-]
p_i	Partial pressure of the reactants	[N m^{-2}]
Pr	Prandtl number	[-]

Pe	Peclet number	[-]
$\dot{q}_{s\rightarrow p}$	Convective heat transfer between gas and surface	[W m^{-3}]
$\dot{q}_{ext}$	External heat transfer	[W m^{-3}]
$\dot{q}_{cond}$	Energy released or absorbed by condensation or evaporation	[W]
$\dot{q}_{w}$	Energy flow through wall	[W m^{-3}]
R	Radius of the packed bed reactor	[m]
$\bar{\mathbf{R}}$	Molar gaseous reaction rate	[mol m^{-2} s^{-1}]
r	Pellet radial coordinate	[m]
r_{cond}	Rate of water vapor condensation	[kg s^{-1}]
r_{e}	Equivalent pore radii	[m]
Re	Reynolds number	[-]
R_{u}	Universal gas constant	[J mol^{-1} K^{-1}]
Sc	Schmidt number	[-]
S_{g}	BET surface area	[m^{2} kg^{-1}]
t	Time	[s]
T_{ij}^{*}	Reduced temperature	[J m^{-1}]
T	Temperature of the pellets and gases	[K]
T_{∞}	Outside temperature	[K]
T_{m}	Mean temperature	[K]
u	Average bulk velocity	[m s^{-1}]
u_{s}	Gas velocity in interstitial pores	[m s^{-1}]
U	Overall heat transfer coefficient	[W m^{-2} K^{-1}]
V	Total volume of the packed bed	[m^{3}]
V_{ij}	Diffusion volume of the molecule	[m^{3}]
$\mathbf{W}$	Molecular weight of the species	[g mol^{-1}]
x	Reactor axial distance	[m]
$\mathbf{X}$	Mole fraction of species	[-]
Y	Mass fraction of species	[-]

Greek Letters:

Variable	Description	Units
α_i	Ratio of molecular weight of the species	[-]
β	Volumetric thermal expansion coefficient	[K^{-1}]
ε	Porosity	[-]
ε_{ij}	Potential wall depth	[Å]
ε_1	Macro-pore porosity	[-]
ε_2	Micro-pore porosity	[-]
$\varepsilon(r)$	Radial porosity	[-]
θ	Coverage factor of the reactants over the catalysts	[-]
λ	Pellet thermal conductivity	[W m^{-1} K^{-1}]
λ_a	Axial thermal conductivity of the solid	[W m^{-1} K^{-1}]
λ_s	Molecular thermal conductivity of fluid	[W m^{-1} K^{-1}]
λ^{eff}	Effective thermal conductivity	[W m^{-1} K^{-1}]
λ_l^{eff}	Effective axial thermal conductivity	[W m^{-1} K^{-1}]
λ_o^{eff}	Effective static thermal conductivity	[W m^{-1} K^{-1}]
$\lambda(r)^{eff}$	Effective radial thermal conductivity coefficient	[W m^{-1} K^{-1}]
μ	Dynamic viscosity	[N s m^{-2}]
ρ	Density of the pellet	[kg m^{-3}]
ρ_w	Density of reactor wall	[kg m^{-3}]
ρ_s	Density of the fluid	[kg m^{-3}]
$\overline{\rho}$	Molar density	[mol m^{-3}]
$\overline{\rho}_s$	Molar density of the fluid	[mol m^{-3}]
σ_{ij}	Reduced collision diameter	[Å]
σ	Stefan-Boltzmann constant	[W m^{-2} K^{-4}]
τ	Tortuosity	[-]

ψ	Tortuosity factor	[-]
ψ_k	Tortuosity factor for Knudsen diffusivity	[-]
Ω	Collision integral	[-]
ω, ω_s	Humidity ratio and saturated humidity ratio	[-]

Subscript:

Variable	Description	Units
i, j	Reactant species	[-]
m	mean	[-]
r	Radial	[-]
s	Bulk gas or fluid medium	[-]
p	Pellet	[-]

Superscript:

Variable	Description	Units
n	Time step	[-]

CHAPTER 1

INTRODUCTION

1.0 MOTIVATION

Internal Combustion (IC) engines produce harmful exhaust gases like carbon monoxide (CO), nitrogen oxides (NO_x), hydrocarbons (HC) and particulate matter (PM) due to incomplete combustion and high temperature dissociation of fuel, complete combustion products and air. While exhaust gas concentrations of NO_x and CO for a typical four-stroke Spark Ignition (SI) engine range only between 100 and 4000 ppm depending upon the driving conditions, temperature and air-to-fuel ratio [1,2], these species are a major concern for global air pollution as they account for around 57.6% and 38.3% of the total emissions for CO and NO_x respectively [3,4]. In the last three decades, emission regulations for IC engine exhaust have become increasingly stringent in order to preserve the environment for future generations. A major way to meet these low standards is to employ exhaust aftertreatment devices using heterogeneous catalysis for chemical species conversion. This is because the temperature is too low and the residence time is too short for chemical reactions to happen in the exhaust via a homogeneous manner.

In order to continually reduce emission levels, it becomes essential to predict the conversion properties of individual pollutants from IC engines as a function of temperature and pressure within these aftertreatment devices. The early history of exhaust cleanup in the 1970s involved the use of packed bed reactors containing aluminum spheres washcoated with noble metal catalysts. Because of durability and operation issues, industry transitioned towards

monolithic type devices consisting of a large number of small channels containing the same noble metal catalysts washcoated on the surface. However, in the laboratory setting, a large number of researchers still employ packed bed reactors when determining the chemical reactions happening on the surface of the washcoat. Moreover, collaborative efforts investigating chemical kinetics for exhaust aftertreatment between the Mechanical (ME) and Chemical and Petroleum Engineering (CPE) Departments at the University of Kansas require the creation of a packed bed model in parallel to an experimental setup in Burt Hall.

The transport of the chemical species contacting the catalytic surface plays a vital role in the design of the packed bed reactor. A complete understanding of the fluid flow distribution in a packed bed is of considerable practical importance due to its significant impact on transport phenomena and reaction rates. As a result, it is important to derive the governing equations for a packed bed reactor and provide the corresponding limitations of the model on a laboratory scale. Furthermore, since the driving force for accuracy in any heterogeneous catalyst model is proper reaction kinetics, it is necessary to review the literature in order to incorporate a proper reaction rate expression within the packed bed model.

1.1 INTRODUCTION TO PACKED BED REACTOR

The first commercial application of a packed bed reactor dates back to 1831 when Peregine Philips patented a process for making sulfur trioxide by passing air and sulfur dioxide over a relatively hot bed of platinum. As the catalyst was not consumed in the reaction, it could be used repeatedly as a continuous reactor. Since then, packed bed catalytic reactors have become one of the most often used units for gas-solid and liquid-solid reactions [5]. For example, petrochemical and oil refinery industries continue to employ packed bed reactors for a

large variety of catalytic processes such as catalytic reforming, hydro-treatment and ammonia and sulfuric acid synthesis.

As previously mentioned, the original means for controlling hazardous pollutants from automobiles involved a catalytic converter (also known as aftertreatment device) made of packed spherical pellets placed into the exhaust stream as shown in Figure 1. This device is an assembly of uniformly sized catalytic particles or pellets, which were randomly arranged and firmly held in position within a vessel or tube. The pellets were usually on the order of 3 to 6 mm in equivalent diameter in order to minimize pressure drop within the bed at the flow rates typically utilized. The reactants were supplied to the reactor with the bulk of the fluid flowing through the packed bed. Through contacting with the catalytically active particles, the reactants underwent chemical transformations, which were usually accompanied with heat release or heat consumption. If necessary, heat was removed or supplied through the walls of the device.

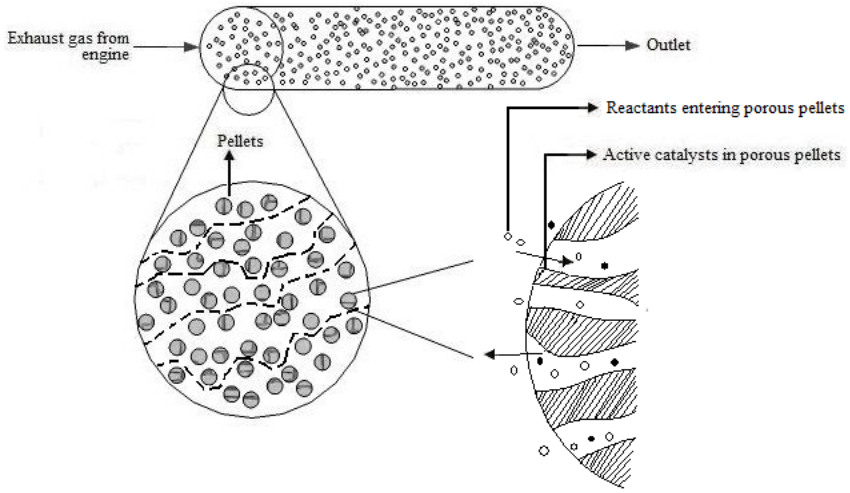

Figure 1: Packed bed reactor illustrating pellets and active catalytic material.

The degradation of this device in automobile exhaust during typical operation from vibration and temperature often resulted in pellet fracturing and plugging which caused the industry to shift to monolithic devices that are still in use today. However, a significant number of researchers still utilize packed bed reactors in the laboratory in order to formulate the chemical kinetics [6-10]. There has been a relative shift in the automotive literature towards use of monolithic reactor studies, most notably by Olsson and Anderson [11], Heck et al. [12], Harned [13] and Oh et al. [14]. Nevertheless, there exists a significant catalog of experimental data that is still useful today. In particular, as industry attempts to develop better kinetics as a function of interactions on the surface [15-22], and as indicated by efforts at KU through adaptive kinetics that include metal properties like dispersion and loading, this past data continues to provide insight [23]. As a result, it is necessary for the automotive engineer today working in the catalytic exhaust aftertreatment field to have both monolithic and packed bed reactor models available for chemical kinetics studies and utilization.

Flow modeling of packed bed reactors is a challenging task because of the difficulty of incorporating the complex geometry into the flow equations while including the interactions between fluid, pellets and walls of the reactor [24]. The packed bed reactor is a heterogeneous system composed of solid particles and fluid flowing in the interstitial space among the particle pellets [25]. The spherical porous pellets are usually made of γ-alumina, 0.2 to 0.25 inches in diameter on the laboratory scale and a Brunauer-Emmett-Teller (BET) area of 100-200 m^2/g. Manufacturers treat these pellets with stabilizers to prevent thermal sintering and add active catalytic metals like platinum, palladium and rhodium. They have relatively good crush and abrasion resistance characteristics with better pore diffusion mass transfer characteristics than monolithic type systems in order to yield high conversion rates [26].

An exact mathematical description of packed bed reactors is virtually impossible because of the interactions of fluid mechanics, heat and mass transport with chemical reactions. As a result, simplified mathematical simulations in terms of averaged flow quantities have been developed. These models are one-dimensional in nature and based upon the fundamental conservation laws of mass, momentum, species and energy. The derived versions for pelletized bed or packed bed type reactors are application specific and have their own corresponding numerical treatment [5]. Fundamentally, the result of these efforts are two types of general models; pseudo-homogeneous and heterogeneous. Research illustrates that the pseudo-homogenous model is the most commonly employed for designing packed bed reactors due to the simplifying assumptions of single phase equations utilizing effective properties for fluid and solid phases [27-29]. However, the literature is missing a thorough understanding of the assumptions presented in this model along with a summary of effective parameters.

A previous effort by Dr. Christopher Depcik thoroughly documented the one-dimensional monolithic catalyst modeling field in order to determine the correct formulation of the governing equations for this application [30]. This work follows suit in the area of one-dimensional pseudo-homogenous packed bed reactor modeling. It is important to note that a one-dimensional simplification of a monolithic or packed bed reactor may be simplistic in nature considering the device might have a significant cross-sectional area. However, it is important to understand the fundamentals of one-dimensional model first before moving into the two-dimensional realm. Secondly, as illustrated in the monolithic catalyst modeling field [31], the extrapolation of the model into a second dimension can often be done by adding only a few terms. Hence, the one-dimensional model is frequently the foundation of the two-dimensional model. Moreover, in the laboratory quite often a one-dimensional representation is sufficient, as the packed bed reactor is

often only a small core of material. The pseudo-homogeneous species and energy equations with their criteria are discussed thoroughly in Chapter 4. The importance of the various chemical kinetic parameters and their dependency in the numerical modeling of the packed bed can be understood from the chapters preceding.

1.2 THESIS OVERVIEW

The purpose of this thesis is to develop a fundamental model for a packed bed reactor in one-dimension with the previous section providing a brief history and introduction the physical and transport phenomena within this type of experimental setup (followed up in significant detail in Chapter 4). Since the accuracy of the model will be largely dependent on reaction kinetics, it is important to include an investigation into reactions occurring on the surface. The reaction chosen of NO interacting with CO is one of the more important reactions in a Three-Way Catalyst (TWC) aftertreatment device for SI engine exhaust. The exhaust from SI engines contains considerable amounts of CO and NO, and so, it becomes important to eliminate these gases in a single step through NO reduction and CO oxidation over precious catalysts in a TWCC.

Moreover, the choice of catalyst surface is important and this thesis focuses on Platinum Group Metals (PGM) because of their widespread usage within the industry. Platinum Group Metals, like platinum (Pt), palladium (Pd) and rhodium (Rh), play a vital role in providing the conversion capabilities through surface bonding and subsequent reduction in the activation energy for reactions. Hence, a review of reaction kinetics was accomplished in order to obtain a fundamental understanding of the detailed reactions on rhodium/alumina (Rh/Al_2O_3) and platinum/alumina (Pt/Al_2O_3) catalysts with alumina being the standard washcoat material for TWC devices.

As a result, Chapter 2 provides a comprehensive review of NO reduction by CO over Rh/Al_2O_3 catalysts that has been published by the author [32]. This review describes the major reaction steps involved in the reduction reaction under a wide range of temperature and concentration conditions. This is necessary as SI and Compression Ignition (CI) engines have different compositions and exhaust temperatures, which may lead to different rate determining steps over the catalyst. As a result, distinctive global mechanisms are required to satisfy both low and high temperature conditions in order to give aftertreatment models the required accuracy.

Similarly, Chapter 3 involves a theoretical investigation of the NO reduction reaction by CO over Pt/Al_2O_3 catalysts [33]. Similar to Rh, the optimization of Pt metal loading over alumina substrate is very important due to the cost involved into the manufacturing of catalytic converters [34]. In addition, since aftertreatment devices contain a mixture of PGM components, the review of both Pt and Rh versions of the NO and CO reaction will help future researchers develop a more predictive model for metal combinations. The outcome of this research is the formulation of a detailed kinetic mechanism that relies heavily on the previous research in order to indicate the main steps in the process. From the detailed reaction steps, the authors create a global kinetic mechanism that will simulate this reaction better than the current versions utilized in the aftertreatment modeling literature.

Chapter 4 begins with a review of the literature for one-dimensional (1-D) pseudo-homogeneous packed bed modeling by examining heat and mass transport properties. As a result, a general packed bed model with appropriate species and energy equations is developed in order to model reaction kinetics on a laboratory scale. Finally, the author concludes by presenting a parametric study using the NO-CO reduction reaction over Rh/Al_2O_3, illustrating the influence of model components and transport parameters. Furthermore, this thesis includes a

summary of various factors influencing the model in order to describe how to formulate a two-dimensional packed bed simulation (radial effect) based upon this work. It is important to note that the chapters in this thesis are self-contained with respect to writing as they are intended to be (or have already been) submitted to journals for possible publication.

CHAPTER 2
REDUCTION REACTION OF NITRIC OXIDE BY CARBON MONOXIDE OVER RHODIUM/ALUMINA CATALYSTS*

2.0 INTRODUCTION

The hazardous emissions from industrial, commercial and personal activities are one of the biggest challenges faced by scientists for improving air quality. Of the various sources, on-road vehicle use accounts for a significant part of the problem with 2002 Environmental Protection Agency (EPA) levels indicating that carbon monoxide (CO) and nitrogen oxides (NO_x) emissions, account for 57.6% and 38.3% respectively of the total emissions of each variety [3,4]. Over the past two decades, emissions produced from automobiles are of great concern because of their impact on human health and the environment. Emission regulations set by governments across the world have made a considerable impact in reducing problematic species and continue to be set lower as researchers meet and exceed current standards. However, these increasingly stringent regulations are becoming a technological challenge for the automotive companies.

Of particular importance, the Three Way Catalyst (TWC) for Spark Ignition (SI) engines has had a significant impact on reducing both NO_x and CO emissions. Unlike Compression Ignition (CI) engines, SI engine exhaust contains enough CO, along with hydrocarbons (HC) and hydrogen (H_2), to act as a reductant for the NO_x emissions as indicated in Table 1.

* This chapter has been published as: Srinivasan, A., & Depcik, C. (2010). Review of chemical reactions in the NO reduction by CO on rhodium/alumina catalysts. Chem. Rev. Sci. Eng., 52, 462-493.

Table 1: Average concentrations of exhaust gas constituents during an FTP [35].

HC	NO_x	CO	H_2	CO_2	O_2	H_2O
750 ppm	1050 ppm	0.68 vol%	0.23 vol%	13.5 vol%	0.51 vol%	12.5 vol%

A second catalyst then oxidizes any remaining CO, HC, and H_2 by using the remaining oxygen and secondary air injection. Through this combination of reduction and oxidation catalysts, the TWC has a well-known conversion curve as shown in Figure 2 [36]. Near stoichiometry, each chemical species has relatively high conversion rates.

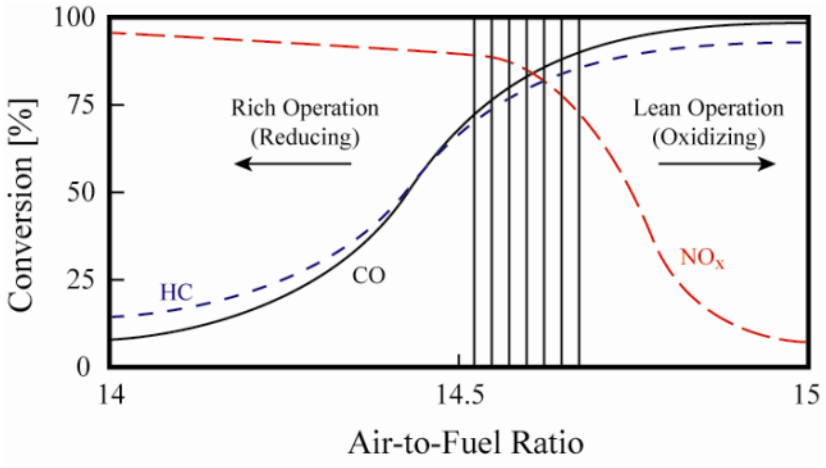

Figure 2: TWC chemical species conversion characteristics based on A/F ratio [36]

In the reduction catalyst, Platinum Group Metals (PGM) like platinum (Pt), palladium (Pd) and rhodium (Rh) play a vital role in providing the conversion capabilities. While these metals make up only a small amount of the washcoat, they contribute significantly to the catalyst cost as indicated in Figure 3. Manufacturers adjust catalyst loading to take into account market fluctuations while trying to achieve the same reducing capabilities. However, rhodium plays a vital role by enhancing NO_x conversion capabilities and helps in the suppression of ammonia

(NH_3) emissions at rich conditions. In the past, researchers have found rhodium to be one of the best catalysts to serve this dual purpose. Since it is significantly more expensive than the other metals, manufacturers weigh its use against the needed conversion potential.

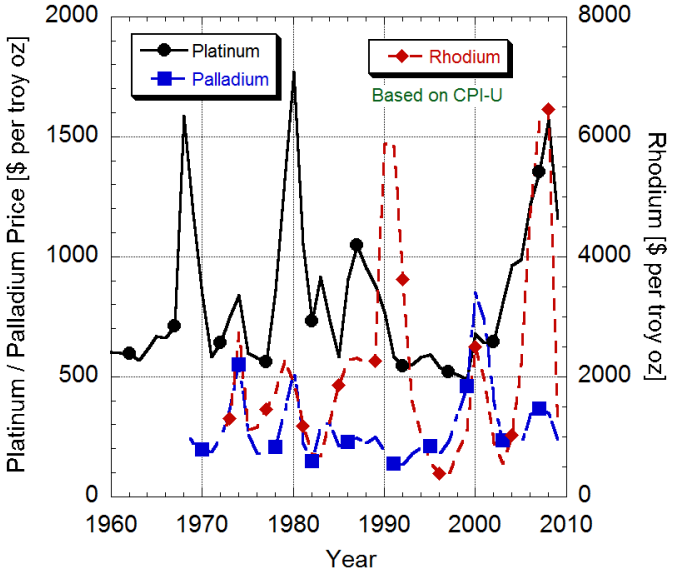

Figure 3: Historical prices of platinum, palladium and rhodium adjusted for Consumer Price Index [37,38].

As a result, TWC models must predict correct mechanism rates in order to give users the ability to minimize the amount of rhodium being utilized. With respect to the literature, one-dimensional based catalyst models tend to follow the lead of Montreuil et al. [39] and Koltsakis et al. [31] in simulating NO_x reduction reactions. These reactions resulted from an early effort by Voltz et al. [40] and act more as an extension to the model rather than a fundamental study of the reaction and its associated global mechanism.

In order to make models more accurate and predictive [23], this paper researches the history of the NO and CO reaction over rhodium to determine a better global kinetic mechanism for incorporation which requires an understanding and an explanation of the history of the

detailed reactions occurring on the surface as this mechanism leads to the global formulation through the rate-determining step. This reaction mechanism occurred in the absence of other species such as hydrogen and hydrocarbons in order to provide a clear focus of efforts. The result is a global reaction rate expression that will simulate this reaction better than the current versions in the aftertreatment literature.

2.1 REACTION HISTORY

In 1957, Yang and Garl were among the first to study the NO-CO reaction over rhodium by investigating CO bonding to the surface [41]. Through Infrared (IR) exploration, they found three different gas-metal bonding structures: 1), a singular CO molecule bonding to the surface (single linear); 2) two CO molecules bonding to a singular Rh (twin type); and 3) three CO molecules interacting with two Rh surface sites (bridged). Of the types illustrated in Figure 4, the linear and bridged versions are most common and will shift towards the linear form as the coverage of CO increases. They also state that the twin type CO reacts with O_2 even when heated at partial coverage; however, the linear and bridged CO reacts at room temperature at both low and high coverage.

Fifteen years later, Bauerle et al. published an important paper for automotive applications by studying the reduction of NO by CO in the presence of oxygen on copper-based and noble metal catalysts [42]. The impact of oxygen on the reaction is important because the leaner an engine can run with excess O_2 available during combustion, the more thermodynamically efficient the engine and the better the fuel economy. In addition, since most engines were of the carbureted variety in this decade, fuel-air ratios could vary dramatically during operation, requiring catalysts to be more robust. They found that the conversion of NO over Rh was virtually unaffected by O_2 concentrations up to a certain level (2500 ppm) whereas

ruthenium (Ru) and platinum (Pt) started producing nitrous oxide (N_2O) at lower levels of O_2 of about 1250 ppm. In addition, lowering temperatures did not reduce NO conversion capabilities at higher concentration levels of oxygen. This work indicates the necessity of rhodium as a preferred metal in the catalysis of SI engine exhaust.

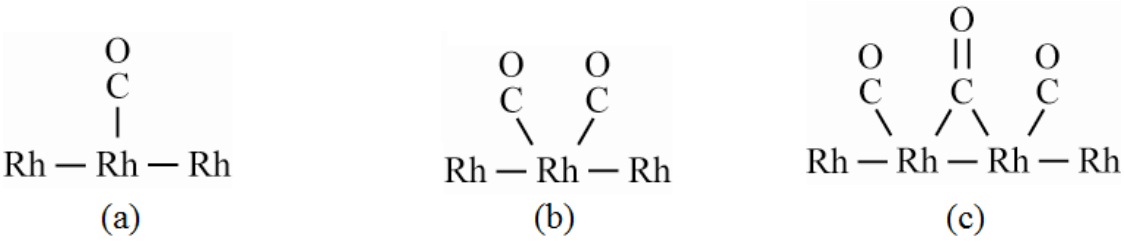

Figure 4: Different CO bonding structures with Rh surface: (a) Single linear (b) Twin type and (c) Bridged [41].

In 1974, Uland and Barker researched the impregnation of rhodium catalysts with ruthenium for use under reduced conditions (excess fuel) in an automotive exhaust stream [43]. The result of their efforts showed that alumina washcoat (γ-Al_2O_3) catalysts incorporating low levels of Rh were highly effective in NO_x removal. However, one drawback of the conversion process was the tendency to produce ammonia (NH_3) under rich conditions [44] which is particularly important to note as a number of diesel aftertreatment systems under current development utilize this reaction to produce ammonia over a Lean NO_x Trap (LNT) for later Selective Catalytic Reduction (SCR) devices [45-47].

In the same year, Kobylinski compared the reduction of NO by hydrogen and carbon monoxide over the major Platinum Group Metals; Rh, Pt, Ru and Pd [48]. His studies revealed that the rhodium catalysts have a higher activity of NO reduction by utilizing CO rather than H_2. He found that when H_2 is utilized as a reducing agent, the activity sequence for the reduction capability is Pd > Pt > Rh > Ru whereas for CO the sequence is reversed. Moreover, the

formation of NH_3 over Rh ceases around 590°C, indicating possible reconversion back to full combustion products; however, for Pt and Pd, significant ammonia formation was observed even at 790°C.

In 1976, Hiromichi and Hiroo studied NO/CO adsorption and bond strength over an alumina-supported rhodium catalysts [49]. They found that NO is adsorbed in two forms; cationic ($Rh{\cdot}NO^+$) in a linear angle structure (180°) and anionic ($Rh{\cdot}NO^-$) in a bent angle structure (120°) as illustrated in Figure 5. Through an x-ray study of these compounds, both the Rh·N and N·O bonds of the cationic structure were stronger than the bonds of the anionic structure. Upon introducing oxygen to the feed stream, the $Rh{\cdot}NO^-$ bond strength decreases rapidly, and the adsorbed NO reacts to form a bidentate nitrato structure as shown in Figure 5. Under lean conditions, the frequency of this structure decreases and does not contribute to the reaction mechanism. In addition, they validated the three different CO bonding structures determined twenty years earlier by Yang and Garl [41].

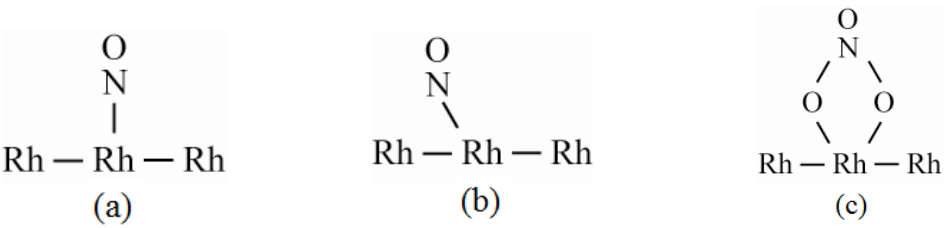

Figure 5: Different NO bonding structures with Rh surface: (a) Linear/Cationic: Rh-NO^+ (b) Bent/Anionic: Rh-NO^- (c) after introduction of oxygen to feed stream to bent form [49].

They experimentally observed that the twin type CO bonding structure reacts with oxygen at elevated temperatures and remains inactive at temperatures below 100°C. However, the linear and bridged CO structures react readily with oxygen at 25°C because the coordination site for adsorption of O_2 remains at the metal atom. Since Rh has the capability to have one more molecule on its surface, the latter structures have a greater probability towards oxygen

adsorption. Thus, the linear and bridged CO structures oxidize relatively easily to create CO_2. Of particular importance, when introducing either CO or NO to a rhodium surface covered with other associated species in linear form, Hiromichi and Hiroo found that the same bonding structure results as illustrated in Figure 5.

These results suggest that the pre-absorbed cationic structure of NO changes to the anionic structure when CO is introduced, indicating a localized interaction of CO and NO species. Both the linear and bridged type CO molecules on the surface interact with the gaseous NO to form this dual-bonded structure ($NO \cdot Rh \cdot CO$) as shown in Figure 6 whereas the twin CO remains unchanged and does not interact with the gaseous NO species. From these observations, they proposed an Eley-Rideal (E-R) mechanism where the pre-adsorbed NO and CO reacts with gaseous CO and NO, respectively:

$CO + Rh \underset{k_{-1}}{\overset{k_1}{\rightleftarrows}} Rh \cdot CO$	(1)
$NO + Rh \underset{k_{-2}}{\overset{k_2}{\rightleftarrows}} Rh \cdot NO$	(2)
$NO + Rh \cdot CO \xrightarrow{k_3} CO_2 + \frac{1}{2} N_2 + Rh$	(3)
$CO + Rh \cdot NO \xrightarrow{k_4} CO_2 + \frac{1}{2} N_2 + Rh$	(4)

In this case, when CO and NO are both present in the dual bonded structure ($NO \cdot Rh \cdot CO$), they react instantaneously and go to completion. Hiromichi and Hiroo also proposed a potential pathway of intermediate NCO and N_2O production during the NO and CO conversion process from the dual bonded structure due to local interactions.

$NO + Rh \cdot CO \xrightarrow{k_5} Rh \cdot N + CO_2$	(5)
$CO + Rh \cdot N \xrightarrow{k_6} Rh \cdot NCO$	(6)

$NO + Rh \cdot N \xrightarrow{k_7} Rh + N_2O$	(7)

where, NCO was found to be stable up to 400°C under vacuum.

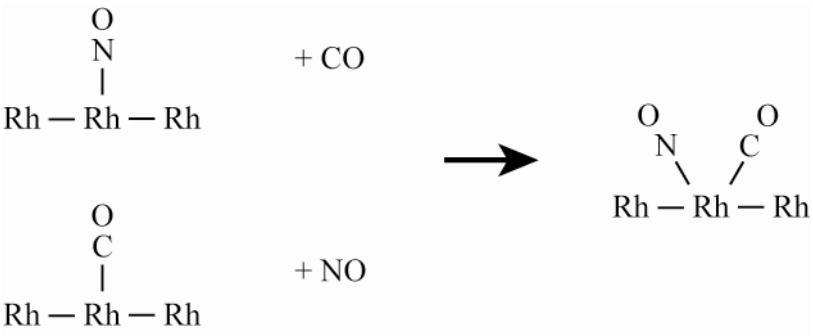

Figure 6: Resulting bond structure when CO or NO is introduced to a rhodium surface covered by the other [49].

In 1978, Campbell and White suggested the first detailed kinetic mechanism over polycrystalline rhodium using Flash Desorption Spectroscopy (FDS) determined under steady-state measurements at 3.2 x 10^{-11} bar [50]. They showed that NO adsorbs with a high initial sticking probability which then dissociates during heating to form N_2 and O_2 species. Two peaks were found for nitrogen formation, illustrating nitrogen desorption and the disproportional reaction between NO and N. Their model infers that N_2 forms from mono-atomic adsorbed N or the disproportional reaction and starts with adsorption via Eqns. (1) and (2) followed by:

$Rh \cdot NO + Rh \xrightarrow{k_8} Rh \cdot O + Rh \cdot N$	(8)
$2Rh \cdot N \xrightarrow{k_9} 2Rh + N_2$	(9)
$Rh \cdot NO + Rh \cdot N \xrightarrow{k_{10}} Rh \cdot O + Rh + N_2$	(10)
$Rh \cdot CO + Rh \cdot O \xrightarrow{k_{11}} 2Rh + CO_2$	(11)

In the same year, Kroeker et al. used tunneling electron spectroscopy measurements to further validate the three forms of chemisorbed CO over alumina-supported rhodium [51]. From

their thermal desorption experiments at 10^{-5} torr CO pressure, they determined that the bridging bond is the strongest (75 meV) followed by single linear CO (58.1 meV) and twin linear species (51.6 meV). In addition, they provided a summary of observed mode positions and indicated the presence of one additional configuration of a singular CO molecule bonded to two rhodium particles as indicated in Figure 7.

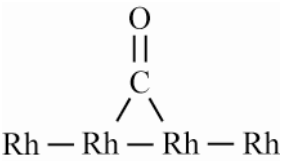

Figure 7: Singular CO molecule bonded to two rhodium particles [51].

Concurrent to these results, Solymosi and Sarkany performed infrared spectroscopic studies at temperature ranging from 25 to 400^{o}C and observed almost the same range of bands for adsorbed NO and CO over Rh/Al_2O_3 confirming earlier work by other researchers [52]. In addition, these bands indicate the presence of an isocyanate complex with its formation sensitive to the composition of the reacting gas mixture. The formation of NCO occurs when the reacting gas mixtures are at high temperatures or with excess NO and Rh^- sites. At high temperatures, they speculate that the formation of NCO occurs through Eqn. (6) and the formation of CO_2 follows an E-R mechanism which occurs through the reduction of oxidized rhodium by CO as given in Eqn. (12).

$CO + Rh \cdot O \xrightarrow{k_{12}} Rh + CO_2$	(12)
$2Rh + NO \underset{k_{-13}}{\overset{k_{13}}{\rightleftarrows}} Rh \cdot N + Rh \cdot O$	(13)

Under excess NO, they postulate another E-R mechanism for the formation of NCO via Eqn. (13) and Eqn. (6). At temperatures above 100°C, the formation of CO_2 occurs via active NO·Rh·CO complexes,

$CO \cdot Rh \cdot NO \xrightarrow{k_{14}} Rh \cdot N + CO_2$	(14)

in which the adsorbed Rh·N follows Eqn. (6) to produce an isocyanate complex.

At the turn of the decade, Yates et al. investigated the dissociation phenomenon of chemisorbed CO [53]. According to their auger spectroscopic and isotopic exchange measurements, at a surface temperature below 800 K, the maximum probability of dissociation of CO molecules in collision with Rh_{111} is approximately 10^{-4}. Hence, they conclude that the probability of the dissociation of CO is negligible when compared to the disassociation of the molecular desorption of CO and therefore rule out the dissociation of CO on Rh during the reaction kinetics. At the same time, Baird and Wynblatt suggested that CO chemisorbs and desorbs molecularly at all coverages over Rh_{110} which is experimentally supported by their Temperature Programmed Desorption (TPD) curves and Ultraviolet Photoelectron Spectroscopy (UPS) studies [54], whereas, NO chemisorbs dissociatively at low coverage (150 to 500 ppm) and molecularly at high coverage (500 to 1500 ppm). In these studies, NO desorbs from Rh_{110} at 340°C and 195°C for low and high coverage, respectively, while the remaining atomic nitrogen desorbs at 250°C.

In the same year, Dubois et al. found from their electron energy loss spectroscopy measurements that oxygen occurs as an intermediate in the formation of CO_2 and N_2 over Rh_{311} [55]. Adsorbed NO dissociates at 450K, which is well below catalytic converter operating temperatures of 600 to 800K. Due to this reaction, they presume N_2 formation follows via Eqn. (9). They ignore the disproportional reaction of Eqn. (10) in contrast with Campbell and White's

model [50]. In addition, since they find oxygen desorbing above 700K, they state that the formation of gaseous CO_2 over the catalyst occurs through Eqn. (12). Two years later, Worley et al. studied the importance of the support material [56]. They show that the nature of this material is quite important in CO chemisorption behavior and is more pronounced when alumina (Al_2O_3) is used as a substrate rather than silica or kaolinite.

In 1984, Edward and Robert investigated NO adsorption using IR studies to determine the effect of oxygen in the formation of the isocyanate complex and nitrous oxide over Rh/Al_2O_3 [57]. At high temperatures, they found that the reaction follows an E-R scheme where rhodium reacts with gaseous NO to give N_2O as a product, and the remaining adsorbed oxygen acts as an inhibitor.

$Rh \cdot NO + NO \underset{k_{-15}}{\overset{k_{15}}{\rightleftarrows}} NO \cdot Rh \cdot NO$	(15)
$Rh + 2NO \xrightarrow{k_{16}} Rh \cdot O + N_2O$	(16)
$Rh \cdot O + NO \underset{k_{-17}}{\overset{k_{17}}{\rightleftarrows}} O \cdot Rh \cdot NO$	(17)

Their experimental studies correlate with the results of Baird et al. [54] but are contrary to the results of Dubois et al. [55] since their IR study illustrates that the oxygen formed on the surface inhibits further reactions until 873K when oxygen desorbs. Furthermore, they proposed a detailed reaction mechanism for the formation of NCO through Eqns. (14), (6) and the formation of CO_2 under high CO partial pressures with Rh·NCO as an intermediate:

$Rh \cdot CO + NO \underset{k_{-18}}{\overset{k_{18}}{\rightleftarrows}} Rh \cdot NO + CO$	(18)
$Rh \cdot NO + 2Rh \cdot CO \xrightarrow{k_{19}} Rh \cdot NCO + CO_2$	(19)

Moreover, N_2O formation does not begin with Eqn. (8); instead, it follows Eqn. (14) that further reacts with gaseous NO to form N_2O. They did not observe N_2O in the absence of CO in the feed stream.

A few years later, Hendershot and Hansen recommended possible reactant structures over Rh_{100} crystals as illustrated in Figure 8 [58]. Under low energy electron diffraction and thermal desorption spectroscopy studies, they found that the adsorbed CO and NO species self-inhibit their reaction rate as their partial pressure increases. They determined that the kinetic order of CO in the reaction varies from +1 to -1 when CO partial pressure increases from 1 to 250 Pa at constant NO partial pressure. Similarly, the kinetic order for NO varies from +3/2 to -1 when the NO partial pressure increases from 1 to 1800 Pa at a constant CO partial pressure.

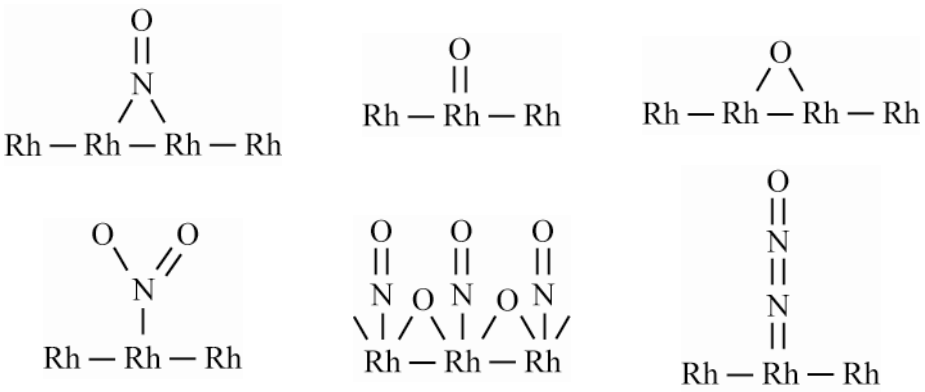

Figure 8: Possible additional structures for adsorbed species over rhodium [58].

In addition, they introduce a new L-H reaction mechanism with the traditional adsorption steps; Eqns. (1) and (2) followed by:

$2Rh \cdot NO \underset{k_{-20}}{\overset{k_{20}}{\rightleftarrows}} Rh \cdot O + Rh \cdot N_2O$	(20)

$Rh \cdot N_2O + Rh \cdot CO \xrightarrow{k_{21}} 2Rh + N_2 + CO_2$	(21)
$Rh \cdot NO + Rh \cdot O \underset{k_{-22}}{\overset{k_{22}}{\rightleftarrows}} Rh \cdot NO_2 + Rh$	(22)
$Rh \cdot NO_2 + Rh \cdot CO \xrightarrow{k_{23}} 2Rh + NO + CO_2$	(23)
$2Rh \cdot NO \underset{k_{-24}}{\overset{k_{24}}{\rightleftarrows}} NO \cdot Rh \cdot NO + Rh$	(24)

In the above reaction mechanism, the oxidation of CO via adsorbed oxygen does not appear because the reaction rate with CO was determined to be negligible compared to oxidation via the NO pathway.

In 1988, Dictor proposed a reaction scheme based on a number of experimental conclusions over Rh/Al_2O_3 [59]. Starting with NO, he states that NO dissociates readily on a reduced rhodium surface via Eqn. (8) rather than an oxidized surface through the formation of isocyanate which forms immediately after the introduction of CO to the pre-adsorbed NO sites as in Eqn. (6). In contrast, isocyanate formation does not occur when NO is introduced to pre-adsorbed CO which differs from the results of the Solymosi and Sarkany studies [52]. Moreover, the linear and bridged CO structures are suppressed in the presence of NO, suggesting that the interaction of NO and CO occurs on a contiguous rhodium surface and not on isolated sites. The NO molecules adsorb as a neutral or net negatively charged species which later becomes a slightly positive charge due to electron withdrawing effect of oxygen atoms over rhodium as in Eqn. (1). The rhodium surface reduces when CO oxidation removes oxygen atoms from the surface through an E-R mechanism. This result proves that the oscillating effect, from reduced state to oxidized state, occurs as the function of the oxygen content over the surface.

Dictor also report that there is no experimental data to support the formation of $Rh \cdot NO_2$ or $NO \cdot Rh \cdot CO$ as part of the reaction mechanism.

In the next few years, Fisher et al. were among the first to study the reaction kinetics under transient conditions over Rh_{111} [60-63]. Their Temperature Programmed Desorption spectra at transient conditions showed similar results to Campbell and White with N_2O formation considered negligible in both Ultra High Vacuum (UHV) and moderate pressure conditions. Their model assumes nitrogen desorption as the rate-limiting step, and their reaction mechanism is similar to the Campbell and White model [50] which involves a modified L-H mechanism using surface reactions Eqns. (1), (2), (8), (9) and (11) and results in the following global rate equation at low p_{CO}/p_{NO} ratios:

$\bar{\mathbf{R}} = \dfrac{kK_{CO}p_{CO}}{\left(1+K_{CO}p_{CO}\right)^2}$	(G1)

where k is the rate constant and K_{CO} is the adsorption equilibrium constant for CO: $K_{CO} = k_1/k_{-1} = A_{CO}e^{-\Delta H_{CO}/(R_u T)}$.

A year later, Carballo et al. proposed a reaction mechanism over noble metal catalysts operating at 250 to 600^{o}C and 10^{-5} to 10^{-3} mbar total pressure through Eqns. (1), (2), (8) and (11) while adding:

$2Rh \cdot NO \underset{k_{-25}}{\overset{k_{25}}{\rightleftarrows}} N_2 + 2Rh \cdot O$	(25)
$Rh + N_2O \underset{k_{-26}}{\overset{k_{26}}{\rightleftarrows}} N_2 + Rh \cdot O$	(26)

and neglecting N_2O formation [64]. They found that the formation of N_2O is significantly lower than the formation of nitrogen and carbon dioxide between 400 and 1000K. Since gaseous N_2O is an important greenhouse gas, it is imperative to understand the conditions at which N_2O forms.

The occurrence of N_2O as a reaction intermediate in the reaction over Rh/Al_2O_3 was discussed by Cho et al. in 1989 [65]. Their results under steady feed and cyclic conditions suggest that the formation of N_2O is an important intermediate step, and they propose an overall reaction scheme in which the formation of N_2 and CO_2 is dominant at high temperatures with a stoichiometric composition. In the case of low temperatures and reduced conditions, N_2O becomes an intermediate in the reaction. Based on their observations, N_2O occurs at relatively high concentrations of NO, and the oxygen produced in the reaction initiates the surface reaction Eqn. (11) to form CO_2 under the light-off temperature:

$\mathrm{Rh \cdot NO + Rh \cdot N \xrightarrow{k_{27}} Rh \cdot N_2O + Rh}$	(27)
$\mathrm{Rh \cdot N_2O \underset{k_{-28}}{\overset{k_{28}}{\rightleftarrows}} N_2O + Rh}$	(28)
$\mathrm{Rh \cdot N_2O \xrightarrow{k_{29}} N_2 + Rh \cdot O}$	(29)

In addition to the above three equations, their overall reaction mechanism includes Eqns. (1), (2), (8), (9) and (11). Hence, below the light-off temperature, the rate of oxygen production via NO decomposition controls the overall reaction rate while oxygen scavenging from the surface via CO oxidation influences conditions above the light-off temperature.

The decade of the 1990s saw the beginning of an in-depth analysis of the detailed reaction mechanism. Anderson et al. demonstrated the plausible modes of adsorbed NO_2 over Rh as it undergoes self-ionization to NO^+ and NO_3^- [66]. According to the Solymosi and Sarkany [52] scheme previously mentioned, the $Rh \cdot NO^+$ species formed experience a reversible

reaction to form the $NO \cdot Rh \cdot CO$ structure and in turn remove carbon monoxide in accordance with the expectation of a weak $Rh \cdot CO$ and a strong $C \cdot O$ bond:

$NO \cdot Rh \cdot NO + NO \xrightarrow{k_{30}} Rh \cdot NO + Rh \cdot O + N_2O$	(30)
$2Rh + NO_2 \xrightarrow{k_{31}} Rh \cdot NO + Rh \cdot O$	(31)
$Rh \cdot NO + Rh \cdot O + NO_2 \xrightarrow{k_{32}} Rh \cdot NO + Rh \cdot NO_3$	(32)
$Rh \cdot NO + Rh \cdot O + CO \underset{k_{-33}}{\overset{k_{33}}{\rightleftarrows}} NO \cdot Rh \cdot CO + Rh \cdot O$	(33)

One year later, the dissociation reaction of the Campbell and White studies are again verified through Bowker et al.'s TPD studies [67]. Their measurements show that the N_2 desorption from Rh_{110} occurs only after NO dissociation in the presence of oxygen atoms or after the removal of oxygen by CO through a "clean off" reaction. The rate of CO_2 production was determined to be much lower than the oxygen reaction, except at extreme temperatures. This is because NO competes with CO for surface sites during steady-state and transient experiments and deposits oxygen atoms more efficiently.

Around this time, as emission standards increased, researchers began enhancing the conversion rate of NO by modifying dispersion, metal loadings and including additives. In 1993, Donald and Constance investigated the effect of Rh dispersion over alumina under cyclic reducing and oxidizing conditions at relatively high temperatures [68]. Under these conditions, Rh particles were recovered from their oxidized state in the form of large metal particles. For an oxidization reaction, they suggest that the highly dispersed Rh is less active than a larger Rh particle. The Rh particle migration was found to have a low sintering order (between 1.6 to 4.7) because of the strong bond between the rhodium catalyst and the alumina substrate. They present a model for sintering in their paper; however, it is beyond the focus of this work.

The developements in the early 90's paved the way to use different kinds of rhodium structutres to improve kinetic rates. Baraldi et al. investigated the rate of NO dissociation with respect to the variation in the rhodium crystal structures using mass spectrometry, TPD and LEED measurements [69]. They found that the rate of N_2 production at 460 to 510K correlates well with the Rh_{110} structure and the rate of CO_2 production is maximum because of loosely bonded oxygen to the rhodium catalyst. Above 670K, the variations in the reaction rate and surface structure are governed only by oxygen, and the rate of N_2 production is maximum when oxygen begins regulating the restructuring of the substrate.

Similar to Donald et al. [68], Kaspar et al. studied the effect of the rhodium dispersion by using Temperature Programmed Desorption (TPD) measurments [10]. From their studies, the dispersion effect depends upon the operating temperture of rhodium catalysts. Above 500K, reductive agglomeration of the rhodium particle occurs, and the TPD peaks shift significantly towards higher values as dispersion increases from 22% to 42%. Illustrating that NO dissociation is promoted by an increase of metal particle size.

In the same year, Byong again looked at the role of N_2O as an intermediate over Rh/Al_2O_3 [70]. With reference to earlier results, it was found that when N_2O interacts with CO on the surface, the reaction occurs twice as fast. However, they found that the sticking coefficient of N_2O under typical reacting conditions is very small (in the order of 2×10^{-6}), and thus the rate-limiting step in the reaction could be the adsorption of N_2O over Rh which contradicts most of the earlier research. Moreover, they calculate the activation energy for N_2O decomposition as 18 kcal/mol which is much larger than the decomposition for N_2O desorption at 6 kcal/mol. The rate of N_2O dissociation increases with an increase in temperature and space velocity through N_2O readsoprtion as the formation shifts right with respect to temperature. In

addition, they state that Rh/Al_2O_3 produces N_2O between 150 to 300°C, but this formation contradicts with their reactor experiment N_2O conversion rate results. Concurrently, Shelef and Graham report the importance of rhodium as the reduction material in a three-way catalyst [15]. It was found that CO oxidation by O_2 was insensitive towards rhodium dispersion whereas the NO dissociation rate was sensitive to the particle size and dispersion.

In 1995, Belton et al. proposed a reaction mechanism using Eqns. (1), (2), (8), (9), (10), (11), (27), (28) and (29); however, reactions Eqns. (2), (10), (11) and (27) were considered only in their experimental studies over Rh_{111} [71]. Through UHV studies, their results do not illustrate the formation of N_2 as a product through Eqn. (10); instead, only N_2O is formed. Thus, the disproportionation reaction between adsorbed NO and N did not appear to occur. They observed that the surface must be saturated with NO in order to form N_2O; with the increase in N coverage, the N + N step is faster than the NO desorption or dissociation via Eqn. (9). It is found that there is no evidence for N_2O readsorption in the reaction mechanism.

In the same year, Charles et al. investigated the selectivity of N_2 and N_2O at relatively high pressures ranging from 1 to 100 torr over Rh_{110} and Rh_{111} surfaces [72]. Their experimental studies suggest that the selectivity towards N_2 is greater than N_2O for Rh_{110} due to more open surfaces whereas Rh_{111} shows more selectivity towards N_2O (70% formation at all experimental conditions) because of the steric crowding of adsorbed NO inhibiting NO dissociation. This result corresponds to low N_2 coverages which increases N_2O formation. It was found that N_2O formation is sensitive towards rhodium surface structures; however, with respect to the activity of the $NO \cdot CO$ reaction, both structures have similar NO consumption rates. The Rh_{110} surface does exhibit a lower apparent activation energy over a wide range of temperatures and pressures than the Rh_{111} surface due to a more facile NO dissociation process.

With continued advances in computing efficiency, Zhdanov and Kasemo in 1996 extrapolated the rate equations from ultra-high vaccum data to atomsperic pressures [73]. They proposed a reaction mechanism with Eqns. (1), (2), (8), (9), (10) and (11) based on their Temperature Programmed Desorption measurements. Their results indicate that nitrogen desorption is the rate-limiting step and N_2O formation is not significant when utilizing the Oh et al. model [60-63]. Their experimental results were in poor agreement with their model because the calculated apparent activation energy for equal NO and CO partial pressures was 53 kcal/mol whereas the measured value was 32 kcal/mol. However, they suggest potential changes to the scheme to obtain better validation for the experimental data; changing the coverage dependence of the activation energies, introducing more than one type of adsorption sites or neglecting NO decomposition at high coverages.

In addition to their earlier works, Belton and Permana provided an in-depth study of the species coverage dependence on the reaction rates over Rh_{111} [74]. They found that below 635K, N_2O formation was favored and NO molecules dominate the surface whereas, above 635K, N_2 formation was preferred and CO is the major surface species. From their kinetic experiments, they show that N_2O readily converts to N_2 when the temperature is less than 700K, and NO coverage plays a key role in determining the activity and selectivity over the catalyst. When the temperature is greater than 623K, N_2 formation rises sharply as a result of the increase in the coverage of nitrogen atoms due to a decrease in NO coverage through desorption and N_2O formation reduces rapidly. Based on their results, they propose a reaction mechanism via Eqns. (1), (2), (11), (13), (27), (28) and (29) while ignorning the recombination of atomic nitrogen step nitrogen via Eqn. (9). At higher temperatures or at lower NO partial pressures, the N_2O production kinetics are overwhelmed by the NO desorption reaction. Thus, the selectivity of the

N_2O reaction is largely based on the competition between the NO + N reaction and NO desorption. Moreover, N_2O readsorption is neglected as described in the earlier work of Belton et al. [71].

In the same year, Zhdanov summarized nitrous oxide findings and determined that the mechanism suggested by Cho et al. is not supported [75]. According to Cho et al. [65], N_2O readsorption plays an important role in the formation of nitrogen which contradicts the experimental results of Belton et al. [74] as well as Zhdanov's own experimental results. Moreover, McCabe and Wong [76] and Belton et al. [74] have shown that the N_2 formation rate from the N_2O and CO reaction is negligibly low compared to the rate in the NO and CO reaction.

From 1990, Permana et al. investigated the effect of oxygen at moderate pressures (lower than 100 torr) using Reflection Absorption Infra Red Spectroscopy (RAIRS) measurements over Rh_{111} [77]. Their work resulted in the addition of one more detailed kinetic step to their earlier model:

$O_2 + Rh \xrightarrow{k_{34}} 2Rh \cdot O$	(34)

It is shown that the NO and CO coverage was unaffected by the addition of stoichiometric oxygen under 675K; i.e. oxygen is not adsorbed by rhodium effectively as compared to NO or CO, and thus it does not impact their coverage factors. In this case, the rate of CO_2 production increases by a factor of approximately four. Moreover, the production rates of N_2O and N_2 are unaffected under lean conditions, and the NO consumption rate is independent of the presence of oxygen. From the RAIRS experiments under 700K, the addition of oxygen increases the CO_2 formation rate without affecting the NO consumption rate or the N_2O selectivity which supports Oh and Carpenter's earlier results [60-63].

In 1997, Novak et al. studied the variations on the rhodium structure during CO adsorption and found that rhodium has only one adsoption band due to a quick oxidative disruption reaction [78]. As a result, it is important to stabilize rhodium dispersion under catalytic conditions with low reductive agglomerization. In the same year, Teuvo et al. corroborated the importance of rhodium as a catalyst in a three-way catalytic converter by finding that the rhodium decreases the formation of ammonia in rich conditions, and it is more active in the initiation of the $NO \cdot CO$ reaction and N_2O decomposition [79]. Their experimental results show that the rate of N_2O formation depends upon the amount of NO coverage.

Concurrently, Zhdanov and Kasemo presented the first review of the detailed reaction mechanism of NO and CO kinetics under 10^{-7} torr of ultra high vacuum and around 8 torr of moderate pressure conditions over Rh_{111} [80]. From their TPD and LEED results, they concluded that the adsorption and desorption behavior of CO and NO depends upon their sticking coefficients and coverage. Specifically, the sticking coefficient and activation energy decreases with an increase in coverage, and the temperature dependence of the sticking coefficient for CO on Rh was found to be relatively weak. Furthermore, NO decomposition occurs only when it has a nearby empty neighbor site. They found that the NO molecule desorbs at 400K whereas molecular nitrogen desorbs at 430K. Their transient exchange experiments indicate that the oxidation of CO proceeds via an L-H mechanism consisting of Eqns. (1), (2), (8), (9) and (11). They found that the NCO formed in the reaction scheme decomposes even at 150K, and therefore they omitted its incorporation. Their model follows the Charles et al. [74] mechanism and neglects the possibility of N_2O formation in the system under UHV conditions. They discovered that at moderate pressures and temperatures lower than 800K, NO primarily covers the surface, and correspondingly, NO dissociation was chosen as the rate-limiting step.

In 1998, Granger et al. investigated the catalytic reactions for the removal of NO in the presence of NH_3, CO and H_2 [17]. They report that the turnover frequency of NO increases as the dispersion of rhodium on the surface decreases from 100% to 1.7%. The increase of the Rh loading from 5.84% to 11.21% caused a rapid decrease in the turnover frequency of NO, relating to the earlier efforts of Kasper et al. [10] which indicate that an increase in the rhodium particle size enhances the reaction rate.

In the same year, Chuang and Tan suggested the formation of different products from the same adsorbed species based on unique states of rhodium over an alumina substrate [81]. As a result, the state of the rhodium (whether Rh^0 or Rh^+) can be determined based on these products as shown here (superscript '+' and '–' sign corresponds to the oxidized and reduced site of Rh atoms):

$NO + Rh^0 \underset{k_{-35}}{\overset{k_{35}}{\rightleftarrows}} Rh^0 \cdot NO^-$	(35)
$Rh^0 \cdot NO^- + Rh^0 \underset{k_{-36}}{\overset{k_{36}}{\rightleftarrows}} Rh^0 \cdot N + Rh^0 \cdot O$	(36)
$Rh^0 \cdot NO^- + 2Rh^0 \underset{k_{-37}}{\overset{k_{37}}{\rightleftarrows}} (Rh)_2 O^{2-} + Rh^0 \cdot N$	(37)
$Rh^+ + 2CO \underset{k_{-38}}{\overset{k_{38}}{\rightleftarrows}} Rh^+ (CO)_2$	(38)
$Rh^+ + NO \underset{k_{-39}}{\overset{k_{39}}{\rightleftarrows}} Rh \cdot NO^+$	(39)
$Rh \cdot NO^+ + 2CO \underset{k_{-40}}{\overset{k_{40}}{\rightleftarrows}} Rh(CO)_2 + NO$	(40)
$Rh \cdot CO + (Rh^+)_2 O^{2-} \overset{k_{41}}{\rightarrow} 3Rh^0 + CO_2$	(41)
$Rh^+ (CO)_2 + 2Rh \cdot O \overset{k_{42}}{\rightarrow} 2Rh^+ + 2CO_2$	(42)

$Rh \cdot NO^{-} + Rh^{0} \cdot N \xrightarrow{k_{43}} 2Rh^{0} + N_2O$	(43)
$2Rh^{0} \cdot N \xrightarrow{k_{44}} 2Rh^{0} + N_2$	(44)
$Rh^{0} \cdot N + Rh \cdot CO \xrightarrow{k_{45}} Rh^{0} + Rh \cdot NCO$	(45)

Under lean conditions, they found that the oxygen adsorbs over Rh and reacts with the adsorbed $Rh^{+}(CO)_2$ species to produce CO_2 and $Rh \cdot NO^{-}$ which dissociates to form adsorbed nitrogen and oxygen. In addition to the reaction mechanism suggested above, it was observed that the adsorbed oxygen from air reacts with $Rh \cdot NO^{+}$ at 473K, producing a nitrato species $Rh(NO_3)$ that is reversible and provides more rhodium sites for the $NO \cdot CO$ reaction. When the species react above 473 K, the adsorbed oxygen reacts with Rh^{+} (CO_2), producing CO_2 and thus blocks the reduced Rh^{0} sites for $Rh \cdot NO^{-}$ because it oxidizes Rh^{0} and Rh^{+} to Rh^{2+} sites and inhibits the NO conversion and N_2O formation.

In 1998, Kiss et al. investigated the stability of NCO under lean conditions using RAIR spectrum measurements over Rh_{111} at 5×10^{-10} mbar [82]. Their results indicate that pre-adsorbed oxygen atoms result in an increase in the relative amount of NCO formation. However, at high temperatures and low concentrations, the NCO species have a shorter lifetime and fully decompose around 300K. They found that adsorbed oxygen atoms enhance its stability by 60K. At the same time, Cant et al. studied the formation kinetics of nitrous oxide [16]. Their result shows the highest amount of N_2O (370 ppm) formation below 400K, and as the temperature increases, N_2O formation rapidly decreases. Throughout this process, ammonia formation over rhodium is very small (30 ppm). In addition, they suggest that N_2O production increases with catalyst aging due to the sintering of rhodium particles at high temperatures.

In the following year, Herman et al. compared Rh_{100} crystals with their earlier results over Rh_{110} and Rh_{111} of partial pressures at 8 Torr [83]. They found that the formation and selectivity towards N_2O remains similar irrespective of the crystal structure, depending mainly upon NO partial pressure. In addition, between 150 and 500K, the turnover number for NO over Rh_{100} is between Rh_{110} and Rh_{111}, and thus the activity of the overall reaction is Rh_{110} > Rh_{100} > Rh_{111} which is inversely related to their surface atomic density.

One year later, Chuang et al. investigated the reactivity of $Rh^{+}(CO)_2$ during $CO \cdot O_2$ and $CO \cdot NO$ reactions over Rh/Al_2O_3 [84]. With respect to their earlier efforts, $Rh^{+}(CO)_2$ remains inactive towards gaseous NO and the oxidization of CO. This species requires sufficient Rh^0 and Rh^+ sites to initiate the redox reaction. In this paper, $Rh^0 \cdot NO^-$ is reported to dissociate, producing N_2 and Rh^+ sites for the formation of $Rh^{+}(CO)_2$. Any available CO reduces Rh^+ to Rh^0 which forms CO_2 and leads to the dissociation of NO molecules. The proposed reaction scheme follows Eqns. (1), (35), (37) and includes:

$4CO + \left(Rh^+\right)_2 O^{2-} \underset{k_{-46}}{\overset{k_{46}}{\rightleftarrows}} 2Rh^+ \left(CO\right)_2 + O^{2-}$	(46)
$2Rh^+ \left(CO\right)_2 + O^{2-} \underset{k_{-47}}{\overset{k_{47}}{\rightleftarrows}} 2Rh^0 \cdot CO + CO_2 + CO$	(47)
$Rh^+ \left(CO\right)_2 + NO \underset{k_{-48}}{\overset{k_{48}}{\rightleftarrows}} Rh \cdot NO^+ + 2CO$	(48)
$Rh^0 \cdot CO + NO \underset{k_{-49}}{\overset{k_{49}}{\rightleftarrows}} Rh^0 \cdot NO^+ + CO$	(49)

At the same time, Zaera and Gopinath supported the results of Cho et al. [65] by suggesting the presence of N_2O as an intermediate in the reduction of NO using molecular beam experiments over Rh_{111} [18]. They found the formation of N_2O through an NO+N reaction and not by N+N+O or NO+NO reactions. In addition, they suggest that the recombination of

nitrogen atoms does occur at low temperatures, and N_2 formation from NO does not appear to involve a direct $N \cdot NO$ interaction.

In 2001, Bustos et al. studied the overall kinetics using a lattice-gas model and Monte Carlo algorithm over Rh_{111} and provide a new reaction model with Eqns. (1), (2), (8), (10), (11) and the following [85]:

$Rh \cdot NO + Rh \cdot N \underset{k_{-50}}{\overset{k_{50}}{\rightleftarrows}} Rh \cdot NO \cdot N + Rh$	(50)
$NO + Rh \cdot N \overset{k_{51}}{\rightarrow} Rh \cdot NO \cdot N$	(51)
$Rh \cdot NO \cdot N \overset{k_{52}}{\rightarrow} Rh + N_2O$	(52)

Their experimental results show that the recombination of nitrogen atoms is not responsible for the reduction of NO over Rh; instead, an intermediate species $(Rh \cdot NO \cdot N)$ forms.

In the same year, Harmsen et al. investigated NO reduction by CO under the presence and absence of oxygen using transient experiments at 1.1 bar total pressure [86]. Their results indicate that chemisorbed CO does not react directly with chemisorbed NO and N_2. Moreover, N_2O formation occurs only after NO dissociation and the presence of oxygen inhibits its production. Concurrently, Zaera and Gopinath investigated the kinetics over Rh_{111} under lean conditions [87]. They found that at low temperatures (less than 550K), the kinetics of NO reduction by CO does not differ; the rate of NO reduction by CO is six times faster than the rate of the oxidation reaction of CO. At high temperatures above 600K, the inhibition effect of the adsorbed oxygen species decreases through Eqn. (12) and thus increasing the rate of production of nitrogen. However, the rate of the $CO \cdot NO$ reaction is much faster than the $CO \cdot O_2$ interaction. As a result, they infer that oxygen does not inhibit the kinetics of NO reduction by CO.

In the following year, Baumer et al. looked at the structural sensitivity of CO dissociation over Rh crystals [88]. They found that the dissociation of CO is easier on a stepped surface like Rh_{211} rather than a flat surface like Rh_{111}. Their experimental results show that CO cannot dissociate on Rh_{111}, but it may dissociate under a stepped structure or through defects on the surface. One year later, concurrent with the results of Baumer et al. [88] and Zaera et al. [87], Loffreda et al. investigated the chemisorption and dissociation of NO over different Rh crystals by using the density field theory (DFT) [89]. They found that the dissociation rate depends upon the Rh structure, and the activity order given has $Rh_{100} > Rh_{511} > Rh_{111}$ with the dissociation rate highest on a Rh_{100} open surface because it has the lowest activation energy barrier as compared to the closely packed Rh_{111} surface. In addition, they propose a detailed scheme for NO molecular dissociation by starting with a stable molecular adsorption through Eqn. (2), then through a metastable precursor state towards a transition state in which the energy difference between these two states gives the effective activation energy for dissociation via Eqn. (8).

In 2005, Avalos et al. proposed a reaction model based on their experimental results and Monte Carlo simulations over Rh_{111} [90]. Their scheme follows Eqns. (1), (2), (8), (11), (51) with an additional reaction:

$Rh \cdot NO \cdot N \xrightarrow{k_{53}} Rh \cdot O + N_2$	(53)

They state that in the above scheme, N_2 forms via the $Rh \cdot NO \cdot N$ intermediate species through dissociation of adsorbed NO, and the reaction rate depends upon the coverage factor. In other words, NO dissociation increases with an increase in vacant sites previously mentioned by Zhdanov and Kasemo [80]. They neglect the E-R reaction between the adsorbed nitrogen atom and gaseous NO because they find that nitrogen production from the $Rh \cdot NO \cdot N$ intermediate is faster than the classical recombination step of nitrogen atoms.

One year later, Granger et al. studied the kinetics over Rh and Pt catalysts using TDP measurements [91]. They proposed reaction schemes for the $NO \cdot CO$ interaction and N_2O dissociation. Their $NO \cdot CO$ scheme follows Eqns. (1), (2), (3), (8), (9), (10), (11) while including one additional reaction to account for N_2O formation:

$\mathrm{Rh \cdot NO + Rh \cdot N \xrightarrow{k_{54}} 2Rh + N_2O}$	(54)

They suggest that the dissociation of adsorbed NO is the rate-determining step with their corresponding rate expression given as:

$\overline{R}_{\mathrm{NO}} = \dfrac{kK_{\mathrm{NO}} p_{\mathrm{NO}}}{\left(1 + K_{\mathrm{NO}} p_{\mathrm{NO}} + K_{\mathrm{CO}} p_{\mathrm{CO}}\right)^2}$	(G2)

Where, k is the rate constant for NO dissociation and K_{CO} and K_{NO} are the equilibrium adsorption constants: $K_{\mathrm{NO}} = k_2 / k_{-2} = A_{\mathrm{NO}} e^{-\Delta H_{\mathrm{NO}}/(R_u T)}$.

The N_2O dissociation mechanism follows Eqns. (1), (11) and the following new reactions:

$\mathrm{Rh + N_2O \underset{k_{-55}}{\overset{k_{55}}{\rightleftarrows}} Rh \cdot N_2O}$	(55)
$\mathrm{Rh \cdot N_2O + Rh \xrightarrow{k_{56}} Rh + Rh \cdot O + N_2}$	(56)
$\mathrm{Rh \cdot N_2O + Rh \xrightarrow{k_{57}} Rh \cdot N_2 + Rh \cdot O}$	(57)

with the corresponding global rate expression:

$\overline{R}_{\mathrm{N_2O}} = \dfrac{kK_{\mathrm{N_2O}} p_{\mathrm{N_2O}}}{\left(1 + K_{\mathrm{N_2O}} p_{\mathrm{N_2O}} + K_{\mathrm{CO}} p_{\mathrm{CO}}\right)^2}$	(G3)

Where, k is the rate constant for N_2O dissociation and $K_{\mathrm{N_2O}}$ is the equilibrium adsorption constant: $K_{\mathrm{N_2O}} = k_{55} / k_{-55} = A_{\mathrm{N_2O}} e^{-\Delta H_{\mathrm{N_2O}}/(R_u T)}$. They determined that N_2O dissociates more readily on Rh/Al_2O_3, and the strong attraction of NO to the Rh surface prevents the readsorption of N_2O.

They found a rapid decrease in N_2O selectivity above the NO light-off temperature, and NO conversion is highest for Rh, followed by Pt/Rh and then Pt.

At the same time, Ricart et al. investigated the competitive decomposition of N_2O over Rh_{111} [92]. They found that N_2O adsorbs through Eqn. (55) without any distortion; i.e., no changes in their bond length and chemical structure after adsorption. It then dissociates into two possible adsorbed species: NO+N or N_2+O. The preferential decomposition process of N_2O is the formation of N_2 rather than NO because of the low adsorption energy of N_2. Hence, they infer that N_2 is the main product from the reduction of NO over Rh, and N_2O is only a minor factor.

In the following year, Granger et al. compared the utilization of Platinum Group Metals with respect to the conversion characteristics of NO reduction by CO/H_2 under UHV conditions [19]. They found that the order of the activity sequence for NO reduction by CO is equal to Rh/Al_2O_3 > Pd/Al_2O_3 > Pt/Al_2O_3 with their rate determining step considered to be the dissociation of NO molecules over the rhodium site. In addition, the formation of N_2O during NO reduction by CO over rhodium was lower in comparison to the other two metals. Their proposed mechanism follows reactions (1), (2), (8), (9), (10), (11), (54) and they give the following reaction but neglect it in their final summary:

$2Rh \cdot NO \xrightarrow{k_{58}} N_2 + 2Rh \cdot O$	(58)

Moreover, they observed a lack of ammonia formation over Rh/Al_2O_3 during the NO+H_2 reduction reaction.

As nano-technology continues to improve, Dent et al. in 2007 investigated the interaction of NO and CO species over rhodium nano-particles [93]. They illustrate that rhodium nano-particles corrode significantly at low temperatures (below 473K) to form $Rh \cdot NO^+$ and

$Rh(CO_2)$, respectively. Here the corrosion of rhodium metal means the substantial dispersion of nano-particulate rhodium to mononuclear rhodium sites. In addition, as the temperature of the catalytic bed increases, aggregation becomes more favored and the CO-NO redox reaction becomes more efficient. They propose an E-R mechanism that follows Eqns. (3) and (4) and suggest that the reaction Eqn. (3) is kinetically twice as fast as reaction Eqn. (4).

Recently, Na-Ranong et al. studied the steady state kinetics under periodic operations with a concentration of NO ranging from 500-2000 ppm and 1000-6000 ppm for CO [20]. According to the power rate law the reaction orders obtained for CO and NO over Rh were 0 and 0.396 (positive values) whereas the reaction order for CO over Pt is negative (-0.7) [94], implying that the CO self-inhibiting effect over Rh is weaker than the effect on Pt and the reaction rate inhibition due to strongly adsorbed CO; NO is insignificant. They propose a reaction mechanism that follows Eqns. (1), (2), (9), (54) and include the following reactions in accordance with their experimental results:

$CO + Rh \cdot NO \xrightarrow{k_{59}} Rh \cdot N + CO_2$	(59)
$Rh \cdot CO + NO \xrightarrow{k_{60}} Rh \cdot N + CO_2$	(60)

This reaction scheme is of the E-R type, including reversible NO and CO adsorption and rapid consumption of the $NO \cdot Rh \cdot CO$ structure; i.e., Eqn. (14) is much faster than its formation. In addition, they neglect the NO dissociation step because their experimental operating temperature is below 450K and refer to Dubois et al. who state that NO dissociation does not occur below this temperature [55]. From their previous results, the formation of the isocyanate complex and $Rh \cdot (CO_2)$ are not considered in their reaction scheme. Their rate-limiting step in their reaction scheme is the recombination of nitrogen atoms. In addition, they found a higher selectivity of

N_2O compared to N_2 under the light-off temperature; hence they consider the N_2O formation step in the rate expression.

2.2 REACTION HISTORY SUMMARY

Research began for the NO and CO reaction over rhodium in the late 1950s. Early efforts focused on the adsorption profile of both CO and NO molecules. Based on IR measurements, researchers found multiple structures for both species without singular preferred alternatives. In addition, they started investigating the advantages of rhodium over other PGMs like platinum and ruthenium [41]. It was found that rhodium is an important catalyst for NO reduction, and it minimizes the production of ammonia under rich conditions [43,44]. In addition, lean conditions do not appear to affect the kinetics with high conversion rates maintained [42].

The physical properties and the bond strength of the adsorbed species based on these chemical structures provided vital information for the initiation of detailed reaction mechanisms. Based on three forms of NO adsorption and four CO structures [49], researchers initially believed that the scheme follows an E-R type mechanism through Eqns. (3) and (4) with stable NCO formation [49]. However, a comprehensive detailed kinetic scheme proposed by Campbell and White instead supported an L-H mechanism without NCO formation [50]. While other researchers backed the E-R version with stable NCO formation [49,51], later work showed that this species is highly unstable [80].

In the early 1980s, researchers began to explore the reaction kinetics with respect to emission regulations. The dissociation of CO was found to be negligible compared to NO [53,54] and researchers maintained the use of an E-R mechanism because of the oxygen desorption at high temperatures [55]. Furthermore, the alumina substrate became a preferred

washcoat material because of its efficient CO chemisorption ability [56]. In the mid 1980's, NO and CO kinetics began to include N_2O species because their formation was found to be high during rich conditions [57]. Researchers started using both E-R and L-H mechanisms to explain the kinetics based on their oxygen and N_2O investigations [55,57,58,61,65]. With the increasing emphasis on greenhouse gases, Cho et al. described a detailed kinetic mechanism with N_2O as a reaction intermediate and proposed a modified L-H mechanism involving its formation [65,70]. From their results, they suggest that N_2O dissociation increases with an increase in temperature because of its higher activation energy.

Early in the 1990s, kinetics examination began based on dispersion, metal loadings, metal particle size and the catalyst face structure. During an oxidation reaction, highly dispersed particles are less active than larger rhodium particles [67,69]. In addition, a loosely packed structure has the highest tendency for CO_2 conversion [68]. It was also suggested that rhodium dispersion was insensitive to CO oxidation, but the NO dissociation rate was sensitive to particle size and dispersion [15]. Moreover, NO dissociation increases by an enlargement in the particle size [10] and open structures like Rh_{110} increase the production of nitrogen whereas closed face structures like Rh_{111} boost N_2O formation due to its inhibition of NO dissociation [71,83]. Furthermore, Belton et al. suggested a scheme for N_2O formation by neglecting the traditional N_2 disproportional reaction [71]. Other researchers indicate that oxygen influences the selectivity of N_2O and NO while NCO formation is instable at temperatures above 150K [41,74,77,83] .

Recent work targets accurate measuring techniques to study the NO turnover rate with respect to dispersion and metal loading. This rate was found to increase with a decrease in dispersion and an increase in metal loading which corroborates the earlier results [10,17]. In-depth studies illustrate that NO dissociates easily over reduced rhodium particles which occurs in

the presence of CO [81]. In addition, experimental data show that N_2O formation occurs only after NO dissociation while oxygen does not inhibit the NO reduction rate which validates earlier results [18,86]. In this decade, most researchers describe the reaction kinetics through an L-H mechanism by assuming negligible N_2O production above a NO light-off temperature, and there is an increase in NO dissociation with more vacant rhodium sites [41,85,88,91,95]. As the price of rhodium rose exponentially, a comparative study was made which revealed that the formation of N_2O and NH_3 was lower as compared to platinum and palladium catalysts [19]. Moreover, N_2O is a minor product compared to N_2 because of the rapid decrease in N_2O production after 400K [16,92]. Recently, with the development of nano-technology, researchers found that rhodium nano-particles easily oxidize at low temperatures (around 473K) [93]. In addition, E-R mechanisms are still being considered with negligible N_2O formation above the NO light-off temperature and more selectivity towards N_2O under this temperature [20,93].

2.3 DETAILED REACTION MECHANISM

Based on the analysis presented in the previous section, the author feel that NO reduction by CO over rhodium occurs via the following steps:

- NO and CO Adsorption
- NO Dissociation
- N_2O Formation and Dissociation
- CO_2 Formation
- N_2 Formation

In this mechanism, the formation of NCO is neglected because the detailed reaction mechanism described here is for operating temperature conditions of catalytic converters, and it is known from the history of the reaction mechanism that NCO is unstable above 150K over

Rh_{111} [80]. In addition, the adsorption of oxygen molecules is considered to be relatively small as compared to CO and NO adsorption, and the mechanism neglects its use [67,77,95]. Moreover, the formation of $Rh(CO_2)$ is not considered in the reaction mechanism since it reacts rapidly with chemisorbed oxygen atoms generated from NO dissociation [84]; also, diffusion of the reacting species over the surface is negligible [20].

2.3.1 NO and CO Adsorption

The first step in the detailed reaction mechanism is the adsorption of the reacting species over rhodium. The sticking coefficients of the species NO and CO are found to be high and dependent on both temperature and composition [95]. The initial sticking coefficients of NO and CO were found to be 0.7 to 0.8 and 0.68, respectively [96,97]. Moreover, the sticking coefficients for both species increase with a decrease in coverage [41], and thus the coverage dependence on the reaction rate should be considered [71]. With an increase in temperature, there is also an increase in the sticking coefficient along with a decrease in the NO adsorption energy. Concurrently, the sticking coefficient of CO decreases [95], suggesting that NO is more likely to adsorb rather than CO. Thus the first step towards the detailed reaction mechanism follows Eqns. (1) and (2).

As for a bonding angle, researchers found that adsorbed NO frequently forms a bent structure (anionic) with weak NO bonds [49] while adsorbed CO is equally likely to form a linear or twin structure [41,59].

2.3.2 NO Dissociation

The dissociation of NO is considered to be the second step in the reaction mechanism which follows Eqn. (8). Adsorbed NO in its bent structure dissociates easily at temperatures above 450K at low coverages [54]. For compression ignition exhaust having low NO tailpipe

concentrations, this phenomenon is indeed true; however, NO may not dissociate on the surface under typical spark ignition exhaust conditions which contain a higher amount of NO and result in elevated coverages [54]. In this case, the dissociation characteristic changes with an increase in the temperature and vacant sites [90]. Because of the switching nature of this equation based on NO concentration, some authors consider this reaction the rate-limiting step [54]. In addition, researchers also believe NO dissociation is slow in spite of this low dissociation energy because of the high dispersion of rhodium over the alumina substrate, making it difficult for NO molecules to find vacant sites and dissociate [61,62,80,90,91].

2.3.3 N_2O Formation and Dissociation

Researchers usually neglect the formation of N_2O or include it via a separate pathway different from the detailed reaction mechanism. After reviewing the previous work, the authors consider that it is reasonable to include N_2O formation under the following conditions. The formation of N_2O occurs at temperatures around 400K which is below the NO light-off temperature. The amount will increase with a rise in NO coverage because of the inhibition of the NO dissociation reaction [57,70,71,86,95]. Unlike Bustos et al. [85], the authors consider that N_2O forms via an L-H mechanism as given in Eqn. (27) at high temperatures and there is no ready adsorption of N_2O gas via an E-R mechanism because of its high adsorption energy as compared to NO and CO species.

Gas phase N_2O is not an intermediate in NO-CO kinetics for the production of nitrogen, and N_2O dissociates even at low temperatures of about 60K over a clean rhodium surface [97], serving as a precursor to the dissociative adsorption of N_2O forming N_2 and O atoms [76,98]. Moreover, the dissociation rate increases with a raise in temperature [70,92]. The authors

consider the dissociation reaction of N_2O into nitrogen molecules and oxygen atoms because of the strong terminal bond of the oxygen with rhodium as provided in Eqn. (56).

According to Oh et al., the N_2O desorption rate is slow compared to the rate of N_2O formation [61]. However, Byong et al. [70] consider the reversible desorption reaction with low desorption energy whereas other authors neglect the N_2O desorption step and state that dissociation is relatively fast [18,61,65,92]. Since N_2O formation can be found in the exhaust stream, the authors include this step but for lower temperatures. Considering the fact that N_2O desorption energy is less than the dissociation with respect to Byong et al. [70] and dissociation increases with an increase in temperature, the authors consider an additional reaction without subsequent readsorption of N_2O molecules from the gas:

$\mathrm{Rh \cdot N_2O \xrightarrow{k_{61}} Rh + N_2O}$	(61)

These desorption and dissociation steps are still controversial when reviewing the history of N_2O studies.

2.3.4 CO_2 Formation

The oxygen formed during the dissociation reactions of NO and N_2O is considered stable on the surface, but in the presence of CO it reacts rapidly to form CO_2 through an E-R mechanism [49,51,62] as presented in Eqn. (12). Furthermore, the authors consider that the intermediate $\mathrm{CO \cdot Rh \cdot NO}$ forms at temperatures around 373K [20,49,52,59,66]. According to Hiromichi and Hiroo along with Na-Ranong et al., NO·Rh·CO formation occurs via the previously bonded CO or NO pathways [20,49]:

$\mathrm{CO + Rh \cdot NO \xrightarrow{k_{62}} CO \cdot Rh \cdot NO}$	(62)
$\mathrm{NO + Rh \cdot CO \xrightarrow{k_{63}} CO \cdot Rh \cdot NO}$	(63)

The authors present both steps in spite of the higher sticking coefficient of NO, leading to a higher surface coverage of NO.

Due to the strong attraction between CO and the weaker NO bond [49,51,62], they react to form CO_2 as given in Eqn. (14). Since the dissociation of adsorbed CO is highly negligible due to its strong CO bond, the L-H mechanism for the formation of CO_2 is not considered. The rhodium is reduced through the E-R mechanism to produce CO_2, and in turn this reduced rhodium is highly effective for NO dissociation [84].

2.3.5 N_2 Formation

Nitrogen primarily forms through the recombination step of nitrogen atoms and the disproportional step. The recombination of adsorbed nitrogen atoms as provided in Eqn. (9) can be considered as a rate-limiting step due to its low rate constant at temperatures below 400K [20]. In addition, its production kinetics were found to be high above 700K [95]. Apart from this recombination step, nitrogen can also form through the disproportional reaction of NO and N atoms through an L-H mechanism. However, it is neglected here because no experimental evidence exists to warrant its inclusion [71,86] and this step is typically not indicated when incorporating the N_2O formation step as in Eqn. (27). Of note, according to Granger et al. [19,91], the consideration of this step is based upon the partial pressures of NO. Since nitrogen molecules are found to desorbs from 400K to 700K based on their coverage [73,80], they are rapidly released when formed under typical catalytic operating temperatures.

2.4 GLOBAL RATE EXPRESSION

For completeness, this section presents two global kinetic mechanisms over Rh/Al_2O_3 as a function of the potentially different RDS depending on the concentrations of NO, CO and the temperature of the reacting species; NO dissociation and recombination of nitrogen atoms.

The formulation of the first RDS mechanism starts with NO adsorption where the forward and reverse rate equations are:

$\overline{R}_{2} = k_{2} p_{\mathrm{NO}} \theta_{\mathrm{Rh}}$	(64)
$\overline{R}_{-2} = k_{-2} \theta_{\mathrm{Rh \cdot NO}}$	(65)

At equilibrium, the rates become equal:

$k_{2} p_{\mathrm{NO}} \theta_{\mathrm{Rh}} = k_{-2} \theta_{\mathrm{Rh \cdot NO}}$	(66)

With the equilibrium constant in atm^{-1} defined as:

$K_{\mathrm{NO}} = k_{2} / k_{-2}$	(67)

The forward and reverse rate equations for CO adsorption are respectively:

$\overline{R}_{1} = k_{1} p_{\mathrm{CO}} \theta_{\mathrm{Rh}}$	(68)
$\overline{R}_{-1} = k_{-1} \theta_{\mathrm{Rh \cdot CO}}$	(69)

Similarly, at equilibrium the following balance is generated:

$k_{1} p_{\mathrm{CO}} \theta_{\mathrm{Rh}} = k_{-1} \theta_{\mathrm{Rh \cdot CO}}$	(70)

where:

$K_{\mathrm{CO}} = k_{1} / k_{-1}$	(71)

Assuming that the dissociation reaction, Eqn. (8), only proceeds in the forward direction which results in:

$\overline{R}_{8} = k_{8} \theta_{\mathrm{Rh \cdot NO}} \theta_{\mathrm{Rh}}$	(72)

If this is the RDS, a global reaction expression can be obtained from equating Eqns. (66) and (70) by solving for the associated coverage fractions of adsorbed NO and CO only.

$\theta_{\mathrm{Rh \cdot NO}} = K_{\mathrm{NO}} p_{\mathrm{NO}} \theta_{\mathrm{Rh}}$	(73)
$\theta_{\mathrm{Rh \cdot CO}} = K_{\mathrm{CO}} p_{\mathrm{CO}} \theta_{\mathrm{Rh}}$	(74)

Substituting Eqn. (73) in Eqn. (72),

$\overline{R}_8 = k_8 K_{NO} p_{NO} \theta_{Rh}^2$	(75)

Using the fact that $\theta_{Rh} = \left(1 - \theta_{Rh\cdot NO} - \theta_{Rh\cdot CO}\right)$ along with Eqns. (73) and (74), the coverage fraction for rhodium is found to be:

$\theta_{Rh} = \dfrac{1}{\left(1 + K_{CO} p_{CO} + K_{NO} p_{NO}\right)}$	(76)

Finally, by substituting Eqn. (76) into Eqn. (75) we obtain the following global reaction expression considering the dissociation of NO as the RDS:

$\overline{R}_{NO} = \overline{R}_8 = \dfrac{k_8 K_{NO} p_{NO}}{\left(1 + K_{CO} p_{CO} + K_{NO} p_{NO}\right)^2}$	(77)

Where k_8 is the rate constant in $molm^{-2}s^{-1}$ for the NO dissociation step with p_{NO} and p_{CO} the partial pressures of NO and CO species respectively. The expression derived above is similar to the expression developed by Granger et al. along with Dubois et al. [55,91].

If the RDS is the recombination of nitrogen atoms at low temperatures as previous researchers have considered [18,99], the rate expression obtained is determined from the forward rate expression and the surface coverage via Eqn. (9):

$\overline{R}_9 = k_9 \theta_{Rh\cdot N}^2$	(78)

with an activation energy between 108 and 128 kJ/mol. The overall rhodium coverage in the general case is equal to:

$\theta_{Rh} + \theta_{Rh\cdot NO} + \theta_{Rh\cdot CO} + \theta_{NO\cdot Rh\cdot CO} + \theta_{Rh\cdot N} + \theta_{Rh\cdot N_2O} + \theta_{Rh\cdot O} = 1$	(79)

History illustrates that oxygen does not disturb N_2 production kinetics; instead, it rapidly forms into CO_2 under the presence of CO [61,77]**.** In addition, the coverage factor of N_2O over rhodium can be neglected due to its fast decomposition and desorption kinetics. Moreover, the aforementioned history illustrates that the conversion of the intermediate $CO\cdot Rh\cdot NO$ into CO_2 is relatively fast and, therefore, its coverage factor can be neglected from the expression (79).

These calculations result in a simplified expression for the surface coverage which is in similar to vacant site expression of Araya and Cortes [100], excluding the factor for oxygen coverage:

$$\theta_{Rh} + \theta_{Rh\cdot NO} + \theta_{Rh\cdot CO} + \theta_{Rh\cdot N} = 1 \quad (80)$$

Incorporating the adsorption steps (1) and (2), the coverage fraction can be simplified into just Rh and Rh·N fractions:

$$\theta_{Rh} + K_{NO} p_{NO} \theta_{Rh} + K_{CO} p_{CO} \theta_{Rh} + \theta_{Rh\cdot N} = 1 \quad (81)$$

Solving for the Rh·N fraction results in:

$$\theta_{Rh\cdot N} = 1 - \left(K_{NO} p_{NO} + K_{CO} p_{CO} + 1\right)\theta_{Rh} \quad (82)$$

and the following for the rate expression in $molm^{-2}s^{-1}$ as a function of Rh coverage:

$$\overline{R}_9 = k_9 \left[1 - \left(K_{NO} p_{NO} + K_{CO} p_{CO} + 1\right)\theta_{Rh}\right]^2 \quad (83)$$

2.5 CONCLUSION

This chapter illustrates a comprehensive review of NO reduction by CO over rhodium. The author found that the adsorption of NO is greater than the adsorption of CO with a negligible self-inhibiting property due to the associated species coverage. Moreover, NO adsorbed species over rhodium frequently form an anionic or bent structure which is more suitable for NO dissociation due to their weak NO bonds. Based on the research performed, the author believe that the reaction mechanism follows the five fundamental steps given below: NO and CO Adsorption; NO Dissociation; N_2O Formation and Dissociation; CO_2 Formation; and N_2 Formation. The proposed detailed reaction mechanism from the analysis suggests a combination of Langmuir-Hinshelwood and Eley-Rideal mechanisms. In particular, CO oxidation follows an E-R mechanism at high temperatures and rich conditions. In addition, CO_2 conversion is high at

temperatures below 500K, and conversion is slow at higher temperatures and rich NO conditions. The reduction reaction of NO follows the L-H mechanism with the recombination of nitrogen atoms, and the dissociation of NO is considered to be the rate-limiting steps. The formation of N_2O and their corresponding decomposition is still under research, but from past studies, it is understood that the formation of N_2O occurs at low temperatures and at high NO pressures. Thus, in order to minimize N_2O formation, it is necessary to preheat the rhodium catalysts.

Furthermore, it is observed that the catalytic activity of rhodium metal to dissociate NO molecules decreases with an increase in dispersion or a decrease in rhodium size over an alumina substrate. Research is still required to finalize these effects and to choose the reaction mechanism that works best under realistic catalytic converter conditions. In the next chapter, similar analysis is carried out on platinum catalysts with appropriate global mechanisms.

CHAPTER 3
REDUCTION REACTION OF NITRIC OXIDE BY CARBON MONOXIDE OVER PLATINUM/ALUMINA CATALYSTS[†]

3.0 INTRODUCTION

Internal combustion engines produce harmful exhaust gases like carbon monoxide (CO), nitrogen oxides (NO_x), hydrocarbons (HC) and particulate matter (PM) due to incomplete combustion and high temperature dissociation of fuels. While exhaust gas concentrations of NO and CO for a typical four-stroke spark ignition engine range only between 100-4000 ppm depending upon the driving conditions, temperature and air/fuel ratio [1,2], they are a major concern for global air pollution as given in Figure 9 and account for around 57.6% and 38.3% of the total emissions for CO and NO_x respectively [3,101,102]. Because of the inability to remove these emissions completely using in-cylinder combustion techniques, engine manufacturers result to using catalytic exhaust aftertreatment devices as a preferred method to control their release into the atmosphere.

In the last two decades, emission regulations for automobile exhaust has become increasingly stringent and led to many studies on the reduction of nitric oxide over noble metal catalysts such as platinum, palladium and rhodium [35,40]. Since exhaust from spark ignition engines produces sufficient carbon monoxide under stoichiometric conditions, the NO-CO reaction over these noble metal catalysts plays an important role for effective NO_x reduction. In particular, researchers have investigated this reaction from both theoretical and experimental viewpoints and a significant amount of literature exists on this topic.

[†] This chapter has been submitted to Surface Reviews and Letters Journal.

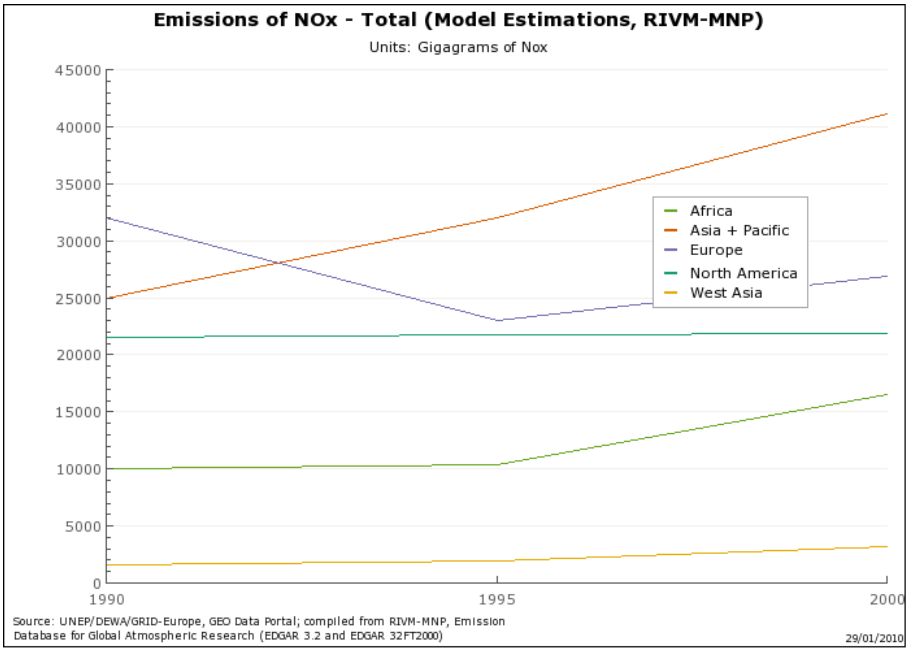

Figure 9: Total emissions of NO_x worldwide from 1990 to 2000 [102].

In this work, the author restrict a review of this research to platinum-alumina (Pt/Al_2O_3) catalysts to supplement rhodium-alumina (Rh/Al_2O_3) efforts documented in an earlier paper [32]. Similar to rhodium, the optimization of platinum metal loading over alumina substrate is very important due to the cost involved into the manufacturing of catalytic converters as given in Figure 10 [34]. With respect to platinum, research documents that this catalytic material effectively promotes the NO-CO reaction based on knowledge of platinum structures. Throughout these papers, researchers propose detailed reaction mechanisms based on the platinum surface orientation, kinetic oscillations and pressure conditions. In the recap of these efforts, the completed work presented here investigates this reaction mechanism in the absence of other species, such as hydrogen and hydrocarbons, in order to provide a clear focus of efforts.

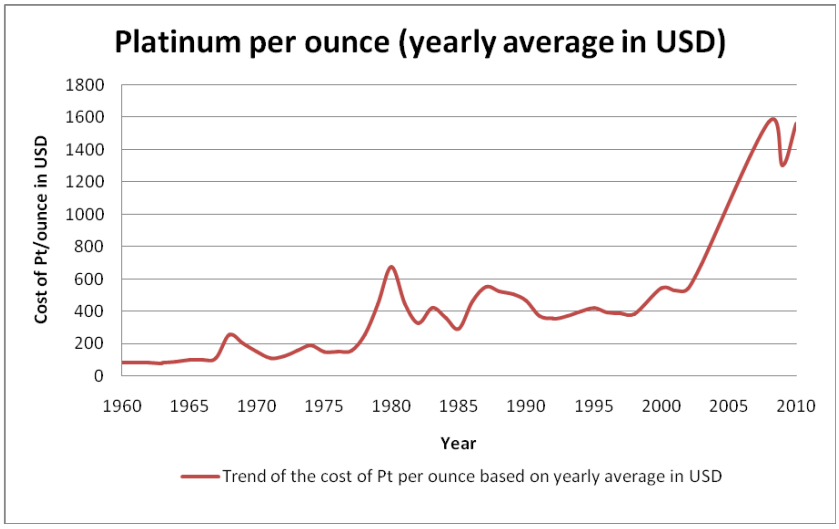

Figure 10: Historical prices of platinum per ounce based on yearly average from 1960-2010 in US dollars (plot reproduced based on the data provided) [34].

The outcome of this research is the formulation of a detailed kinetic mechanism that relies heavily on the previous research to indicate the main steps in the process. From this, the authors create a global kinetic mechanism that will simulate this reaction better than the current versions utilized in aftertreatment modeling literature [23].

3.1 REACTION HISTORY

In 1973, Unland became the first researcher to investigate the interaction of NO and CO over Pt/Al_2O_3 using infrared (IR) spectroscopy [103]. His results illustrate that the mechanism occurs via the following pathway with the inclusion of isocyanate (NCO) as a reaction intermediate:

$NO + Pt \xrightarrow{k_{82}} Pt \cdot N + Pt \cdot O$	(84)
$Pt \cdot N + CO \xrightarrow{k_{83}} Pt \cdot NCO$	(85)
$Pt \cdot O + CO \xrightarrow{k_{84}} CO_2 + Pt$	(86)
$Pt \cdot NCO + NO \xrightarrow{k_{85}} N_2 + CO_2 + Pt$	(87)

His efforts also document that that the dissociation of NO occurs at temperature higher than 300K.

In the following year, Kobylinksi and Taylor study the reduction of nitric oxide over platinum group catalysts and find that the reaction rate for Pt is lower than compared to rhodium (Rh) and ruthenium (Ru) due to the hindrance caused by the adsorbed CO molecules [104]. Moreover, they find the production of significant ammonia, approximately 77.6%, over Pt until reaching 1033K.

Concurrent to these efforts, Lambert and Comrie determine, from Auger spectroscopy and flash desorption experiments, that CO and NO adsorb non-dissociatively over Pt [105]. Above 300K, thermal dissociation of NO over Pt occurs and any dissociated monatomic oxygen reacts rapidly with adsorbed CO molecules. They establish that N_2 and CO_2 are the main products of the reaction kinetics with small amounts of nitrous oxide (N_2O) and O_2 produced and find no evidence for nitrogen dioxide (NO_2) and isocyanate formation. Their reasoning for the negligible formation of NO_2 and isocyanate is due to their relatively high activation energies when compared to that of the formation of CO_2 from monatomic oxygen. As a result, they propose the following reaction kinetics pathway:

$CO + Pt \underset{k_{-86}}{\overset{k_{86}}{\rightleftharpoons}} Pt \cdot CO$	(88)
$NO + Pt \underset{k_{-87}}{\overset{k_{87}}{\rightleftharpoons}} Pt \cdot NO$	(89)
$Pt \cdot NO + Pt \xrightarrow{k_{88}} Pt \cdot N + Pt \cdot O$	(90)
$Pt \cdot CO + Pt \cdot O \xrightarrow{k_{89}} CO_2 + 2Pt$	(91)
$2Pt \cdot N \xrightarrow{k_{90}} N_2 + 2Pt$	(92)
$Pt \cdot N + Pt \cdot NO \xrightarrow{k_{91}} N_2O + 2Pt$	(93)

$Pt \cdot O + Pt \cdot O \xrightarrow{k_{92}} 2Pt + O_2$	(94)

Two years later, Niiyama et al. investigate the formation of isocyanate over Pt surfaces using IR spectroscopy [106]. Their results show that isocyanate complexes form above 573K with a decline in rate for formation when the partial pressure of NO increases. The formation of NCO species acts as an inhibitor and not as a reaction intermediate in the NO-CO kinetics. Moreover, under practical conditions NCO readily forms ammonia when reacting with water.

In the following year, Solymosi et al. looked into the interaction of NO-CO species and their formation of isocyanate complexes over 5% Pt/Al_2O_3 using thermal decomposition and IR spectroscopic measurements with the temperature ranging between 298 and 673K [107]. They suggest that reduced platinum sites play an important role by factoring in the adsorption and dissociation of NO species. In particular, adsorbed NO species usually bond to platinum in linear form. Moreover, they indicate that at high temperatures the Eley-Rideal (E-R) mechanism between CO and adsorbed NO is responsible for isocyanate formation. Besides clean Pt_{111} and Pt_{100} catalysts, Pt/Al_2O_3 demonstrates no evidence for the formation of isocyanate complexes. This results in a reaction mechanism that follows Eqns. (85), (88), (89), (90), (91) and (92). They follow this effort by studying the influence of the support materials on the formation of isocyanate over Pt using infrared spectroscopy [108]. Their efforts show that the stability and formation of isocyanate species depends upon the substrate metal. Experimental results demonstrate that dissociated nitrogen atoms migrate from platinum catalyst to alumina and react with gaseous or adsorbed CO to yield isocyanate species. Moreover, isocyanate formed over Al_2O_3 is relatively unstable as compared to MgO and SiO_2 support materials.

In 1979, Chang and Hegedus investigate the influence of inhibitors in the reduction of NO by CO [109]. From their IR and integral reactor experimental results, chemisorbed CO at

richer than stoichiometric conditions and dissociatively chemisorbed oxygen at lean conditions act as inhibitors for the NO-CO reaction. They reason that the high conversion rates for NO and CO molecules at a stoichiometric feed ratio occur because of sufficient oxygen to control the inhibition caused by CO, but not too much to act as an inhibitor for the reaction. Hence, the formation of species on the surface serves to indicate the stoichiometric range. In the next year, Hegedus et al. investigate Pt/Al_2O_3 when exposed to NO, CO and O_2 at 1051K [110]. They find an increase in cyclic frequency augments the conversion rates of CO and NO molecules. Moreover, they find that the formation of isocyanate requires at least two surface species; e.g., its formation follows a Langmuir-Hinshelwood (L-H) mechanism between the adsorbed NO and CO species.

In 1980, Singh-Boparai and King characterize the NO-CO reactions over Pt_{100} at 300K and ultrahigh vacuum (UHV) conditions using a molecular beam technique [111]. From their experimental results, they determine that L-H kinetics between adsorbed CO and NO do not apply for this reaction because experiments occurring under two different conditions provided different results. In particular, the first experiment between pre-absorbed NO and gaseous CO proceeds via an L-H mechanism to produce N_2 and CO_2. Whereas, when CO is pre-adsorbed, the reaction does not complete until termination of the NO beam indicating that it does not follow the same pathway.

In the following year, Gorte and Schmidt study the interaction of NO and CO over Pt_{111} using temperature programmed desorption [112]. Under UHV conditions, the reaction between NO and CO does not occur to a measurable extent until it reaches the desorption temperature of NO which ranges from 250 – 350K. They determine that the sticking coefficient of CO is independent of CO, NO coverage, and the sticking coefficient of NO follows similarly but it

sharply reduces near CO saturation. Moreover, the co-adsorption of CO affects the NO desorption temperature by lowering it around 100K; whereas, the co-adsorption of NO does not influence CO desorption temperature due to its strong bond to the platinum surface.

Two years later, Banholzer and Masel research the adsorption characteristics of NO and CO on Pt_{100} with reflection-adsorption infrared spectroscopy (RAIRS) [113]. Their results show clear evidence for strong chemical interactions between NO and CO over this surface. These efforts demonstrate an autocatalytic behavior of the species; i.e., surface explosion of the N_2 and CO_2 products were produced at a narrow peak temperature above 450K (later supported by Lesley and Schmidt [114]). Moreover, they discover that adsorbed CO does not form an impenetrable island over Pt_{100} and this supports the adsorption of NO over these islands in the form of bridged structure.

In 1985, Lesley and Schmidt demonstrate the autocatalytic behavior of the reduction reaction of NO by CO over Pt_{100} using temperature programmed desorption (TPD), low energy electron diffraction (LEED) and isothermal desorption mass spectrometry measurements [114]. From the TPD spectra for the NO-CO reaction, N_2 and CO_2 desorb instantaneously at 410K and are virtually independent of the coverage fractions up to 10^{-6} torr. They determine that as the partial pressure of the reactants increases, the peak temperature of the products increases considerably and this trend suggests that first or second order rate expressions cannot describe the reaction kinetics. Various factors cause the autocatalytic behavior, which is known as an abrupt change in the reaction rate; two of which are the formation of CO islands over Pt with strong attraction between CO molecules [112] and the decrease in the activation energy with the corresponding decrease in coverage due to the interaction between adsorbents [115]. However, the above factors do not have a greater influence on the reaction rate due to their insufficient and

inconsistent experimental evidence. Moreover, they propose a possible reaction mechanism satisfying the trends of production peaks and suggest that the dissociation of NO atoms is the slowest step while the formation of CO_2 from L-H mechanism is instantaneous. Their reaction mechanism follows Eqns. (88), (89), (90), (91), (92) and the following reaction with the formation of reactive intermediate species or structural changes in the platinum catalyst promoting the autocatalytic mechanism.

$Pt \cdot N + Pt \cdot NO \xrightarrow{k_{93}} 2Pt \cdot N + Pt \cdot O$	(95)

One year later, Schwartz and Schmidt review their experimental results and describe that the NO-CO reaction over clean Pt_{100} or on polycrystalline Pt can exhibit oscillations at all pressures between 10^{-8} and 1 torr [116]. They determine this to be due to the change in the surface phase transition from hexagonal to a square (1×1) surface. Concurrently, Muraki and Fujitani provide a broad view on the reduction of NO by CO over platinum group metals (PGM) supported by α-Al_2O_3 under cyclic feed streams [117]. The catalytic activity of platinum in the NO reduction is the least among platinum group metals because of its susceptibility to CO self-poisoning. Moreover, the formation of N_2O is the highest when compared to Rh, Pd and Ru.

In 1988, Matyshak investigated the kinetics of NO-CO under lean conditions and proposed a reaction mechanism that follows Eqns. (88), (89), (90), (91), (92) with the subsequent additions [118]:

$Pt \cdot N + Pt \cdot CO \xrightarrow{k_{94}} Pt \cdot NCO + Pt$	(96)
$Pt \cdot NCO + Pt \cdot NO \xrightarrow{k_{95}} N_2 + Pt \cdot CO_2 + Pt$	(97)
$Pt \cdot CO_2 \xrightarrow{k_{96}} CO_2 + Pt$	(98)

It is shown that the formation of nitrogen reaction through the adsorbed isocyanate is included at low temperature conditions of about 400K.

At the same time, Schwartz and Schimdt continue their investigation of NO-CO oscillations over Pt_{100} under steady state conditions using LEED measurements [119]. They conclude that the reaction rate of CO and O_2 is ten times lower than NO and CO at UHV conditions. Moreover, they establish that the dissociation of NO increases with an increase in temperature above 450K. They state that the oscillatory behavior of the reaction occurs due to the surface phase transition from 1×1 to a hexagonal surface that does not strongly absorb CO or NO molecules.

In 1989, Banse et al. investigate transient NO-CO kinetics over a polycrystalline platinum surface [120]. Their study involves two possible mechanisms (both L-H and E-R) and the corresponding rate law equations for transient conditions. Based on their observations, they propose that the reaction to CO_2 proceeds through an L-H mechanism. Their efforts demonstrate that the dissociative mechanism of NO is responsible for the production of monatomic oxygen atoms on the surface, which in turn produces CO_2. As a result, they theorize that the reaction mechanism follows Eqns. (88), (89), (90), (91) and (92).

In 1991, Fink et al. propose a mechanism for the NO-CO reaction over Pt_{100} [121]. Their reaction mechanism considers the dissociation of NO as the rate-determining step with five individual steps as follows:

- Under high CO partial pressures, CO molecules poison the Pt surface due to their low adsorption enthalpy and eventual desorption of the molecules yields vacant sites.
- As the temperature increases, CO forms CO_2 and this creates vacant sites for NO dissociation that in turn produces N_2 leading to a 'surface explosion' of CO_2 and N_2 occurring at 390K.

- Any NO adsorbed on clean Pt sites dissociates and the corresponding atomic nitrogen produced desorbs rapidly as N_2 through a recombination step leading to an increase the oxygen coverage that eventually hinders NO dissociation.
- Due to the previous step, adsorption of NO and monatomic oxygen molecules increases.
- Adsorbed CO removes surface oxygen in order to produce CO_2 that ultimately regenerates mixed NO+CO adsorbed sites.

Their reaction mechanism follows Eqns. (88), (89), (90), (91) and (92) with the requirement of at least three Pt sites.

Concurrently, Yaldram and Khan study the reaction kinetics using Monte Carlo simulations over square and hexagonal surfaces of a Pt catalyst [122]. Their reaction mechanism follows Eqns. (88), (89), (90), (91) and (92) with the dissociation of NO being the rate determining step while also including a higher CO affinity during adsorption. They observe that the reactivity of the surface oxygen from NO dissociation is somewhat less when compared to the reactivity of the surface oxygen from the dissociated oxygen. One year later, Fink et al. look into the oscillatory characteristics of the products over Pt_{100} under isothermal conditions at low pressures of 10^{-6} mbar using bifurcation theory [123]. Their results collaborate with their earlier efforts by following a similar reaction mechanism as proposed above with Eqns. (88), (89), (90), (91) and (92) and the dissociation of NO considered the rate-determining step. They formulate differential equations for CO, NO and O coverage factors with equations for empty sites and the repulsive interactions of CO-NO chemisorbed molecules. The resultant numerical integration of the differential equations yields the kinetic oscillations of the reaction that in turn substantiates the proposed reaction mechanism.

In 1992, Scharpf and Benziger investigate the adsorption-desorption characteristics of NO and CO molecules [124]. They conclude that the sticking probability of CO species is nearly constant from 430 to 490K and therefore consider it temperature independent. Desorption of CO is found to be high above 450K and the presence of NO molecules over Pt is directly proportional to desorption of the CO molecules. Their theorized reaction mechanism follows Eqns. (88), (89), (90), (91) and (92) while additionally including:

$Pt \cdot NO + Pt \cdot CO \xrightarrow{k_{97}} Pt \cdot N + CO_2 + Pt$	(99)

They postulate that this bimolecular reaction step, Eqn. (99), is the rate limiting step as their data correlates well with previous findings by Klein et al. [125]. Moreover, their experimental data shows inconsistency towards the commonly assumed rate-determining step of NO dissociation.

At the same time, Uchida et al. examine the structural changes due to the influence of explosive reactions of NO-CO using reflection electron microscopy (REM) under 10^{-6} Torr of chamber pressure [126]. They discern that the transition between 1×1 and hex phase of the Pt_{100} crystal structure occurs because of adsorption of CO and NO molecules. Whereas, a Pt_{111} flat surface is insensitive to the NO-CO reaction. Based on their experiments, they determine that Pt_{100} is likely to be more active than Pt_{111} for NO reduction. Concurrently, Veser and Imbihl scrutinize the spatial pattern formation in the NO-CO reaction using photoemission electron microscopy (PEEM) under 10^{-6} torr and temperature ranging between 380 and 430K [127]. They conclude that the Pt_{100} and Pt_{310} surfaces are highly active for NO dissociation and propose a reaction mechanism similar to others that follows Eqns. (88), (89), (90), (91) and (92).

Two years later, David uses molecular beam studies to examine the oscillatory behavior of the reaction over Pt_{100} [128]. From their studies under high CO-NO coverage at temperatures ranging from 380 to 410K, they determine NO dissociation to be the rate-determining step.

Their proposed reaction mechanism is of L-H type that again follows Eqns. (88), (89), (90), (91) and (92). Their experiments show that as the temperature increases, so does the density of empty sites available for dissociation and their sustained oscillations.

In 1994, Evans et al. analyze lattice-gas models over a Pt_{100} surface [129]. They suggest the common reaction mechanism following Eqns. (88), (89), (90), (91) and (92) with the requirement of two empty sites for the adsorption species and neglecting their diffusion between sites. They conclude that adsorbed NO instantaneously dissociates in order to create nitrogen atoms that detach immediately when nitrogen forms. Moreover, adjacent CO and O atoms instantaneously react to produce CO_2. Concurrently, Zagatta et al. examine the products of the reaction over Pt_{100} using temperature programmed reaction methods [130]. They find that the major reaction products are N_2 and CO_2 along with the formation of small amounts of N_2O. Furthermore, they observe that a part of the oxygen produced from dissociation reaction of NO does not react with CO and instead remains adsorbed on the Pt site.

In tandem, Vesser and Imbihl probe the oscillatory characteristics of the reaction over Pt_{100} at 10^{-6} mbar using PEEM [131]. At a partial pressure ratio of NO and CO ranging from 0.8 to 1.9 and at low temperatures below 405 K, they observe unsynchronized oscillations with the indication of high sensitivity towards NO-CO reaction under small microscopic defects in the structure.

In the following year, Graham and Kevrekidis investigate concentration patterns using the Karhunen-Loeve (KL) decomposition method in order to provide a clear recognition of the visual arrangement [132]. They state that this method clarifies the surface dynamics even with small surface defects over Pt and can strongly modify the local reactivity in the NO-CO mechanism. The details about the structural aspects of the platinum were mostly irrelevant to this

review and considered to be beyond the scope of this research. Meanwhile, Svoronos et al. explore a different perspective of the kinetics based upon the preparation conditions of the catalyst [133]. Their TPD measurements under steady state conditions indicate that the catalytic activity of the acid treated catalysts were higher (up to five times the magnitude) than those prepared under basic conditions. Therefore, the results indicate that impregnated pH will influence metal dispersion and the reaction activity of the catalysts.

In 1996, Mergler and Nieuwenhuys investigate the reaction over 0.4% wt of Pt/Al_2O_3 under reducing conditions [134]. They find that the deactivation of the catalyst occurs without any oscillations under reducing conditions at 673K. This happens because of the accumulation of strongly adsorbed CO molecules that reduce the number of vacant sites required for NO dissociation. They discover that the dispersion of the Pt catalysts over alumina allows for a relatively easily oxidation due to the preferential dissociation step of oxygen molecules. Thus, adsorbed CO molecules are relatively inert until 673K under oxidizing conditions. Furthermore, they conclude that isocyanate does not form over Pt/Al_2O_3. In the same year, Sadhankar and Lynch investigate reaction transient characteristics using an external recycle reactor [135]. Based on their experiments, they propose a reaction mechanism that follows Eqns. (88), (89), (90), (91), (92), (93) and the following while including negligible internal diffusion:

$N_2O + Pt \xrightarrow{k_{98}} N_2 + Pt \cdot O$	(100)

They find that their model corroborates well with the previous works with respect to the CO conversion; i.e., the decrease in CO conversion is proportional to the increase in CO surface coverage.

One year later, Sadhankar and Lynch follow up their efforts by investigating the reaction under steady state conditions with the temperature ranging from 465 to 520K [136]. They utilize

the same reaction mechanism and observe the formation of N_2O under high NO partial pressures with a selectivity decreasing rapidly corresponding to an increase in NO conversion. Moreover, they find a relatively strong inhibition by CO molecules. At the same time, Miners et al. suggest a technique to determine the phase relationship of CO and NO adsorption bands over Pt_{100} based on their partial pressures in the low temperature region ranging from 380 to 411K [137]. This technique involves measuring real time infrared data from an oscillatory reaction system. They find that their experimental method correlates well with the Fink et al. [123] results that describe the driving factor of oscillations is a surface explosion. This phenomenon reduces the surface coverage of the CO and NO molecules, which subsequently increases the vacant sites for NO dissociation.

In 1998, Granger et al. develop reaction kinetics at 573K with CO and NO partial pressures ranging from 1.5×10^{-3} to 9×10^{-3} atm [138]. Their experimental studies reveal that the nature of the support material determines the adsorption and dissociation rate constants of the reaction. Their kinetic mechanism follows Eqns. (88), (89), (90), (91), (92), (93) and the following:

$\mathrm{Pt\cdot N + Pt\cdot NO \xrightarrow{k_{99}} N_2 + Pt\cdot O + Pt}$	(101)

They discern that the apparent activation energy for CO, NO and N_2O are 19, 22 and 27 kcal mol^{-1} respectively following the order of Pt/Al_2O_3 < Pt/Si_3N_4 < Pt/Cr_3C_2. Moreover, the selectivity of N_2O is higher for Pt/Al_2O_3 due to a lower activation energy as compared to Pt/Si_3N_4 and Pt/Cr_3C_2. Their reaction mechanism assumes the rapid non-dissociative adsorptions of CO and NO with the dissociation of NO species on the nearest vacant Pt site. This mechanism utilizes three Pt sites by considering the dissociation of NO molecule as the rate-determining step with the corresponding rate expression given below:

$\overline{R}_{88} = \frac{k_{88} K_{NO} p_{NO}}{\left(1 + K_{CO} p_{CO} + K_{NO} p_{NO}\right)^2}$	(102)

Where, K_{CO} and K_{NO} are the adsorption equilibrium constants of CO and NO respectively.

In the next year, Frank and Renken were among the first to study the reaction kinetics involving the formation of N_2O over a MoO_3 supported Pt/Al_2O_3 catalyst [139]. Their proposed reaction mechanism is of the L-H type following Eqns. (88), (89), (90), (91) and (92) with NO dissociation being the rate determining step. They state that the rate of N_2O formation decreases above 673K with a relatively slow deactivation of the catalyst observed under reducing conditions. In this case, they refer to deactivation as the cause for reduction in the NO conversion rate. Moreover, a relatively low activity occurs in the deactivated state due to the strong adsorption of CO over Pt and, hence, is not due to the presence of isocyanates that only act to delay the deactivation state.

Miners et al. investigating the kinetics of the reaction and propose favorable conditions for the formation of NCO over Pt_{100} using Infrared Reflection Absorption Spectroscopy (IRAS) under non-oscillatory conditions [140]. They discover that the CO molecules have a higher enthalpy of adsorption over NO and as a result, CO absorbs first creating an initial poisoning over the Pt_{100} surface. As the temperature increases to 415K, adsorbed CO molecules form CO_2 that in turn provide sites for NO molecular adsorption. Their theorized reaction mechanism follows Eqns. (88), (89), (90), (91), (92) and (96) with rapid desorption of N_2 and CO_2 molecules from the surface. They suggest that NCO formation becomes favorable at low temperatures around 380K when the surface is covered with significant CO molecules and low concentration of N atoms. A high coverage of CO molecules, therefore, hinders the diffusion of monatomic

nitrogen atoms resulting in the production of NCO. Moreover, they mention that dissociation of NCO occurs above 396K following:

$Pt \cdot NCO + Pt \xrightarrow{k_{101}} Pt \cdot CO + Pt \cdot N$	(103)

Under rich combustion, relatively high CO coverages reduce the diffusion of N-atoms, even at high temperatures of about 453K.

In the same year, Takeshima et al. suggest a new method for preparing catalysts using micro-emulsion (ME) techniques [141]. Based on their experimental results, they show that anisotropic platinum catalysts have relatively low NO conversion and low N_2 selectivity due to their low activity for NO dissociation. Whereas, Pt catalysts prepared using the ME method demonstrate high NO conversion with high N_2 selectivity even at temperatures above 613K. Concurrently, Granger et al. extend their earlier efforts by proposing a kinetic mechanism for the intermediate N_2O with CO [142]. They express that the CO and N_2O reaction occurs more readily on Pt rather than on Rh and the decomposition of N_2O is very slow; conversion is around 6% even at 773K. Their efforts reveal that the dissociation of adsorbed N_2O over Pt is the rate-determining step in this reaction.

In this same year, Aida et al. research the influence of intra-pellet diffusion and adsorption of the species along a plug flow reactor [143]. Their model calculations on the time-averaged conversion of NO species suggest that the effect of this diffusion requires consideration for strong adsorption under periodic operations. Meanwhile, Akama and Matsushita discuss the progress in NO_x reducing catalysts for spark ignition and compression ignition engines [144]. They suggest that a platinum catalyst allows for effective reduction of NO_x at low temperatures ranging from 523 to 573K; however, the formation of N_2O is relatively high at these respective temperatures.

With advancement in crystal technology, in the next year Hartmann et al. investigate pattern formation of the NO-CO reaction over a Pt_{100} surface by changing crystal surface size and geometry [145]. They employ photoelectron emission microscopy (PEEM) in creating different patterns such as circles, rings and dumbbells that correspond to various size and geometry of the Pt_{100} sites. These Pt_{100} sites show significant differences in their NO-CO reaction rate based on their respective patterns. Thus, this is one of their techniques to find the change in reaction rate based on the Pt_{100} domains. At the same time, Miners and Gardner scrutinize the oscillatory behavior of the reaction kinetics over the same surface at a partial pressure of 10^{-7} mbar [140]. From their LEED and IRAS studies, they find that reaction rates and oscillations are relatively high when the surface is in the hex phase. Moreover, they discover that their surface should be a defective hex site i.e.: the platinum sites with square and hex phase for efficient NO dissociation.

In 2001, Bourane et al. describe the adsorption of NO molecules on a reduced catalyst using Fourier Transform Infrared (FTIR) spectroscopy at temperatures ranging from 300 to 680K [146]. They observe two types of linear adsorbed NO species that correspond to defect and terrace sites of Pt. They identify linear NO species at 1764 and 1710 cm^{-1} infrared bands and consider that these adsorbed species are immobile with the heat of adsorption having a linear trend with surface coverage. Based on their assumptions, they formulate an expression relating coverage and heat of adsorption of the species as follows:

$$\theta = \frac{R_u T_a}{\Delta H} \ln\left[\frac{1+K_0 p_a}{1+K_1 p_a}\right] \qquad (104)$$

Where, ΔH is the difference in the heat of adsorption at coverage, $\theta = \theta(E_0)$ and $\theta = \theta(E_1)$, K_0 and K_1 are the adsorption coefficients at $\theta = 0$ and $\theta = 1$, respectively; and T_a and p_a are the adsorption temperature and pressure respectively. From their analytical results, they determine

the heat of adsorption of linear NO species to have a linear trend with E_{a0} = 135 kJ mol^{-1} at zero coverage to E_{a1} = 105 kJ mol^{-1} at full coverage. Moreover, they state that NO dissociates over the catalyst at temperatures greater than 400K.

Concurrently, Ikeda et al. explore the thermal stability characteristics of Pt particles prepared by different methods and examine their corresponding catalytic activity [147]. They determine that pressed micro-emulsion Pt catalysts have the highest NO conversion rate and greatest resistance towards sintering even after a thermal treatment at 973K as compared to sol-gel and impregnation prepared catalysts. At the same time, Granger et al. re-consider the kinetics of the reaction using IR spectroscopy [148]. Their revised reaction mechanism then follows Eqns. (88), (89), (90), (91), (92) and (101). They additionally make mention of different states at which NO is adsorbed over Pt. It is observed that neutral NO species were predominant over Pt/Al_2O_3 which indicates weaker NO adsorption and a slower dissociation of NO species.

Their studies reveal a higher probability towards strong CO adsorption with a weaker NO adsorption and corresponding slow rate of NO dissociation. Similar to rhodium, NO species demonstrate the ability to have positive, neutral and negatively charged adsorption species dependent upon the oxidation state of Pt sites.

In 2002, Na-Ranong et al. explore the reaction kinetics at 423K under periodic and steady state conditions [149]. Based on the slope of their logarithmic plots under steady state conditions, they determine that the reaction order is 0.9 and -0.7 with respect to NO and CO concentrations. The negative reaction order for CO occurs because of strong CO adsorption over Pt. Their proposed reaction kinetics follows an L-H mechanism that neglects the NO dissociation step because of findings from their low temperature experiments. As a result, their reaction mechanism includes Eqns. (88), (89), (90), (91), (92) and (105).

$\mathrm{Pt \cdot NO + Pt \cdot CO \underset{k_{-103}}{\overset{k_{103}}{\rightleftharpoons}} Pt \cdot N + CO_2 + Pt}$	(105)

with the global reaction rates of NO described as:

$\overline{R}_{\mathrm{NO}} = \frac{n\left(k_{103}K_{\mathrm{NO}}K_{\mathrm{CO}}C_{\mathrm{NO}}C_{\mathrm{CO}} + k_{91}K_{\mathrm{NO}}C_{\mathrm{NO}}\alpha\right)}{\left(1 + K_{\mathrm{NO}}C_{\mathrm{NO}} + K_{\mathrm{CO}}C_{\mathrm{CO}} + \alpha\right)^2}$	(106)

Where

$\alpha = \frac{\sqrt{\left(k_{91}K_{\mathrm{NO}}C_{\mathrm{NO}}\right)^2 + 4k_{103}k_{90}K_{\mathrm{NO}}K_{\mathrm{CO}}C_{\mathrm{NO}}C_{\mathrm{CO}}} - k_{91}K_{\mathrm{NO}}C_{\mathrm{NO}}}{2k_{90}}$	(107)

Here, 'K_{NO}' and 'K_{CO}' are in s^{-1} and 'α' in 'mol $m^{-3}s^{-1}$'. In Eqn. (106), the numerator corresponds to the elimination of NO molecules through Eqns (93) and (105) and the denominator corresponds to the Pt vacant sites. Furthermore, they illustrate that the selectivity towards nitrogen increases as the concentration of CO species increases and present this selectivity as:

$\frac{\overline{R}_{\mathrm{N_2}}}{\overline{R}_{\mathrm{N_2O}}} = \frac{k_{90}\alpha}{k_{91}K_{\mathrm{NO}}C_{\mathrm{NO}}}$	(108)

Concurrently, Zhdanov employs the first Monte Carlo simulations of the kinetic oscillations that occur in the catalytic reaction over Pt_{100} [150]. This results in a proposed reaction mechanism that follows Eqns. (88), (89), (90), (91), (92) and (93) while including a consideration of diffusion of the adsorbed CO and NO molecules over Pt for the effective dissociation of NO. In addition to this work, Zhdanov utilized Monte Carlo simulations to examine experiments conducted under UHV conditions with temperatures ranging from 400 to 500 K [151]. This ends in the proposition of the same reaction mechanism with kinetic oscillations depending upon the NO dissociation step at temperatures below 430K.

In 2003, Yubing and Shoujia document a mathematical model at high NO pressures over Pt/Al_2O_3 catalyst [152]. They determine that the dissociation of NO dominates at low pressures;

whereas, at high NO pressures, the bimolecular reaction between CO and NO is the rate-determining step. Their detailed L-H reaction mechanism follows Eqns. (88), (89), (92), (93) and (105) with the corresponding production rates of CO_2 and N_2 equal to:

$\overline{R}_{CO_2} = k_{CO_2}\theta_{NO}\theta_{CO} = \frac{k_{CO_2}K_{NO}p_{NO}K_{CO}p_{CO}}{\left(1+K_{NO}p_{NO}+K_{CO}p_{CO}\right)^2}$	(109)
$\overline{R}_{N_2} = k_{N_2}\theta_{NO}\theta_{CO} = \frac{k_{N_2}K_{NO}p_{NO}K_{CO}p_{CO}}{\left(1+K_{NO}p_{NO}+K_{CO}p_{CO}\right)^2}$	(110)

During this same year, Matsushima et al. investigate desorption dynamics of the explosive NO-CO reaction over Pt_{100} using thermal desorption and time-of-flight techniques [153]. Their investigation ends in the commonly proposed reaction mechanism following Eqns. (88), (89), (90), (91) and (92). They determine that the L-H reaction between adsorbed CO and adsorbed O atoms occurs rapidly at 400K and the recombination of nitrogen atoms is the only step possible to produce nitrogen because of the lack of experimental evidence for the other nitrogen formation steps. They find the peak of desorption for CO_2 and N_2 species occurs in a narrow range of temperature between 360 and 400K. Moreover, they find the formation of N_2O and its decomposition occurs even at 140K over a Pt_{112} surface.

Meanwhile, Rienks et al. spend the year examining the reaction over Pt_{100} using synchrotron X-ray photoelectron spectroscopy under 10^{-7} mbar of total pressure [154]. Again, the same reaction mechanism is proposed through Eqns. (88), (89), (90), (91) and (92) while additionally considering the reconstruction of the Pt structure during the clean state; i.e., the phase transition from hexagonal state to square (1×1) phase. Moreover, they consider the square phase to be active for NO dissociation. Based on their experimental results, they postulate that NO dissociates rapidly and thus it is not the rate-determining step. Instead, they consider the

removal of adsorbed monatomic oxygen and monatomic nitrogen from the dissociation reaction the rate-determining step.

In the following year, Zhdanov simulates the kinetic oscillations in the reaction using Monte Carlo methods while varying the lattice size of the Pt catalysts down to the nanometer scale [21]. The reaction mechanism considered for simulation follows Eqns. (88), (89), (90), (91) and (92) with rapid formation of N_2 indicating low N-atoms coverage. He finds that the kinetics of the nanometer-sized catalyst lattice indicates irregular kinetic oscillations as compared to that of uniform lattices. At the same time, Makeev and Kevrekidis investigate the kinetics over Pt_{100} using coarse grained bifurcation analysis with a resulting reaction mechanism following Eqns. (88), (89), (90), (91) and (92) [155]. Miners et al. examined the same metal looking at the coverage dependency of the molecules in the low temperature oscillatory region [156]. They suggest that adsorbed CO molecules occur atop; i.e., CO molecules top the Pt site and create bridged structures while exhibiting identical adsorption and reaction behaviors. Moreover, the oscillatory characteristics that result corroborate Fink et al.'s earlier model [121].

In 2005, Alas et al. propose a relatively new reaction mechanism over Pt_{100} by replacing the classical recombination step of nitrogen atoms with an N-NO intermediate step while additionally neglecting the formation of N_2O [157]. Moreover, they disregard the diffusion and desorption of oxygen atoms. They deem this intermediate step responsible for the formation of gaseous nitrogen but they do not find any experimental data available for its rate of formation and subsequent decay. Their proposed mechanism follows Eqns. (88), (89), (90), (91) and two new reactions:

$\mathrm{Pt \cdot NO + Pt \cdot N \underset{k_{-109}}{\overset{k_{109}}{\rightleftharpoons}} Pt \cdot (N\text{-}NO) + Pt}$	(111)

$Pt \cdot (N\text{-}NO) \xrightarrow{k_{110}} N_2 + Pt \cdot O$	(112)

Meanwhile, Horino and Matsushima study the angular and velocity distributions of the desorbing products like N_2 and CO_2 over Pt_{100} [158]. From their experimental results during a steady-state reaction, they discover that the reaction rate increases around 400K due to an increase in desorption of CO, further allowing vacant sites for NO dissociation. Moreover, the structural transformation from 1×1 to hex occurs during the explosive desorption of the products leading to a faster recombination step of nitrogen atoms.

In the next year, Alas and Zgrablich investigate oscillations and pattern formation over Pt_{100} crystals at low pressure conditions around 0.4×10^{-5} Pa [159]. They state that sustained oscillations are formed when NO and CO diffusion rates are relatively high and linear. This higher rate of NO diffusion causes an increase in the vacant sites and augments the rate of dissociation of NO. Their experimental oscillatory studies reveal that the diffusion of both species, NO and CO molecules, requires consideration when determining the appropriate reaction rate for the mechanism.

In 2006, Bianchi and Derrouiche examine the effect of oxidation on CO species due to the adsorption of NO molecules over 2.9 wt% Pt/Al_2O_3 utilizing FTIR and mass spectrometer (MS) experiments [160]. They illustrate that CO and NO adsorbs through linear and bridged type molecules with the linear bond being the strongest. Furthermore, they determine that the adsorbed N-species from NO dissociation inhibits CO oxidation and the oxidation of CO species involves an L-H mechanism to form CO_2. Their micro-kinetic studies reveal that CO is favored during adsorption under competitive CO-NO chemisorptions at 300K. Experiments demonstrate that linear CO bonds are stronger than bridged CO structures and NO does not displace linear CO species but it can dissociate over free Pt sites that form during the desorption of bridged CO.

These resulting adsorbed N atoms do not desorbs easily; experimentally corroborated by their higher binding energies (>3.9 eV) than that of adsorbed NO (>1.3 eV) and adsorbed oxygen (>3.2 eV).

Concurrently, Liu et al. scrutinize the influence of surface impurities on the oscillations of the reaction mechanism over Pt_{100} [161]. Their efforts demonstrate that an increase in impurities shifts regular sustained oscillations into a damped oscillation regime. Moreover, global sustained oscillations appear when diffusion rates of NO and CO molecules increases.

In the following year, Mantri et al. propose a small change to the reaction mechanism under atmospheric pressures by taking into account the formation of N_2O [162]. Their elementary steps follow Eqns. (88), (89), (90), (91), (92) with two additional reactions:

$Pt \cdot N + Pt \cdot NO \xrightarrow{k_{111}} Pt \cdot N_2O + Pt$	(113)
$Pt \cdot N_2O \xrightarrow{k_{112}} N_2O + Pt$	(114)

In their mechanism, they consider the dissociation of NO the rate-determining step. According to their findings, N_2O concentrations are higher than N_2 at temperatures around 603K; however, this phenomenon sharply decreases as temperature rises. Under atmospheric conditions, strong competition for the catalyst sites results in oscillations (bifurcations) over Pt_{111}; whereas, under UHV conditions, Pt_{111} does not demonstrate any oscillations due to the relatively low activity of NO dissociation.

Mantri and Aghalayam follow this paper with a second effort in order to provide detailed results in the reduction of NO based on the influence of temperature, coverage and surface area [22]. Their reaction mechanism follows Eqns. (87), (88), (89), (90), (91), (92), (113) and (114) with the dissociation step of NO considered the rate-determining step. They observe that the formation of nitrogen occurs through the recombination of nitrogen atoms, and the formation of

N_2O happens through Eqn. (113). Their detailed study on surface coverage suggests the following phenomenon:

i. At temperatures less than 523K, the Pt catalyst is saturated with CO molecules making the catalyst relatively inert and resulting in low conversion rates of NO and CO.

ii. At temperatures between 553 and 623K, the abundant presence of adsorbed NO and N atoms lead to the formation of N_2O through an L-H mechanism.

iii. At temperatures higher than 643K, most of the adsorbed NO dissociates which in turn leads to less N_2O production.

iv. At temperatures higher than 673K, the dissociated NO rapidly forms N_2 and simultaneously CO rapidly forms CO_2 leading to a lower oxygen coverage and reduced state of the Pt catalyst at all ranges.

From their comparative studies with Rh catalysts, they determine that the activation energy for the dissociation of adsorbed NO molecules over Rh is lower than that of Pt making rhodium a better catalyst for NO conversion at low temperatures while additionally leading to less N_2O production. Moreover, they illustrate that at temperatures above 300K, an increase in surface area and residence time will increase the conversion activity of adsorbed NO.

Two years later, in an extension to their previous work, Alas and Vicente scrutinize the surface explosion phenomenon under low pressures about 10^{-6} to 10^{-4} Pa and 300 to 550K temperature conditions using temperature programmed reaction (TPR) experiments [163]. They state that co-adsorbed NO and CO species inhibit the dissociation of NO; however, dissociation improves under the presence of empty sites and adsorbed N atoms at the nearest site. Within this temperature range, they discover that adsorbed NO and CO molecules react to form narrow CO_2

and N_2 production peaks for a short period of time also known as surface explosion. Under the presence of CO and NO diffusion, the TPR spectra shifts towards lower temperatures indicating the production of CO_2 and N_2 occurs between 400 and 410K. Moreover, due to the mobility of the NO and CO species, the probability for NO dissociation is relatively high. This explosive phenomenon shifts towards the lower temperature region; i.e., from 422 to 402K, as the diffusion rate increases from zero to $30s^{-1}$. Therefore, they indicate that the diffusion properties of CO and NO molecules are important with respect to the explosive phenomenon.

3.2 REACTION HISTORY SUMMARY

Research began for the NO and CO reaction over a platinum washcoat with alumina support in the early 1970s [103,164]. These early efforts focused on the kinetics of the reaction and the stable formation of isocyanate and ammonia species [103,104]. During this time, investigators began including relative studies of the platinum catalysts in comparison to other PGMs, like rhodium and ruthenium. They determined that platinum is comparatively less reactive than rhodium and ruthenium [104]. Moreover, adsorption profile experiments of CO and NO molecules during this decade provided information about their relative bond strength with platinum [104,105,164]. The physical properties and bond strength of the adsorbed species provided vital information for the initiation of detailed reaction mechanisms. Based on their experiments, researchers initially believed that the reaction kinetics follow a Langmuir-Hinshelwood type mechanism following the Eqns. (85), (88), (89), (90), (91), (92), and (93) with stable NCO formation. They additional believed that the isocyanate species acts as a reaction inhibitor [105-107]. Later researchers discovered that isocyanate species formed over Al_2O_3 substrates were unstable when compared to MgO and SiO_2 substrates [108]. Moreover, the

literature demonstrates that adsorbed oxygen under lean conditions and adsorbed CO molecules during rich conditions can inhibit the reaction mechanism [109].

In the early 1980s, researchers began to explore the reaction kinetics with respect to emission regulations. Comprehensive detailed kinetic mechanisms were proposed utilizing a clear insight into the adsorption profiles of NO and CO molecules [111,112]. As discussed earlier, these reaction mechanisms were based on the relatively strong adsorption of CO with strong chemical interactions between adsorbed NO and CO [112,113]. In the mid 1980's, the autocatalytic behavior of the reduction reaction included the discussion of surface explosion of the products occurring around 400K [114]. Concurrently, researchers began including the influence of structural changes in the platinum catalyst in their L-H reaction mechanism [114,116,125]. They determined that the reaction proceeds with the dissociation of NO as the rate-determining step with its rate increasing above 450K [118-120]. Moreover, NO and CO mechanisms began to include the decomposition of isocyanates under lean conditions depending on the structure of platinum [118,119].

When the 1990s began, researchers were examining the kinetics based on oscillations in the reaction and the face structure of platinum catalytic material [121-123,126,129]. These oscillations occur due to the surface transition between square (1×1) and hexagonal faces of the Pt catalyst. They find that a detailed mechanism consisting of Eqns. (88), (89), (90), (91) and (92) agrees well with these oscillatory characteristics [122,123,126-129]. Moreover, during this time, the literature examined the bimolecular reaction based on adsorption and desorption characteristics [124,139] with open surface Pt_{100} catalysts found to be more active with respect to NO dissociation [127]. Later in this decade, the focus shifted to oscillations under reduction and oxidation conditions and observations indicated that strongly adsorbed CO molecules deactivate

the catalyst under reducing conditions [132,134]. With an increasing emphasis on greenhouse gases, Sadhankar and Lynch [136] described a detailed kinetic mechanism with N_2O as a reaction intermediate based on their transient experimental results [136,138]. They suggest that N_2O formation increases with an increase in NO partial pressures and decreases rapidly with an increase in NO conversion [136,138,144]. Findings in the literature additionally document that formation of N_2O is high in the temperature range of 523 to 573K, but decreases drastically above 673K [139,144]. Since cold start engine tests have a large impact on emission regulations, researchers around this time found in necessary to investigate emissions at low temperatures [165]. As a result, they theorize that NCO becomes favorable around 380K at high CO partial pressures, but it dissociates rapidly above 400K through Eqn. (93) [165]. Additional advancements in catalyst preparation techniques found that pressed platinum catalysts prepared by micro-emulsion methods have high NO conversion characteristics and a high thermal resistance towards sintering [141,147].

Recent work targets accurate measuring techniques to study the NO turnover rate with respect to their adsorption bands, structural changes and dispersion [145,146,156]. NO molecules adsorb in a linear form, and CO molecules occur in linear and bridged structures with the linear bonds stronger than the bridged structures [156,160]. Researchers additionally illustrate that NO adsorption energy increases with an increase in coverage [146]. Most researchers support the L-H mechanism proposed in the 1990s with considerable N_2O formation and strong CO adsorption as characteristics of the model [22,148-151,153,160]. They find that the rate of formation of CO_2 increases above 400K and the recombination of nitrogen atoms is the only step for nitrogen formation because of the lack of experimental evidences for other nitrogen formation steps [158]. Moreover, the rate of NO dissociation varies with the respect to

the structure of platinum i.e., NO dissociation is rapid over square phase platinum structures [21,154,158]. In-depth studies on detailed mechanisms provide slightly different reaction steps for nitrogen formation [159] and oscillatory studies reveal that the diffusion of NO and CO molecules are important for characterizing a precise detailed mechanism along with the explosive phenomenon [159,162,163].

3.3 DETAILED REACTION MECHANISM

Based on the analysis presented, the author feel that NO reduction by CO over platinum/aluminum surface occurs via the following steps:

- NO and CO Adsorption
- NO Dissociation
- CO_2 Formation
- N_2O Formation
- N_2 Formation

In this mechanism, the formation of NCO occurs rapidly at high NO partial pressures but it decomposes at real time operating temperature conditions for catalytic converter and so, the detailed reaction mechanism do not consider NCO formation and its subsequent decomposition. It is known from the history of the reaction mechanism that NCO is unstable over Pt/Al_2O_3 [105,107,134] and Pt_{100} [108]. Moreover, the adsorption of oxygen molecules is relatively small as compared to CO and NO adsorption, and the mechanism neglects its use because of its rapid formation to form CO_2 from monatomic oxygen [105,148,150,157]. Finally, the formation of $Pt{\cdot}NO_2$ [105,148,153], bimolecular steps [139,153] and the diffusion of the reacting species [146] over the surface are negligible in this reaction mechanism.

3.3.1 NO and CO Adsorption

The first step in the detailed reaction mechanism is the adsorption of the reacting species NO and CO over the platinum surface. Researchers find that NO and CO adsorb non-dissociatively [105] and the sticking coefficients of the species are relatively high and independent on both temperature [124] and coverage [112]. However, the sticking coefficient and desorption temperature of adsorbed NO is slightly influenced by the strong adsorption of the CO molecules [124]. These CO molecules act as an inhibitor due to their low adsorption enthalpy [109,112,114,139,148,162,165]. Thus, the accumulation of adsorbed CO tends to reduce the number of vacant sites for NO dissociation [118,121,122,134,160]. Unlike NO molecules, the desorption temperature of CO is independent of partial pressures and has higher desorption temperature above 450K when compared to NO [134,158]. Moreover, CO molecules do not form an impenetrable island over Pt catalysts [112-114] and, therefore, NO molecules adsorb even during rich conditions through bridged CO structures. In addition, it is found that the NO adsorption occurs over reduced Pt sites [107]. The literature illustrates a negative reaction order of CO concentration [149] due to strong adsorption and suggests that CO is more likely to adsorb than NO over Pt surface. Thus, the first two steps towards the detailed reaction mechanism follow Eqns. (88) and (89) respectively. As for a bonding angle, researchers determined that adsorbed CO frequently forms linearly atop and bridged structures [156,160] while adsorbed NO is equally likely to form a linear or bridged structure [107,146,148,156,157].

3.3.2 NO Dissociation

Dissociation of NO via Eqn. (90) is the second step in the reaction mechanism with adsorbed NO molecules dissociating relatively easily at temperatures above 400K [103,105,119,146,151]. The historical review indicates that the dissociation of NO depends

upon the concentration of CO molecules and this attribute differentiates the platinum catalysts apart other PGMs. In this case, these characteristics change with the increase in the temperature, vacant sites and the desorption temperature above 450K of the CO molecules [124,134]. In addition, researchers find that NO dissociation is slow in spite of this low dissociation energy because of the high dispersion of platinum over the alumina substrate. This makes it difficult for NO molecules to find vacant sites among the strongly adsorbed CO molecules and dissociate above 400K. Thus, similar to others, the authors believe that the NO dissociation step is the rate-determining step [122,134,148].

3.3.3 CO_2 Formation

Oxygen formed during the dissociation reaction of NO is considered stable over the surface, but in the presence of CO it reacts rapidly to form CO_2 above 400K via Eqn. (91) [22,108,148,160]. The formation of CO_2 leads to an increase in NO adsorption and NO dissociation respectively. Since dissociation of adsorbed CO is highly negligible due to the strong bond between the C and O atoms, the L-H mechanism for the formation of CO_2 through the dissociated oxygen from CO is not considered. Platinum is reduced during the L-H mechanism that produces CO_2, and, in turn, this reduced platinum is highly effective for NO dissociation i.e., the adsorbed oxygen over platinum reacts with the adsorbed CO through L-H mechanism and thus reduces the platinum site due to the lack of oxygen [108].

3.3.4 N_2O formation

The historical summary indicates to the author that it is reasonable to include N_2O formation under the following conditions. N_2O occurs at temperatures under 400K which is below the NO light-off temperature [139]. The amount of N_2O will increase with a rise in NO coverage because of the inhibition of the NO dissociation reaction, and the formation of N_2O

decreases with an increase in the NO conversion [135,136,138]. N_2O will form via an L-H mechanism through Eqn. (93) in the temperature range between 250 and 350K. The literature illustrates that there is no ready adsorption of N_2O gas because of its high adsorption energy as compared to that of NO and CO species. Thus, there is always a small amount of N_2O formation at the outlet during the NO and CO reaction over Pt catalysts. Moreover, the literature suggests the formation of N_2O happens only through the dissociation reaction and not through a bimolecular reaction of adsorbed NO and CO molecules [139]. Unlike rhodium catalysts, N_2O dissociation occurs slowly over platinum, and it is experientially shown that the decomposition of N_2O is very slow and less than six percent even at 773K over Pt/Al_2O_3 [142]. Moreover, gas phase N_2O is not an intermediate in the NO and CO reactions kinetics during the production of nitrogen. However, the author note that desorption and dissociation steps are still controversial when reviewing the history of N_2O studies.

3.3.5 N_2 formation

Nitrogen primarily forms through the recombination step of nitrogen atoms as indicated by Eqn. (92) [105,107,114,120,121,123,135,138,148]. Moreover, its formation is significantly high above 673K. Apart from this recombination step, nitrogen can also form through the disproportional reaction of NO and N atoms through an L-H mechanism. However, the author neglect this option because no experimental evidence exists to warrant its inclusion [153] and this step is typically not indicated when incorporating the N_2O formation step as in Eqn. (93). Since nitrogen molecules desorbed in the temperature range between 400 and 700K based on their coverage, they rapidly release when formed under typical catalytic operating temperatures. Now, let us derive the global rate expression based on the detailed reaction steps.

3.4 GLOBAL RATE EXPRESSION

For completeness, this section presents the global kinetic mechanism of the NO and CO reaction over Pt/Al_2O_3 as a function of the rate-determining step (RDS) depending on relative concentrations of NO and CO. Moreover, this section includes a theorized N_2O global kinetic mechanism based on the historical review.

The formulation of the mechanism begins with inlet of CO, NO and inert gas streams. In which, CO adsorption occurs first due to the affinity and their corresponding forward and reverse rate equations are given below respectively:

$\overline{R}_{86} = k_{86} p_{CO} \theta_{Pt}$	(115)
$\overline{R}_{-86} = k_{-86} \theta_{Pt \cdot CO}$	(116)

Under equilibrium, the rates become equal:

$k_{86} p_{CO} \theta_{Pt} = k_{-86} \theta_{Pt \cdot CO}$	(117)

with the equilibrium constant in atm^{-1} defined as:

$K_{CO} = k_{86} / k_{-86}$	(118)

The forward and reverse rate equations for NO adsorption are respectively:

$\overline{R}_{87} = k_{87} p_{NO} \theta_{Pt}$	(119)
$\overline{R}_{-87} = k_{-87} \theta_{Pt \cdot NO}$	(120)

Similarly, at equilibrium the following balance is generated:

$k_{87} p_{NO} \theta_{Pt} = k_{-87} \theta_{Pt \cdot NO}$	(121)

where K_{NO} in atm^{-1}:

$K_{NO} = k_{87} / k_{-87}$	(122)

Assuming that the dissociation reaction, Eqn. (90) proceeds only in the forward direction, the corresponding reaction rate is:

$\overline{R}_{88} = k_{88}\theta_{\text{Pt·NO}}\theta_{\text{Pt}}$	(123)

As the literature suggests, utilizing this reaction as the RDS, a global reaction expression in terms of $\text{molm}^{-2}\text{s}^{-1}$ is obtained by equating Eqns. (119) and (122) through solving for the associated coverage fractions of adsorbed CO and NO only:

$\theta_{\text{Pt·CO}} = K_{\text{CO}}p_{\text{CO}}\theta_{\text{Pt}}$	(124)
$\theta_{\text{Pt·NO}} = K_{\text{NO}}p_{\text{NO}}\theta_{\text{Pt}}$	(125)

Substituting Eqn. (125) in Eqn. (123),

$\overline{R}_{88} = k_{88}K_{\text{NO}}p_{\text{NO}}\theta_{\text{Pt}}^2$	(126)

Since there is a rapid formation of CO_2 from adsorbed CO and adsorbed oxygen atoms above 400K; the amount of oxygen coverage over Pt is negligible and so, the amount of vacant sites is given by:

$\theta_{\text{Pt}} = \left(1-\theta_{\text{Pt·NO}}-\theta_{\text{Pt·CO}}\right)$	(127)

Substituting Eqns. (124) and (125), the coverage fraction for platinum is found to be:

$\theta_{\text{Pt}} = \dfrac{1}{\left(1+K_{\text{CO}}p_{\text{CO}}+K_{\text{NO}}p_{\text{NO}}\right)}$	(128)

Finally, by substituting Eqn. (128) into Eqn. (126) the author obtain the following global reaction expression considering the dissociation of NO as the RDS:

$\overline{R}_{\text{NO}} = \overline{R}_{88} = \dfrac{k_{88}K_{\text{NO}}p_{\text{NO}}}{\left(1+K_{\text{CO}}p_{\text{CO}}+K_{\text{NO}}p_{\text{NO}}\right)^2}$	(129)

where, k_{88} is found to be the rate constant for NO dissociation step in terms of $\text{molm}^{-2}\text{s}^{-1}$ with p_{NO} and p_{CO} the partial pressures of the NO and CO species respectively. This expression is similar to the reaction rate developed by Granger et al. [138] and it can be used for competitive adsorptions of NO and CO.

As indicated in the previous section, the bimolecular step of the adsorbed CO and NO molecules through Eqn. (99) does not influence this detailed mechanism. Hence, the authors neglect this reaction step in the reaction mechanism and the formation of CO_2 from adsorbed CO and oxygen atom is rapid. Therefore, the dependence of CO pressures is negligible in the global rate expression for the rate-determining step.

Because of potential need to predict N_2O production for future emission regulations, the author include here a global expression for the formation of N_2O over Pt/Al_2O_3 catalyst based on the detailed reaction mechanism. The historical review indicates that the formation of N_2O occurs at high NO pressures/lean conditions and at temperatures less than 400K. Since the N_2O formation temperature is lower than the NO light-off temperature, the formation of nitrogen through Eqn. (92) is neglected for finding the global expression. Considering high NO pressures and negligible N_2O re-adsorption, only the forward reaction rate is important in the corresponding N_2O detailed step:

$\overline{R}_{91} = k_{91}\theta_{\mathrm{Pt\cdot NO}}\theta_{\mathrm{Pt\cdot N}}$	(130)

Here, the platinum vacant site (θ_{Pt}) is given by:

$\theta_{\mathrm{Pt}} = 1-\left(\theta_{\mathrm{Pt\cdot NO}} + \theta_{\mathrm{Pt\cdot CO}} + \theta_{\mathrm{Pt\cdot N}} + \theta_{\mathrm{Pt\cdot O}}\right)$	(131)

The above equation Eqn. (131) contains nitrogen and oxygen atom coverage factors added to the previous platinum vacant site Eqn.(127) and this is due to the high NO pressures and low temperatures conditions. The formation of CO_2 and N_2 is found to be negligible below 400K and hence, it becomes important to calculate the coverage factor of nitrogen and oxygen atoms over Pt. Moreover, the endothermic reaction for formation of NO_2 from adsorbed oxygen atom and adsorbed NO is found to occur above 475K [166-168]; the formation of NO_2 is not considered in finding the global reaction mechanism.

The coverage factors $\theta_{Pt\cdot N}$ and $\theta_{Pt\cdot O}$ can be calculated by applying a quasi-steady-state approximation to the nitrogen and oxygen adsorbed species respectively:

$\frac{d\theta_{Pt\cdot N}}{dt} = k_{88}\theta_{Pt\cdot NO}\theta_{Pt} - k_{91}\theta_{Pt\cdot NO}\theta_{Pt\cdot N} - \theta_{Pt\cdot N} \approx 0$	(132)
$\frac{d\theta_{Pt\cdot O}}{dt} = k_{88}\theta_{Pt\cdot NO}\theta_{Pt} - \theta_{Pt\cdot O} \approx 0$	(133)

The last term in the Eqns. (132) and (133) corresponds to the non-reactive adsorbed nitrogen and oxygen atoms over the Pt surface. Eqns. (125) and (132) allow for obtaining the coverage fractions:

$\theta_{Pt\cdot N} = \frac{k_{88}\theta_{Pt\cdot NO}\theta_{Pt}}{1+k_{91}\theta_{Pt\cdot NO}}$	(134)
$\theta_{Pt\cdot O} = k_{88}\theta_{Pt\cdot NO}\theta_{Pt}$	(135)

Substituting Eqns. (134) and (135) into Eqn. (131) and using Eqns. (124) and (125) yields:

$\theta_{Pt} = \frac{1}{\left[1+K_{CO}p_{CO}+K_{NO}p_{NO}+\frac{k_{88}K_{NO}p_{NO}}{1+k_{91}K_{NO}p_{NO}}+k_{88}K_{NO}p_{NO}\right]}$	(136)

Now, Eqns. (127) and (136) are substituted in Eqn. (132) to give the rate expression for the formation of N_2O in terms of $molm^{-2}s^{-1}$ is:

$\overline{R}_{91} = \frac{k_{88}k_{91}\left(K_{NO}p_{NO}\theta_{Pt}\right)^2}{\left(1+k_{91}K_{NO}p_{NO}\theta_{Pt}\right)}$	(137)

where, θ_{Pt} is given by the Eqn.(136) and k_{88} is in $molm^{-2}s^{-1}$ and k_{91} is dimensionless.

The above expression for the formation of the N_2O considers the effect of oxygen and carbon monoxide coverage factor and neglects the recombination step as it occurs above 600K. This gives the global rate expression for the formation of N_2O over Pt/Al_2O_3 in the NO reduction mechanism.

3.5 CONCLUSION

This paper provides a comprehensive review of NO reduction by CO over a platinum washcoat with alumina substrate. The authors find that the adsorption of CO is greater than the adsorption of NO over Pt with a relatively high self-inhibiting property of CO molecules under high CO concentrations. A thorough historical examination illustrates that the reaction mechanism follows five fundamental steps: (I) CO and NO Adsorption; (II) NO Dissociation; (III) CO_2 Formation; (IV) N_2O Formation; and (V) N_2 Formation. A proposed detailed reaction mechanism from this analysis suggests that the reaction proceeds via a Langmuir-Hinshelwood pathway unlike rhodium catalysts that follow both an L-H and Eley-Rideal mechanism. History indicates that NO dissociation is the rate-determining step because of its dispersion over the alumina substrate. The creation of N_2O in the mechanism is still under research, but from past studies, researchers believe that the formation of N_2O occurs at low temperatures and at high NO pressures. Furthermore, the literature demonstrates that the catalytic activity of the platinum metal in dissociation of NO molecules decreases with an increase in dispersion or a decrease in platinum size over an alumina substrate. Research is still required to finalize these effects under realistic catalytic converter conditions.

In the next Chapter, the fundamental knowledge gained through detailed reaction mechanisms and global rate expressions are utilized in the modeling of packed bed reactor.

CHAPTER 4
ONE-DIMENSIONAL PSEUDO-HOMOGENEOUS PACKED BED MODELING

4.0 HISTORY OF PSEUDO-HOMOGENEOUS CHEMICAL SPECIES EQUATION

It is important to understand the fundamentals of the pseudo-homogenous one-dimensional model in order to formulate the chemical species equation. When the packed bed under study does not have a significant length in the radial direction, for instance: less than 2 cm in the radial direction with 6 cm in axial direction, simplification allows modeling in one-dimension to be sufficient. In addition, since the flow through the packed bed is often relatively small in comparison to the speed of sound (Ma « 0.3), modelers can often assume dynamic incompressibility to further simplify the governing equations [30]. As a result, only the species and energy equations require solving. If the pressure drop is deemed to be important, experimental results indicate that the Ergun equation [169], derived from the conservation of momentum, accurately models this phenomenon over the packed bed reactor. The pseudo-homogeneous incorporation comes into the model by coalescing the properties of the solid (pellets) and fluid (exhaust gas) into a single governing equation while assuming a negligible pressure drop. This allows one equation each for the governing equations of species and energy, instead of the requirement of modeling both the solid and fluid phases independently as typically seen in monolithic converter simulations. The assumption of uniform catalyst pellet exterior further simplifies the task to omit the requirement of including catalyst characterization in the model [170]. This section presents a history of the development of the pseudo-homogeneous

model for the chemical species equation. A following section will document the energy equation.

Taylor in 1953 and Aris in 1956 [171,172] describe a lumped pseudo-homogeneous model for the species equation when the transverse diffusion time is much smaller than the advection time with axial mixing. They find that the molecules move at an average axial velocity similar to the plug flow model, but some degree of mixing is always present e.g., some molecules may move faster or slower than the average velocity. Moreover, this axial mixing results from the random velocity fluctuations of molecules travelling in the reactor that they reason as the degree of mixing of fluids due to the molecular diffusion. Due to this effect, they include a dispersion term and referred to as the dispersed plug flow model. This model gives a similar solution to the two-dimensional advection-diffusion equation when replacing the diffusion coefficient of the plug flow model with the dispersion coefficient.

$$\frac{\partial \bar{\mathbf{C}}}{\partial t} + u_s \frac{\partial \bar{\mathbf{C}}}{\partial x} = \mathbf{D}_I^{eff} \frac{\partial^2 \bar{\mathbf{C}}}{\partial x^2} - \bar{\mathbf{R}} \qquad (138)$$

In this equation, the indicated concentration of the species is the mean or volume-averaged concentration which combines the different phases that changes as a function of time, while advecting through the mixture as indicated on the left hand side of the equation. The first term on the right-hand side includes an effective dispersion (not diffusion) coefficient and the last term on this side incorporates the reactions occurring on the surface.

In 1965, McGuire and Leon [173] analyzed the stability of a packed-bed reactor and present a lumped model for the species and energy equations with the chemical reactions happening on the surface of the pellets:

$$\varepsilon \frac{\partial \bar{\mathbf{C}}}{\partial t} = \mathbf{D}^{eff} \frac{\partial^2 \bar{\mathbf{C}}}{\partial x^2} - \bar{\mathbf{R}}$$	(139)

They include a porosity term, ε, in front of the time-change of species to incorporate the space within the packed-bed particles; hence, this model requires consideration of the porosity of the interface. Furthermore, they write the reaction rate expression as a function of the surface composition and temperature.

In 1972, Harned [13] investigates the performance of packed-bed catalytic converters using a one-dimensional flow model and assumes negligible flow diffusion effects. To provide consistency, model nomenclature conversion occurs here for comparison purposes:

$$\varepsilon u_s \frac{\partial \mathbf{X}}{\partial x} = -\frac{\bar{\mathbf{R}}}{\bar{\rho}}$$	(140)

Instead of modeling the concentration of the species, Harned uses mole fractions that provide the same results since the assumption of dynamic incompressibility is inferred [174]. Harned's work explains that for automotive type converters, the time-change of species term in the governing equation is small and does not significantly influence the model solution. Moreover, this work calculates the mass and heat transfer coefficients using Wicke's model [175].

Harned mentions that there are three distinct catalytic reaction regimes based on an increase in temperature from warm-up to 700^{o}C. The first regime is when reaction rates are low and the diffusion flux is insignificant. The second regime is when there is an increase in diffusion flux represented by an increase in the pore diffusion and the effectiveness factor reduces gradually with pore diffusion controlling the regime. The last regime involves the diffusion flux governing the reaction rate through boundary layer from the bulk gas stream and thus extra pellet diffusion governs the reaction. In this region, the chemical reaction zone is restricted to a small portion of the bead volume near the external pellet surface. Harned

considers the reaction occurring to be of a first order dependency regardless of the intrinsic kinetics of the species. These findings provide information for the formulation of an effectiveness factor and diffusivity based on the regime. However, the analysis of these regimes and their formulation is beyond the scope of this paper's research.

In the same year, Eigenberger [176] proposed a heterogeneous model that this paper combines for consistency by merging both solid and fluid phases into the following pseudo-homogeneous model.

$$\varepsilon \frac{\partial \bar{\mathbf{C}}}{\partial t} + u_s \frac{\partial \bar{\mathbf{C}}}{\partial x} = -G_{ca} \bar{\mathbf{R}} \qquad (141)$$

Eigenberger assumes that heat conduction only takes place in the catalyst phase and suggests that the model reduces down to a few solutions for steady state conditions.

Two years later, Ferguson and Finlayson [27] study the mathematical models of automobile packed bed reactors for the reduction of nitric oxide over various catalysts. They compare the models under the regulated Federal Test Procedure as follows:

i. Quasi-static – In this model, all the processes are steady-state except for the solid temperature and inlet conditions. Furthermore, the temperature is constant throughout the catalyst with only a temperature change at the boundary. This approximation recognizes that thermal response of the packed bed catalytic material governs the time response of the system. They suggest utilizing the Quasi-static model for small time-steps resulting in reasonable computational time limited only by the desired accuracy.

ii. Simple – They obtain this model by simplifying the quasi-static model through reducing the diffusion and reaction components into a first order isothermal reaction

i.e., the reaction takes place at a constant temperature. This results in an analytical calculation of outlet concentrations.

iii. Fully dynamic – This simulates all of the equations considering transient conditions and leads to a set of numerically stiff ordinary differential equations. It increases computational time and limits the time step used in the dynamic model by stability. They proposed a heterogeneous model considering radial effects and it has been modified based on pseudo-homogeneous assumptions:

$$\varepsilon \frac{\partial \bar{\mathbf{C}}}{\partial t} + u_s \frac{\partial \bar{\mathbf{C}}}{\partial x} = \mathbf{D}^{eff} \frac{\partial^2 \bar{\mathbf{C}}}{\partial x^2} - G_{ca} \bar{\mathbf{R}} \quad (142)$$

In 1980, Robertson [177] describes a model of the packed bed catalytic converter that predicts the temperature distribution and converter efficiency during catalyst warm-up. This one-dimensional species equation considers concentration of the chemical species from the exhaust gas to the surface of the pellets with the reaction at the surface of the pellets:

$$u_s \frac{\partial \bar{\mathbf{C}}}{\partial x} = -G_{ca} \bar{\mathbf{R}} \quad (143)$$

The above equation uses a quasi-static assumption neglecting transient terms because the dominant time-dependent behavior is the relatively large heat capacity of the catalyst's pellets. This model additionally neglects intrapellet diffusion.

Concurrently, Oh and Cavendish [178] develop a one-dimensional model of a spherical catalyst pellet in contrast to modeling axial flow through a bed of pellets as given below:

$$\varepsilon(r) \frac{\partial \bar{\mathbf{C}}}{\partial t} = \frac{1}{r^2} \frac{\partial}{\partial r} \left[\mathbf{D}(r)^{eff} r^2 \frac{\partial^2 \bar{\mathbf{C}}}{\partial r^2} \right] - G_{ca} \bar{\mathbf{R}} \quad (144)$$

In this model, the porosity and diffusion values change as a function of the radial direction through the pellet. The computations based on their model show the influence of catalyst design

parameters and converter operating conditions on the light-off behavior of the catalyst pellets. They find that low pellet density and high exhaust gas flow rates favor a lower temperature light-off conversion. Moreover, a decrease in effective diffusivity in the pellets has a trade-off between high and low catalyst activities with respect to warm-up temperatures. Their results indicate that the reaction rate through a single pellet can change radially before warm-up temperatures; whereas, the temperature profile becomes relatively flat above its reaction temperature. This illustrates the reasonable assumption of uniform pellet temperature in modeling packed bed catalytic converters.

A few years later in 1982, Wakao and Kaguei [25] investigate the heat and mass transfer of packed bed reactors in detail and model the species equation with the reaction rate constant modeled as a first order irreversible catalytic reaction under isothermal conditions:

$$u_s \frac{\partial \bar{\mathbf{C}}}{\partial x} - \mathbf{D}_I^{eff} \frac{\partial^2 \bar{\mathbf{C}}}{\partial x^2} + G_{ca} \frac{\bar{\mathbf{R}}}{\varepsilon} = 0 \qquad (145)$$

This model utilizes a dispersion coefficient suggesting that it depends on molecular diffusivity in fluid phase, effective diffusivity in the solid pellet and additionally on the chemical reaction of the particles. They determine that the dispersion coefficient is twenty times larger than the fluid molecular diffusivity for a packed bed undergoing fast chemical reactions; whereas, the dispersion coefficient is one quarter the value of the molecular diffusivity.

In 2000, Winterberg et al. [7] demonstrates that the quasi-homogeneous, one-phase model provides good accuracy in modeling packed bed reactors with chemical reactions. They modify the species equation to neglect variation in bed porosity, radial thermal conductivity and radial mass dispersion:

$$\varepsilon \frac{\partial \mathbf{X}}{\partial t} = \mathbf{D}_I^{eff} \frac{\partial^2 \mathbf{X}}{\partial x^2} - u_s \frac{\partial \mathbf{X}}{\partial x} - G_{ca} \frac{\bar{\mathbf{R}}}{\bar{\rho}_s} \quad (146)$$

Again, this work indicates the use of an axial dispersion coefficient instead of diffusion constant.

Recent work by Younis investigates the flow of hydrogen and air through a packed bed reactor considering the flow to be laminar, unsteady, one-dimensional and adiabatic [179]. Moreover, Younis assumes that the thermal properties of the pellets such as the density specific heat and porosity are uniform and constant. In addition, the mathematical model includes both a gas phase and catalytic surface species equation, simplified into the following:

$$\frac{\partial \mathbf{Y}}{\partial t} + \frac{\partial \left(u_s \mathbf{Y}\right)}{\partial x} = \mathbf{D}^{eff} \frac{\partial^2 \mathbf{Y}}{\partial x^2} - \frac{G_{ca} \bar{\mathbf{R}} \mathbf{W}}{\rho_s} \quad (147)$$

Research in modeling packed bed reactors started in the late 1960s with the focus mainly on finding the tortuosity, diffusion and thermal conductivity coefficients as illustrated in a following section [180-185]. As computational technology improved, researchers developed detailed chemical species equations to include radial effects with more nonlinearity factors [13,27,178,186,187] . This shifted into a trade-off between accuracy, with respect to varying concentrations and temperatures, and computational efficiency. Researchers find that the pseudo-homogeneous model with the inclusion of advection and an effective diffusion coefficient provides a good approximation of the flow pattern [25,179,188]. Moreover, the presence of concentration gradients and variations in velocity of molecules through packed bed induces mixing in the radial direction. When modeling mixing, researchers utilize a dispersion term in the pseudo-homogeneous species equation instead of an effective diffusion coefficient [7,25,171,172,189-191]. A subsequent section illustrates the possible options for either a dispersion or effective diffusion term; whereas, the next section derives the pseudo-homogeneous chemical species equation from first principles.

4.1 CHEMICAL SPECIES EQUATION

One method of modeling a packed bed reactor system is to model the fluid flowing in the interstitial space and the gas at the surface of the catalyst independently. For the gas flowing through the packed bed, the governing equation of chemical species in one-dimensional, compressible format is:

$$\varepsilon \frac{\partial\left(\bar{\rho}_s \mathbf{X}_s\right)}{\partial t} + \varepsilon \frac{\partial\left(\bar{\rho}_s u_s \mathbf{X}_s\right)}{\partial x} = \varepsilon \frac{\partial}{\partial x}\left(\bar{\rho}_s \mathbf{D}^{eff} \frac{\partial \mathbf{X}_s}{\partial x}\right) + \dot{n}_{s\to p} \tag{148}$$

where the first term on the left hand side describes the time-change of species within the interstitial space and the second term represents the advection of the species in the pores. Since the pore structure involves relatively small areas, diffusion effects become important and need to be included as shown in the first term on the right hand side of the equation. The history of this model illustrates the use of an effective diffusion vector for the species; a description will follow for this term later in this paper. The last term on the right hand side accounts for the mass transfer of species between the gas and the surface of the packed bed catalytic material (this term is well known in the one-dimensional monolithic catalyst modeling community [192]). It is included here in a non-descriptive manner, as it will not play a role in the final version of the pseudo-homogeneous chemical species governing equation. Of importance, this equation includes a void fraction or porosity term, since it involves only the gas in the interstitial region, which is a fraction of the total reactor volume.

For the gas adsorbed on the surface of the packed bed catalytic material, the governing equation of chemical species in one-dimensional compressible format is:

$$\left(1-\varepsilon\right)\frac{d\left(\bar{\rho}_p \mathbf{X}_p\right)}{dt} = -\dot{n}_{s\to p} - G_{ca}\bar{\mathbf{R}} \tag{149}$$

This equation includes a corresponding mass transfer term the right hand side to balance the previous interstitial gas equation. The terms from Eqns. (148) and (149) must cancel each other, as the fluxes are required to balance because they utilize the same surface areas [193]. A similar type of arrangement regarding this mass transfer term was seen in the one-dimensional monolithic catalyst modeling field when Harned [13] separated Kuo et al.'s model [194] into two distinct phases for the chemical species equations in the channel and on the surface of the catalyst. The last term on the right-hand side includes the influence of the reaction rates on the surface along with a catalytic surface area per unit volume term. Often this term is lumped into the reaction rate expression when calibration of the chemical kinetics occurs [192].

Unlike monolithic catalyst modeling involving a channel and surface, the distance between the interstitial space and the catalytic surface in a packed bed can be considered small enough to assume that the gas in the bulk is equivalent to the gas at the surface: $\mathbf{X}_s = \mathbf{X}_p = \mathbf{X}$. As a result, the two governing equations., (148) and (149) are added as follows while additionally writing the equation using concentration terms [193]:

$$\frac{\partial \bar{\mathbf{C}}}{\partial t} + \varepsilon \frac{\partial \left(u_s \bar{\mathbf{C}} \right)}{\partial x} = \varepsilon \frac{\partial}{\partial x} \left(\bar{\rho} \mathbf{D}^{eff} \frac{\partial \mathbf{X}}{\partial x} \right) - G_{ca} \bar{\mathbf{R}} \tag{150}$$

The species equation can be lumped into a single concentration term when the ratio of Knudsen to Molecular diffusivity is less than 0.1 and this limitation has been used for our modeling purposes [8].

Since the flow through a packed bed reactor is significantly less than the Mach number, often the assumption of dynamic incompressibility is made [195]. This is a common occurrence in the monolith catalyst modeling field [174,196]. Because the density is now assumed constant through the packed bed, the velocity must also be constant since mass flow into the packed bed

needs to be balanced by the mass flow out of the packed bed due to the continuity equation e.g. no accumulation of mass within the reactor. Another assumption to simplify the computational task is that the effective diffusivity of each species will not change significantly in the *x*-direction resulting in the following version:

$$\frac{\partial \bar{\mathbf{C}}}{\partial t} + \varepsilon u_s \frac{\partial \bar{\mathbf{C}}}{\partial x} = \varepsilon \mathbf{D}^{eff} \frac{\partial^2 \bar{\mathbf{C}}}{\partial x^2} - G_{ca} \bar{\mathbf{R}} \qquad (151)$$

As discussed in an earlier reference from the Dr. Christopher Depcik's results, the assumption of dynamic incompressibility is valid when there is not a significant pressure drop or temperature excursion. There is a considerable pressure drop due to the tortuous flow of the species over a lengthy packed bed with high Reynolds number; however, solving this version of the governing equations has a distinct advantage in terms of numerical run time [174]. Since solution of the chemical species equation is independent of the energy equation, this eliminates the constraint of the ideal gas law in a compressible system that creates a differential-algebraic set of equations. The previous historical review of the model illustrates that researchers are inferring dynamic incompressibility through their independent solution of the chemical species and energy equations.

One-dimensional catalyst modeling has determined that the time-rate of change of chemical species is much faster than that of the monolithic substrate [30]. As a result, the energy equation specifies the time-step of the simulation while the species equation goes to steady-state. Since packed bed pellets are on the same order of magnitude in terms of thermal properties of a monolithic substrate, and previous researchers in the packed bed field made this connection, this assumption is followed further simplifying the governing equation as follows:

$$\varepsilon u_s \frac{\partial \bar{\mathbf{C}}}{\partial x} = \varepsilon \mathbf{D}^{eff} \frac{\partial^2 \bar{\mathbf{C}}}{\partial x^2} - G_{ca} \bar{\mathbf{R}} \quad (152)$$

The species equation formulated above involves the advection effect of the fluid flow, effective diffusivity and reaction rate terms for each species over the catalyst pellet surface. This equation is similar to the models described in the previous section with respect to the steady state and diffusivity assumptions. The reaction rate source term of the catalyst and the advection term of the species concentration derived are slightly different from the previous models based on the assumptions and the fundamental equations of two phases. The method for calculating effective diffusion coefficient is dealt with in detail in the effective diffusion section.

As discussed in the beginning of the historical section, this version of the governing equation of chemical species is only valid during one-dimensional flow and any number of species. Most reactor studies in the laboratory that calculate chemical kinetics utilize only a small core of material without significant length in the radial direction. Moreover, advection will largely follow in the axial direction only. However, there is the potential for diffusion in the radial direction. To ensure that the model presented here remains valid, the mass transfer Biot number should be checked across all species [27,197]:

$$\mathbf{Bi}_m = \frac{\boldsymbol{\kappa} L_m}{\mathbf{D}^{eff}} < 10 \quad (153)$$

where, $\boldsymbol{\kappa}$ is the species mass transfer vector and L_m is the characteristic length in the radial direction. When the mass Biot number of each species is less than 10, the effectiveness factor of the pellet is found to be negligible i.e. the concentration in the pellet would be equal to the surface concentration and there is a negligible radial effect of diffusion of the species. Since the flow through a packed-bed follows a tortuous path, described in more detail later, the characteristic length should involve this factor as follows:

$L_m = \tau \cdot d_b$	(154)

where, τ is the tortuosity of the flow and d_b is the diameter of the pellets.

Hayes and Kolaczkowski [198] illustrate that the species mass transfer coefficient in packed beds needed in the Biot number calculation of Eqn. (153) can obtained using *j*-factors

$\boldsymbol{\kappa} = \dfrac{u_s \varepsilon j_D}{\mathbf{Sc}^{2/3}}$	(155)

This factor (j_D) for automotive converter design is found from Harned as [13,178] and it depends on the Reynolds number calculated from the axial flow velocity as:

$\varepsilon j_D = 0.667 / \mathrm{Re}^{0.481} \quad \text{where} \quad 10 < \mathrm{Re} < 300$	(156)

and the Schmidt number is computed from the mixture diffusivity:

$\mathbf{Sc} = \dfrac{\mu}{\rho_s \mathbf{D}_m}$	(157)

Therefore, calculation of the Schmidt and Reynolds number allows computation of the mass transfer coefficient in order to check the Biot number ensuring that a one-dimensional representation is valid.

4.2 HISTORY OF PSEUDO-HOMOGENEOUS ENERGY EQUATION

An isothermal experimental test requires only modeling of the chemical species equation in order to determine chemical kinetic parameters. However, since the hysteresis of the reactions on the surface can be important under light-off conditions, the energy equation is often included in the model solution to provide the thermal response of the packed bed reactor. In such a case, heat transfer due to convection can usually be neglected in relation to that of radiation and conduction [199,200]. Under low Reynolds number conditions and the dynamic incompressibility assumption, researchers find that there is not any appreciable difference

between a psuedo-homogeneous model and a two-phase model [27,201]. This is from the determination that under these conditions there is no difference between steady-state and transient methods for experimental calculation of an effective thermal conductivity parameter; hence, similar to the chemical species equation and diffusion, a single integrated model can include both fluid and surface phases using the appropriately calculated property [201]. Moreover, one-dimensional modeling of the energy equation assumes no radial changes with a lack of heat transfer through the wall. The above assumptions with the combined flat velocity profile imply that there is no radial gradient at the macroscopic level [198]. Similar to the chemical species equation, a check of the thermal Biot number will provide a check for correct use of the model.

With respect to the history of the energy equation, Harned initially studied the performance of packed-bed catalytic converters using a one-dimensional flow model with negligible flow dispersion effects [13]:

$$\left(1-\varepsilon\right)\rho c\frac{\partial T}{\partial t}+\varepsilon\rho_s c_p u_s\frac{\partial T}{\partial x}=G_{ca}\sum_{j=1}^{NM}\bar{\mathbf{R}}\bar{\mathbf{h}}+\dot{q}_{ext} \quad (158)$$

where the first term on the left hand side represents the energy storage term of the catalyst pellets, the second term models the transfer of heat energy through advection of gas between the pellets, and the first term on the right hand side describes the energy generated through catalytic endothermic or exothermic reactions. The last term on the right hand side is a measure of heat loss to the ambient:

$$\dot{q}_{ext}=\frac{4h_\infty}{D\varepsilon}\left(T-T_\infty\right) \quad (159)$$

Where, D is the diameter of the packed bed. Harned finds that for automotive type converters, the time rate of change, or energy storage term, in the energy equation is much larger than the

corresponding term in the chemical species equation as mentioned earlier. Hence, energy storage term sets the time-step of the simulation.

In the 1972, Eigenberger [176] proposed a two-phase model extending the equations of Liu and Amundson [202] by including heat conduction in the solid phase. The energy equation provided below is transformed based on the pseudo-homogeneous model assumptions:

$$\left[\varepsilon\rho_s c_p + (1-\varepsilon)\rho c\right]\frac{\partial T}{\partial t} + \rho_s c_p u_s \frac{\partial T}{\partial x} = \lambda^{eff}\frac{\partial^2 T}{\partial x^2} + G_{ca}\sum_{j=1}^{NM}\bar{\mathbf{R}}\bar{\mathbf{h}} \qquad (160)$$

This model utilizes a heat conduction term in the catalyst phase in order to predict the phenomenon where the maximum temperature moves to the front of the reactor driven by the backward conduction of heat. This finding is analogous to that of Oh and Cavendish who discover the same phenomenon in the monolithic catalyst modeling field in their 1982 paper [14].

Two years later, Vortmeyer and Schaefer [190] develop a single phase pseudo-homogeneous energy equation from a two-phase model and calculate a one-dimensional effective thermal conductivity coefficient developed from experimental tests involving two-dimensional measurements. They assume a small interphase time for heat transfer when compared to the time for advection:

$$(1-\varepsilon)\rho c\frac{\partial T}{\partial t} + \rho_s c_p u_s \frac{\partial T}{\partial x} = \lambda_l^{eff}\frac{\partial^2 T}{\partial x^2} + G_{ca}\sum_{j=1}^{NM}\bar{\mathbf{R}}\bar{\mathbf{h}} \qquad (161)$$

The above model neglects the thermal capacity of the gas phase when compared to the solid phase. The first term on the right hand side includes an axial effective thermal conductivity which is presented in a later section. Here, the axial effective thermal conductivity is the sum of the stagnant bed thermal conductivity, gas-solid heat transfer and intraparticle conduction.

At the same time, Ferguson and Finlayson [27] describe simple, quasi-static and dynamic models for the energy equation based on the assumptions discussed in the chemical species section. The energy equation provided below is for the dynamic model considering all processes in the transient state:

$$\left[\varepsilon\rho_s c_p + (1-\varepsilon)\rho c\right]\frac{\partial T}{\partial t} + \rho_s c_p u_s \frac{\partial T}{\partial x} = \lambda^{eff}\frac{\partial^2 T}{\partial x^2} + G_{ca}\sum_{j=1}^{NM}\bar{\mathbf{R}}\bar{\mathbf{h}} \quad (162)$$

From this, the quasi-static model neglects the energy storage term in gas phase when compared with the dynamic model.

In 1980, Robertson [177] describes a one-dimensional mathematical model for the analysis of a packed-bed catalytic converter considering heat transfer from exhaust gas to the catalyst pellets and support. The reaction takes place at the surface of the pellets with condensation and evaporation of water vapor occurring at the surface of the pellets:

$$(1-\varepsilon)\rho c\frac{\partial T}{\partial t} + \varepsilon\rho_s c_p u_s \frac{\partial T}{\partial x} = G_{ca}\sum_{j=1}^{NM}\bar{\mathbf{R}}\bar{\mathbf{h}} + \frac{\dot{q}_{cond}}{V_s} + \dot{q}_w \quad (163)$$

This model includes heat transfer due to condensation and evaporation of the water as:

$$\dot{q}_{cond} = r_{cond}\cdot h_{fg} \quad (164)$$

Where:

$$r_{cond} = h_D \varepsilon A(\omega - \omega_s) \quad (165)$$

Moreover, this model includes heat transfer with the converter wall:

$$\dot{q}_w = \frac{h_w A_w (T - T_w)}{\varepsilon_w \rho_w V} \quad (166)$$

This model neglects the accumulation of the energy in the gas phase and the heat loss from the converter walls to the ambient because of assumed adiabatic conditions.

Concurrently, as discussed previously, Oh and Cavendish [178] develop a one-dimensional model of a spherical catalyst pellet in contrast to modeling axial flow through a bed of pellets. Their proposed energy equation considers the radial effect through the spherical catalyst pellets:

$$\left[\rho_s(r)c_p(r)\right]\frac{\partial T}{\partial t}=\frac{1}{r^2}\frac{\partial}{\partial r}\left[\lambda(r)^{eff}\,r^2\,\frac{\partial T}{\partial r}\right]+G_{ca}\sum_{j=1}^{NM}\bar{\mathbf{R}}\bar{\mathbf{h}} \qquad (167)$$

This model of the energy equation provides information about the light-off temperature of the catalyst and the radial effect on each layer of the catalyst pellets for different physical and chemical properties.

Jumping ahead to 2000, Winterberg et al. [7] suggests modification of the energy equation to neglect the variation in bed porosity, along with omitting radial thermal conductivity:

$$\left[\varepsilon\rho_s c_p+\left(1-\varepsilon\right)\rho c\right]\frac{\partial T}{\partial t}+\rho_s c_p u_s\,\frac{\partial T}{\partial x}=\lambda_I^{eff}\,\frac{\partial^2 T}{\partial x^2}+G_{ca}\sum_{j=1}^{NM}\bar{\mathbf{R}}\bar{\mathbf{h}} \qquad (168)$$

This equation contains an axial thermal dispersion coefficient independent of the bed length and chemical reactions.

Recent work by Younis considers the thermal properties of the pellets, such as the density, specific heat and porosity, are assumed to be uniform and constant [179]. In contrast to the other models presented, radiation coming from the catalytic pellets is included in the effective thermal conductivity parameter. He includes this radiative heat transfer in the packed bed by making the effective thermal conductivity of the pellets a function of temperature e.g., the model augments the thermal conductivity of the porous bed with a radiative conductivity. In addition, Younis mathematical model includes both gas phase and catalytic surface species

equation with Arrhenius reactions of a single step global type. These heterogeneous equations condensed to a single energy equation are as follows:

$$\left[\varepsilon\rho_s c_p + (1-\varepsilon)\rho c\right]\frac{\partial T}{\partial t} + \varepsilon\rho_s c_p u_s \frac{\partial T}{\partial x} = \lambda^{eff}\frac{\partial^2 T}{\partial x^2} + (1-\varepsilon)G_{ca}\sum_{j=1}^{NM}\bar{\mathbf{R}}\bar{\mathbf{h}} + \varepsilon G_{ca}\sum_{j=1}^{NM}\bar{\mathbf{R}}_s\bar{\mathbf{h}}_s \quad (169)$$

with both heterogeneous and homogeneous reactions due to the conversion into this paper's pseudo-homogeneous model.

In the same year, Nield and Bejan publish a book on porous media describing different methods at which to calculate the energy equation when combining gas and surface phases [193]. In particular, they provide an understanding of the thermal conductivity term in their model formulation:

$$\left[\varepsilon\rho_s c_p + (1-\varepsilon)\rho c\right]\frac{\partial T}{\partial t} + \rho_s c_p u_s \frac{\partial T}{\partial x} = \lambda^{eff}\frac{\partial^2 \mathrm{T}}{\partial x^2} \quad (170)$$

The energy equation above is valid for an isotropic medium with negligible radiative effects, viscous dissipation and pressure drop. In this model, a local thermal equilibrium between solid and fluid exists: $T_s = T_p = T$. They state that the work done by the pressure change is negligible; therefore, the coefficient of volumetric thermal expansion (β) is not added to the left hand side of the energy equation:

$$\beta = -\frac{1}{\rho}\left(\frac{\partial \rho}{\partial T}\right)_p \quad (171)$$

A significant pressure drop within a packed bed reactor requires the incorporation of this β term in the energy equation through compressible flow. Moreover, they state that viscous dissipation is negligible in natural convection phenomenon i.e. the flow occurring due to a small amount of pressure difference neglects the viscous dissipation term.

In the beginning, researchers proposed an energy equation based on quasi-static assumptions by considering the reactor as a continuous phase with different source terms [13,27,177,188]. They initially considered the radial effect on the conductivity of pellets and various modes of heat transfer within the packed bed [7,178,179]. They based their formulations of the energy equation on intended packed bed reactor applications as seen in their methodology of changing source terms based on the temperature, ambient and flow conditions. Using the assumptions and information found in this historical summary, the next section describes the derivation of the pseudo-homogeneous energy equation for a one-dimensional packed bed reactor from first principles.

4.3 ENERGY EQUATION

Similar to the chemical species governing equation, computation of the energy equation for the interstitial gas follows by utilizing the assumption of dynamic incompressibility:

$$\varepsilon\rho_s c_p\left(\frac{\partial T_s}{\partial t}+u_s\frac{\partial T_s}{\partial x}\right)=\varepsilon\frac{\partial}{\partial x}\left(\lambda_s\frac{\partial T_s}{\partial x}\right)+\dot{q}_{s\to p} \qquad (172)$$

Where, first term on the left hand side describes the time-change of temperature of the gas within the interstitial space and the second term represents the advection of the gas in the pores. Since the pore structure involves relatively small distances, conduction effects may become important as demonstrated in the history of model development (from the denominator of the $\partial^2 T_s/\partial x^2$ term). Hence, the model includes this dependency in the first term on the right hand side of the equation. At this stage, the model does not include an effective thermal conductivity parameter and instead uses the thermal conductivity of the gas. Its inclusion will happen after combining the gas and surface phase energy equations.

Analogous to the species equation, the last term on the right hand side represents convective heat transfer between the gas and the surface of the packed bed catalytic material; again, this term is well known in the monolithic catalyst modeling community [30]. As it will not play a role in the final version of the pseudo-homogeneous governing equation, its inclusion here is in a non-descriptive manner. Of importance, this equation includes a void fraction or porosity term, since it involves only the gas in the interstitial region, which is a fraction of the total reactor volume.

The temperature of the solid material in the packed bed in one-dimensional format is:

$$\left(1-\varepsilon\right)\rho c\frac{\partial T_p}{\partial t}=\left(1-\varepsilon\right)\frac{\partial}{\partial x}\left(\lambda\frac{\partial T_p}{\partial x}\right)-\dot{q}_{s\to p}+G_{ca}\sum_{j=1}^{NM}\overline{\mathbf{R}}\overline{\mathbf{h}}+\dot{q}_{ext} \quad (173)$$

This equation includes a corresponding heat transfer term on the right hand side in order to balance the previous interstitial gas equation. The terms from Eqns. (172) and (173) must cancel each other, as the fluxes are required to balance because they utilize the same surface areas [193]. The second to last term on the right hand side includes the influence of endothermic and exothermic reactions on the surface along with a catalytic surface area per unit volume term. As discussed previously, often this term is lumped into the reaction rate expression during calibration of the chemical kinetics. The last term on the right hand side describes the influence of external heat transfer to the ambient discussed in more depth later in this section.

Similar to the chemical species equations, the distance between the gas and catalytic surface is small and is similar to what it is found in the porous walls within Diesel Particulate Filter modeling [203] along with the historical review of packed bed modeling, convection between the gas and surface far outweighs other contributions. Therefore, it is commonplace to

assume a local thermodynamic equilibrium with $T_s = T_p = T$ [190] . Adding the two governing equations results in the following:

$$\left[\left(1-\varepsilon\right)\rho c + \varepsilon\rho_s c_p\right]\frac{\partial T}{\partial t} + \varepsilon\rho_s c_p u_s \frac{\partial T}{\partial x} = \left[\left(1-\varepsilon\right)\lambda + \varepsilon\lambda_s\right]\frac{\partial^2 T}{\partial x^2} + G_{ca}\sum_{j=1}^{NM}\bar{\mathbf{R}}\bar{\mathbf{h}} + \dot{q}_{ext} \quad (174)$$

However, as Nield and Bejan state [193] and as indicated in the history of the model development, thermal conductivity is often represented as an effective parameter because it can be computed in a number of different manners based on the temperature and their corresponding heat transfer phenomenon. As a result, the governing equation of energy for the pseudo-homogeneous model equals:

$$\left[\left(1-\varepsilon\right)\rho c + \varepsilon\rho_s c_p\right]\frac{\partial T}{\partial t} + \varepsilon\rho_s c_p u_s \frac{\partial T}{\partial x} = \lambda^{eff}\frac{\partial^2 T}{\partial x^2} + G_{ca}\sum_{j=1}^{NM}\bar{\mathbf{R}}\bar{\mathbf{h}} + \dot{q}_{ext} \quad (175)$$

There will be a thorough investigation of the effective conductivity parameter provided later in this paper.

From monolithic catalyst modeling [174], the external heat transfer term includes the influence of convection and radiation:

$$\dot{q}_{ext} = \frac{4}{D}\left\{h_\infty\left(T_\infty - T\right) + \varepsilon_r\sigma\left(T_\infty^4 - T^4\right)\right\} \quad (176)$$

written incorporating the diameter of the packed bed reactor. In order for this term to be valid in model formulation, a check of the wall heat Biot number is required [27,170]:

$$\mathbf{Bi}_{w,h} = \frac{h_\infty D}{2\lambda^{eff}} < 1 \quad (177)$$

with the characteristic length computed from the external surface area of packed bed per unit length:

$$A = \pi D \quad (178)$$

and the total volume of the packed bed per unit length:

$$V = \frac{\pi D^2}{4} \quad (179)$$

as follows:

$$L_t = \frac{V}{A} = \frac{D}{4} \quad (180)$$

Similar to the mass transfer coefficient, calculation of the heat transfer coefficient of the reactor is possible using appropriate Nusselt number and Reynolds number of the pellet particles [13,204]:

$$Nu = 0.17\left(\mathrm{Re}_p\right)^{0.79} \quad (181)$$

with

$$\mathrm{Re}_p = \frac{\left(d_b u_s \rho_s\right)}{\mu} \quad (182)$$

And [198]

$$h_\infty = \frac{Nu \cdot \lambda_s}{L_t} \quad (183)$$

The wall heat Biot number limitation is used to eliminate the external heat transfer to the ambient, and the radial effect of the temperature can be neglected. It is further required to consider pellet heat Biot number as an additional limitation for using 'lumped temperature parameters' for the energy equation [205]. The pellet Biot number should be less than 0.1 in order to neglect intra-particle temperature gradients.

$$\mathbf{Bi}_{p,h} = \frac{h_\infty d_b}{2\lambda} < 0.1 \quad (184)$$

Further, the ratio of mass over wall heat Biot number is usually around the value of 10; and when this condition is reached the concentration and temperature profiles over the catalyst radius is negligible, and this condition is used for the modeling purposes to check the effect of temperature gradients [197].

The history of the use of the energy equation illustrates that the gas-phase accumulation term in this equation could be neglected because of its relatively low value [13,177,190]. In order to utilize this assumption properly without any degree of error requires the development of a proper criterion. Researchers have found that when the volumetric ratio of the heat capacities is less than 0.002, it is relevant to neglect the fluid phase heat capacity term in the energy equation [27,206].

$$C_r = \frac{\varepsilon \rho_s c_p}{(1-\varepsilon)\rho c} < 0.002 \qquad (185)$$

This section describes the one-dimensional energy equation with corresponding assumptions for the effective conversion of the two-phase, two-dimensional energy equation into a one-dimensional pseudo-homogeneous model. The following section explains the fundamental concepts of diffusivity and thermal conductivities for the efficient use of these coefficients in the species and energy equations respectively.

4.4 MOLECULAR AND KNUDSEN DIFFUSIVITIES

This section provides a detailed analysis of the molecular and Knudsen diffusivities in a packed bed reactor before moving on to the calculation of an effective diffusivity term in the species equation. The classification of both molecular and Knudsen diffusivities occurs based on the pore size. Molecular diffusion provides the dominant resistance to mass transfer in porous catalyst when pore radii are larger than one μm [198]. In comparison, Knudsen diffusivity is at a

maximum when pore radii are less than 50Å at standard pressure and temperature [198]. History illustrates that diffusion occurs in more than one coordinate direction due to the tortuous nature of the pores. In addition, effective diffusion is inversely proportional to the square root of its molecular weight and it is species specific as the pore diffusion in the gas phase varies inversely with the square root of the molecular weight. Hence, larger molecules have smaller diffusivities [25,207]. Moreover, mass transfer within the pores is negligible at small Reynolds numbers in spite of the nonzero species velocity of the reactants and products in the pores and diffusion dominates advective transport [207].

The theoretical computation of diffusion begins by calculating the binary diffusion constants between two species, *i* and *j*, from molecular kinetic theory [208,209]:

$$D_{ij} = \frac{3}{16}\frac{\sqrt{2\pi R_u^3 T_s^3 / \left(W_{ij}/1000\right)}}{A p_s \pi \sigma_{ij}^2 \Omega^{(1,1)} T_{ij}^*} \quad (186)$$

Where, σ_{ij} is the reduced collision diameter, or intermolecular separation at which the interaction potential between molecules vanishes, $\Omega^{(1,1)}$ is the collision integral, W_{ij} is the reduced molecular weight utilizing the molecular weight of the species

$$W_{ij} = \frac{W_i W_j}{W_i + W_j} \quad (187)$$

R_u is the universal gas constant; A is Avogadro's number and T_{ij}^* is the reduced temperature:

$$T_{ij}^* = \frac{k_B T_s}{\varepsilon_{ij}} \quad (188)$$

which includes Boltzmann's constant (k_B) and the potential well depth between the two molecules, ε_{ij}.

This depth of potential well is a measure of strength of the interaction as a balance between the repulsion from the Pauli Exclusion Principle and the attraction from van der Waals forces as formulated from the Lennard-Jones potential model. Therefore, its value is a function of the relative charge of the particles involved. For a polar molecule interacting with a polar molecule, or a non-polar with a non-polar:

$$\frac{\varepsilon_{ij}}{k_B} = \sqrt{\left(\frac{\varepsilon_i}{k_B}\right)\left(\frac{\varepsilon_j}{k_B}\right)} \quad (189)$$

When a non-polar molecule interacts with a polar molecule, an additional factor is included:

$$\frac{\varepsilon_{np}}{k_B} = \xi^2 \sqrt{\left(\frac{\varepsilon_n}{k_B}\right)\left(\frac{\varepsilon_p}{k_B}\right)} \quad (190)$$

Note that the Lennard-Jones parameters, ε and σ, are available in the literature for individual species [207,210].

The parameter ξ is:

$$\xi = 1 + \frac{1}{4}\alpha_n^* \mu_p^* \sqrt{\frac{\varepsilon_p}{\varepsilon_n}} \quad (191)$$

which is a function of the polarizability,

$$\alpha_n^* = \frac{\alpha_n}{\sigma_n^3} \quad (192)$$

and dipole moment of the species:

$$\mu_p^* = \frac{\mu_p}{\sqrt{\varepsilon_p \sigma_p^3}} \quad (193)$$

Polarizability relates to the movement of the electrons in the molecular cloud of the species resulting in an electrostatic force. The dipole moments are a function of the sharing of the electrons between atoms in a covalent bond and are not necessarily shared equally. The result is

that the species has a polarity with the center of negative charge generally residing on the atom having the higher electronegativity. The values for the polarizability and dipole moments of chemical species are found in the literature significantly [211,212].

The reduced collision diameter is a function of the individual diameters of the species and the relative charge. When a polar molecule interacts with a polar molecule (or non-polar with non-polar) [210]:

$$\sigma_{ij} = \frac{\sigma_i + \sigma_j}{2} \quad (194)$$

and when a non-polar molecule interacts with a polar molecule, the parameter ξ is again utilized as follows:

$$\sigma_{ij} = \xi^{-\frac{1}{6}} \left(\frac{\sigma_n + \sigma_p}{2} \right) \quad (195)$$

The collision integral involves an understanding of how the molecules interact. Following the Stockmayer extension of the Lennard-Jones potential model including attractive and repulsive forces, the collision between non-polar molecules can be estimated as [210]:

$$\Omega^{(1,1)} T_{ij}^* = 1.0548 \left(T_{ij}^* \right)^{-0.15504} + \left(T_{ij}^* + 0.55909 \right)^{-2.1705} \quad (196)$$

For polar molecules and non-polar and polar interactions, a look-up table for the collision integral is utilized [210].

At this stage, the model of diffusion purely consists of a binary mixture where D_{ij} is equal to D_{ji}. Since the exhaust of an internal combustion engine contains a large number of species in varying magnitude, this model of binary diffusion requires extension. Bird et al. wrote mixture-averaged diffusion constant as [213]:

$$\mathbf{D}_m = \frac{1 - Y_i}{\sum_{i \neq j}^{NM} X_i / D_{ij}} \quad (197)$$

using the mass and mole fractions of the respective species in order to calculate how one species will diffuse in a mixture of many different species. However, Kee et al. stated that this expression is not mathematically well defined in the limit of the mixture becoming a pure species [209]. While diffusion does not have any real meaning in the case of a singular species, numerically the model must ensure that the diffusion coefficients work properly in such a case. As a result, they write the mixture averaged diffusion constants as:

$$\mathbf{D}_m = \frac{\sum_{i \neq j}^{NM} X_i W_i}{W \sum_{i \neq j}^{NM} X_i / D_{ij}} \quad (198)$$

Kee et al. stated that the round off accumulates in nearly the same way between the numerator and denominator, with the quotient well behaved as the pure species limit is approached. While the formula is still undefined in the limit of a pure species, numerically the model is more stable when using this version.

To simplify the computation, Schettler et al. gave an empirical relation replacing the Lennard-Jones potential in finding the molecular diffusion coefficient [214]

$$\mathbf{D}_m = \frac{10^{-3} T^{1.75} \left(1/W_i + 1/W_j\right)^{1/2}}{p\left[\left(\sum_i V_{i1}\right)^{1/3} + \left(\sum_i V_{i2}\right)^{1/3}\right]^2} \quad (199)$$

using the molecular weight of the species with V_{i1} and V_{i2} describing the fraction of molecular volume of the species *1* and *2* respectively [210].

The next step in finding the effective diffusion coefficient is to understand the micro scale diffusion of the pores in the packed bed reactor. The average pore size within a packed bed governs the major contribution to diffusional resistance that moves the fluid toward and

away from the internal catalytic surface. Free-molecule Knudsen flow provides the major resistance to mass transfer if pore sizes are less than 50Å. This is because the mean free path of the gas is larger than the pore diameter and gas molecules collide with the catalyst pellets more frequently than they collide with other gas molecules. The regime is of importance in situations involving very small length scales and/or very low gas density (large mean free path). Under these circumstances, the product of the number of molecules entering the hole and the probability of a molecule that enters the pore passes through (e.g., not bouncing back out) determine the number of molecules passing through the small channel or pore. This is expressed through the calculation of Knudsen diffusion coefficient in a mixture in an array of straight cylindrical pores as given by [25,207,215]:

$$\mathbf{D}_K = \frac{d_p}{3}\sqrt{\frac{8R_uT}{\pi \mathbf{W}}} \quad (200)$$

For simplification, using a pore size expressed in Angstroms and temperature in K, the Knudsen diffusion coefficient in cm^2/s is [207]**:**

$$\mathbf{D}_K = \frac{1.05\times10^{-4} d_p}{2}\sqrt{\frac{T}{\mathbf{W}}} \quad (201)$$

In packed bed reactors, calculation of the Knudsen diffusion with good accuracy can be simplified as follows [198,216]:

$$\mathbf{D}_K = 97 r_e \sqrt{\frac{T}{\mathbf{W}}} \quad (202)$$

where, r_e is the equivalent pore radii determined from the porosity, pellet density (ρ_d) and BET surface area (S_g):

$r_e = \frac{2\varepsilon}{S_g \rho}$	(203)

This section presents the foundation of the effective diffusivity calculation for each species through determination of the fundamental mixture-averaged molecular diffusion and Knudsen diffusivities. The next section explains their incorporation into the packed bed reactor through a historical perspective.

4.5 EFFECTIVE DIFFUSIVITY

Aris in 1956 describes a lumped one-dimensional pseudo-homogeneous model for the species equation under axial mixing conditions [171]. This model superimposes a dispersion coefficient term that depends on the molecular diffusion coefficient and the advection of the flow in the radial direction:

$\mathbf{D}_I^{eff} = \mathbf{D}_m + \frac{u_s^2 R^2}{48\mathbf{D}_m}$	(204)

Aris applies the following condition in order to validate the use of one-dimensional flow in a packed bed:

$\frac{L}{R} > 0.16\left(\frac{u_s R}{\mathbf{D}_m}\right)$	(205)

with the above assumption stating that the tube radius must be small in comparison to a relatively long catalytic reactor length.

The simplest form for calculating the effective diffusivity from both the molecular and Knudsen diffusion coefficients was first accomplished by Evans and Watson in their Series Pore model [187]. This model is utilized due to the occurrence of molecular and Knudsen resistances

to the flow of the species through packed bed pores. The average porosity and tortuosity factor used in this model are based on the average pore radius and this model satisfies the fact that the diffusion flux ratio for binary mixtures is equal to the square root inverse of the molecular masses. As a result, the Series Pore model is expressed as:

$\frac{1}{\mathbf{D}^{eff}} = \left[\frac{1}{\mathbf{D}_m} + \frac{1}{\mathbf{D}_K}\right]\frac{\psi}{\varepsilon}$ (Series Pore model)	(206)

In 1962, Beek expresses the effective diffusion coefficient of the species where the flux of the one of gases is measured on the surface of the pellet [217]:

$\mathbf{D}^{eff} = \frac{L_e f}{\bar{\rho}_s}\left(\mathbf{X}_0 - \mathbf{X}_1\right)$	(207)

Here, the effective diffusion coefficient is given in terms of the difference between the mole fractions at the beginning and end of the reactor, diffusion length (L_e), a flux of the component that can be experimentally determined (f) and the molar density of the mixture.

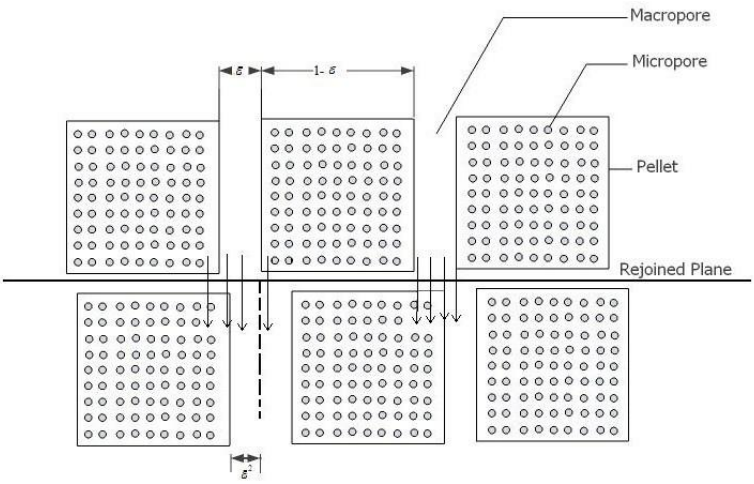

Figure 11: **Random pore model for a bidisperse porous solid [25].**

In the same year, Wakao and Smith, propose a Random pore model for calculating the diffusion coefficient in the catalyst layer for a bidisperse system [218]. They originally applied this model to pellets prepared via the compression of porous catalyst particles. Their model depends upon the pores within the pellets themselves (micro-pores) and spaces between the pellets (macro-pores), which in this paper is the bed porosity (ε) as illustrated in Figure 11. Both pores have a significant effect on the resulting diffusion calculation:

$$\mathbf{D}^{eff} = \varepsilon^2 \mathbf{D}_m + \left[\frac{\varepsilon_m^2 \left(1+3\varepsilon\right)}{1-\varepsilon} \right] \mathbf{D}_K \qquad \text{(Random Pore model)} \qquad (208)$$

with the diffusion coefficient for the macro-pores and micro-pores corresponding to the molecular and Knudsen diffusion coefficients respectively. They determine that this model works well for active catalysts in the micro-pores region because of the mutual contribution towards diffusion [185].

Three years later, Johnson and Stewart introduce a diffusion model that incorporates the radial influence of the pellet [186].

$$\mathbf{D}^{eff} = \frac{\varepsilon}{\psi} \int_0^{\infty} \left[\frac{\left(1-aX_i\right)}{\mathbf{D}_m} + \frac{1}{\mathbf{D}_K} \right]^{-1} \varepsilon\left(r\right) dr \qquad \text{(Cylindrical Pore model)} \qquad (209)$$

Where:

$$a = 1 - \left(W_i / W_j\right)^{1/2} \qquad (210)$$

This model integrates the radial variations of porosity with their corresponding molecular and Knudsen diffusion coefficients. They infer that the tortuosity factor depends upon the particle porosity and more reasonable values of tortuosity factors were obtained from the cylindrical pore model because the diffusion contribution is integrated over the entire range of pore size distribution as compared to an average pore radius used in the Series and Parallel Pore models.

Since the one-dimensional model derived by the author infers a constant porosity in order to minimize the amount of information required for model usage, this work does not explore the Cylindrical Pore model in the resulting parametric studies.

In a packed bed, it is important to understand that the fluid flow does not follow a straight path. Instead, it twists and turns its way through the pores and this tortuous flow requires modeling. This tortuosity is a methodology of accounting for the additional path length and the resulting increase in the capillary velocity over the interstitial axial velocity:

$$\tau = \frac{L_e}{L} \tag{211}$$

with the above equation being the standard definition for tortuosity (τ).

Jumping ahead slightly in the historical summary, with respect to incorporation in the governing equation of the chemical species, Eqn. (152), Epstein states that there is some confusion regarding whether tortuosity relates to either flow or diffusion [183]. He states that tortuosity is the ratio of the average pore length (L_e) to the length of the porous medium along the major flow axis (L), and a tortuosity factor (ψ) influences the diffusivity of a species in a medium. Hence, an effective diffusion of mixture-averaged species requires the use of a *tortuosity factor*:

$$\mathbf{D}_b = \frac{\mathbf{D}_m \varepsilon}{\psi} \tag{212}$$

which is the square of the *tortuosity*:

$$\psi = \tau^2 \tag{213}$$

For a randomly packed bed of pellets with pressure driven flow, researchers [219-222] elucidate that the tortuosity factor can range from one to seven with Carman experimentally determining a value of 2.5 for packed bed reactors.

It is important to mention that this factor is a strong function of the model. This is demonstrated by the fact that researchers calculate the effective Knudsen diffusivity using a separate tortuosity factor [181,182]:

$$\mathbf{D}_k = \frac{\mathbf{D}_K \varepsilon_s}{\psi_K} \tag{214}$$

with Ho and Strieder in 1980 describing the mixture-averaged and Knusden tortuosity factors, respectively, for the series pore model, explained later, as [223]:

$$\psi = 1 - \frac{1}{2}\ln\varepsilon \tag{215}$$

$$\psi_K = \frac{9}{8} - \frac{1}{2}\ln\varepsilon + \left(\frac{13}{8} - \frac{9}{8}\right)\varepsilon^{2/5} \tag{216}$$

Continuing an investigation into the effective diffusivity, Wakao and Kaguei [25] describe this value as:

$$\mathbf{D}^{eff} = (0.6 \sim 0.8)\mathbf{D}_b + 0.5 d_p u_s \tag{217}$$

with the second term added in order to account for turbulence when the flow velocity increases above a Reynolds number equal to five. From this point forward, the mixture averaged and Knudsen diffusivities will incorporate the tortuosity factors given their significance.

In 1991, Muller experimentally determines that the porosity of the packed bed can be computed as a function of the diameter of the reactor and the pellet diameter as follows [184]:

$$\varepsilon = 0.379 + \frac{0.078}{\left(D/d_b - 1.80\right)} \tag{218}$$

While not explicitly related to the effective diffusion, this finding makes it possible for the modeler to determine the porosity without requiring experimental tests.

In the same year, Sharma summarizes effective diffusion models available and revisits the Parallel Pore model of Wheeler from 1951 incorporating a tortuosity factor [185,224]**:**

$$\mathbf{D}^{eff} = \frac{\varepsilon \mathbf{D}_m}{\psi}\left[1 - e^{-(\mathbf{D}_K/\mathbf{D}_m)}\right] \quad \text{(Parallel Pore model)} \tag{219}$$

The author was unable to find a literature based fit of tortuosity factor as a function of porosity for the parallel pore model. As a result, using data from [225-228], the following fit was created:

$$\psi = 1 - 6.85 \ln \varepsilon \tag{220}$$

Note that while a model for the tortuosity factor as function of porosity is simplistic and may not capture all pertinent phenomena, it minimizes the need for additional calibration or models of surface effects.

In 2000, Winterberg et al. [7] describes the correlation for the axial mass dispersion coefficient for turbulent flow of the species:

$$\mathbf{D}_I^{eff} = \mathbf{D}^{eff} + \frac{\mathrm{Pe}}{K_{ax}}\mathbf{D}_b \tag{221}$$

where K_{ax} is a constant for the mass dispersion influence that they calculate with a value equal to two [229,230]. The effective diffusivity is provided in terms of bed porosity and they calculate the molecular diffusivity using a correlation given by Zehner and Schlunder [231]. They determine that the value of axial mass dispersion coefficient does not depend strongly on the type of species. Therefore, the species in the packed bed reactor will disperse at approximately the same rate with the Peclet number as:

$\mathrm{Pe} = \frac{u d_b}{\mathbf{D}_b}$	(222)

Similar to the studies of Evans and Watson [187], Belfiore states that it is necessary to add the resistances from Knudsen flow and ordinary molecular diffusion in order to calculate the net diffusivity in a porous pellet system when the average pore size is between 50 and 10^4 Å [207]. In the pore-size regime, where Knudsen and ordinary molecular diffusion are equally probable, they construct these resistances in series as they occur sequentially within the catalytic pore.

$\frac{1}{\mathbf{D}^{eff}} = \frac{1}{\mathbf{D}_k} + \frac{1-\beta X_i}{\mathbf{D}_b}$ (Series Pore model)	(223)

where, β represents the contribution from advective mass transfer:

$\beta = 1 + \alpha_i$	(224)

and:

$\alpha_i = \left(\frac{W_i}{W_{mix}} \right)^{1/2}$	(225)

The previous historical summary indicates that the mass transfer resistance is large when the advective mass transfer is negligible relative to diffusion at insignificant average species velocity and this condition prevails in porous catalytic pellets [207]. The average species velocity is the mole-fraction-weighted sum of species velocities in the reactor. Hence, advective mass transfer or $\beta = 0$ and this ultimately leads to the addition of the inverse diffusivities as provided by Evans and Watson [187]:

$\frac{1}{\mathbf{D}^{eff}} = \frac{1}{\mathbf{D}_k} + \frac{1}{\mathbf{D}_b}$	(226)

This is also suggested by Bosanquet from an empirical basis e.g., for transition region conditions, bulk diffusion and Knudsen diffusion act in series [232]. In the Series Pore model, it is also observed that the change in pressure does not influence the Knudsen diffusion but it does factor into the bulk diffusion coefficient. It is known that automotive catalytic converters operate at 1 bar pressure, and at this pressure their bulk diffusion coefficient does not show any sudden variations [198]. Furthermore, the bulk diffusion coefficient is relatively much higher than that of the Knudsen or pore diffusion coefficient.

In order to validate model predictions, measurement of the effective diffusivity in a porous solid can occur by utilizing the Wicke and Kallenbach cell method that is commonly used for measuring diffusivity over pellets [233]. This method determines the effective diffusion coefficient by measuring the diffusion rate (N) and incorporating it in the equation below [25,176]:

$$N = A\mathbf{D}^{eff}\frac{\Delta C}{L} \tag{227}$$

where ΔC is the difference in concentration across the catalyst length.

This section elucidates the Parallel, Series and Random Pore models used for the calculation of effective diffusion coefficient and their incorporation into the packed bed reactors [185-187,207,218]. It completes the historical findings of the diffusion coefficient parameter of the species equation which is used for the parametric studies and modeling purposes. In the next section, the chronological summary of the effective thermal conductivity parameter used in the energy equation is studied in detail by incorporating various modes of heat transfer.

4.6 EFFECTIVE THERMAL CONDUCTIVITY

Similar to the effective diffusivity discussion, this section describes a historical perspective of the effective thermal conductivity calculations present in the literature. This starts in 1955 with Plautz and Johnstone [234] proposed a correlation based on experiments that relate it to the molecular viscosity of the fluid, μ_{avg}, at the average bed temperature:

$\lambda^{eff} = 0.439 + 0.00129\left(d_b \varepsilon \rho_s c_p / \mu_{avg}\right)$	(228)

In 1960, Yagi et al. [189] were the first to measure its value in packed bed reactors. They determine that models should not neglect the effective axial thermal conductivity term in design calculations of adiabatic packed bed reactors because of relatively steep axial temperature gradients under low flow conditions. Their resulting formula is as follows:

$\lambda_I^{eff} = \lambda_0^{eff} + \delta \lambda_s \,\mathrm{Pr}\,\mathrm{Re}$	(229)

where, λ_I^{eff} is the axial effective thermal conductivity dependent upon the conduction of pellets as well as local fluid mixing [198]. The axial thermal conductivity effect reduces significantly with the decreases in size of the pellets. The effective thermal conductivity is a function of its value in a motionless fluid (λ_0^{eff}) and the molecular thermal conductivity of a moving fluid (λ_s) with the constant δ equal to 0.7 for metallic balls. The Reynolds number and Prandtl number for this equation are:

$\mathrm{Pr} = \dfrac{c_p \mu}{\lambda_s}$	(230)
$\mathrm{Re} = \dfrac{d_b \rho_s u_s}{\mu}$	(231)

In the following year, Gorring and Churchill [199] propose an empirical correlation to find the static contribution towards the effective thermal conductivity. They determine that the

static thermal conductivity is only a function of conduction as compared to convection and radiation:

$$\lambda_0^{eff} = 1.92\left(\frac{\lambda^2/\lambda_s}{C^2}\right)^{1/3} \quad (232)$$

Their efforts state that there is not a significant loss of accuracy when expressing the static value in terms of solid and fluid conductivities with porosity in the denominator:

$$C = \frac{1}{5/3 - \left(20\varepsilon^{1.5}/\pi\right)} \quad (233)$$

In the early 1960s for the parallel and series models, Yagi et al., Kunii and Smith [189,235] propose that the static thermal conductivity model includes all modes of heat transfer in the packed bed including radiation. They assume that a stagnant fluid film surrounds the particles and heat transfer occurs through the stationary fluid in the void spaces of the packed bed and in the solid phase. They use this reasoning to derive the effective thermal conductivity while continuing the reasoning of Gorring and Churchill with respect to neglecting radiation effects:

$$\frac{\lambda_0^{eff}}{\lambda_s} = \varepsilon + \left(1-\varepsilon\right)\left(\frac{\beta}{\delta + \frac{2\lambda_s}{3\lambda}}\right) \quad (234)$$

In this equation, β is the ratio of the effective distance between particles to the particle diameter, which is equal to one for loose packing, 0.895 for close packing and an average of 0.95 for an intermediate packing. The variable δ is the stagnant fluid thickness and they provide it graphically in terms of loose and dense packing with respect to the ratio of solid and fluid conductivities.

In 1966, Krupiczka [180] includes an empirical formula for finding the effective static thermal conductivity of granular materials with a porosity ranging between 0.215 and 0.476:

$$\lambda_0^{eff} = \lambda_s \left(\frac{\lambda}{\lambda_s} \right)^{0.28 - 0.751\log(\varepsilon) - 0.057\log(\lambda/\lambda_s)} \quad (235)$$

This static thermal conductivity coefficient is determined using derivations consisting of relatively long cylinders and spheres with two different porosities. This is simplified down into the influence of a single value of porosity as given.

At the turn of the decade, Zehner and Schlunder [231] present a model based on one-dimensional conductive heat flow through a packed bed of spherical particles. They assume a point contact of particles in the direction of heat flow e.g., the heat conduction through pellets over large surface contact area is not considered:

$$\lambda^{eff} = \lambda_s \left\{ 1 - (1-\varepsilon)^{1/2} + \frac{2(1-\varepsilon)^{1/2}}{1-BK} \cdot \left[\frac{(1-K)B}{(1-BK)^2} \ln\left(\frac{1}{BK} \right) - \left(\frac{B+1}{2} \right) - \left(\frac{B-1}{1-BK} \right) \right] \right\} \quad (236)$$

Where:

$$K = \frac{\lambda_s}{\lambda} \quad (237)$$

$$B = 1.364 \left(\frac{1-\varepsilon}{\varepsilon} \right)^{1.055} \quad (238)$$

with the value of *B* more accurately predicted by Hsu et al. [236] as given in Eqn. (238).

A few years later, Eigenberger [176] investigates the heat conduction phenomenon in a packed bed and demonstrates that the energy equation of their model in the solid phase requires a conduction term due to the high amount heat exchange through conduction to adjacent pellets when compared to convection and radiation terms. This work clarifies that the heat transfer to adjacent pellets occurs through pure conduction and when fluid velocity is high, heat transfer is a

function of the fluid vortices in the interstitial spaces between pellets and convection becomes important as shown in Figure 12.

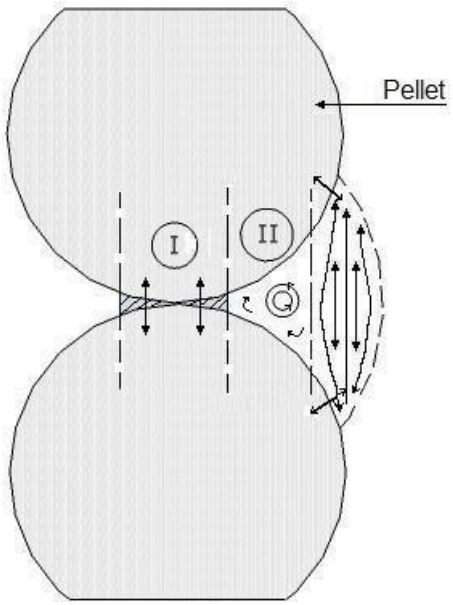

Figure 12: **Heat exchange between adjacent pellets: I. Exchange by pure conduction, II. Exchange by fluid vortices in the larger interstices [176].**

In 1974, Vortmeyer and Schaefer [190] derive the single phase pseudo-homogeneous energy equation from the two-dimensional heat equation under the assumption that the interphase heat transfer time is much smaller than the time for advection. In this model, they write energy equation in terms of an effective axial thermal conductivity:

$$\frac{\lambda_I^{eff}}{\lambda_s} = \frac{\lambda_0^{eff}}{\lambda_s} + \frac{\mathrm{Re}^2\,\mathrm{Pr}^2}{6(1-\varepsilon)\,\mathrm{Nu}} \qquad (239)$$

This equation is in correlation with the Yagi et al.'s relationship given in Eqn. (229). By modifying the last term in Eqn. (229) into a dimensionless parameter, this makes the equation

more versatile for different materials that can be used in the packed bed reactor. In this case, the Nusselt number is given by:

$$\mathrm{Nu} = \frac{h_\infty d_b}{\lambda_s} \tag{240}$$

with the effective static contribution of the thermal conductivity obtained from Eqn. (235).

In 1979, Dixon and Cresswell [191] provide a detailed discussion in predicting the effective axial thermal conductivity for a pseudo-homogeneous model and suggest a two-phase continuum model and single phase lumped model including both radial and axial conductivities. They suggest a detailed expression for the effective axial conductivity as follows:

$$\lambda_I^{eff} = \lambda_{as} + \frac{\lambda_a}{\left[1 + \frac{\frac{16\lambda_a}{3}\left(\frac{1}{hd_b} + \frac{0.1}{\lambda}\right)}{(1-\varepsilon)\left(D/d_b\right)^2}\right]^2} \tag{241}$$

They state that axial conductivity depends not only on the conductivities of the two phases but also on the fluid to solid heat transfer coefficient, the particle diameter and reactor tube to particle diameter ratio. In the above relationship, the axial solid conductivity (λ_a) and axial fluid conductivity (λ_{as}) are:

$$\lambda_a = \frac{2\lambda_s(1-\varepsilon)^{0.5}}{\left(1-\frac{\lambda_s B}{\lambda}\right)}\left[\frac{\left(1-\frac{\lambda_s}{\lambda}\right)B}{\left(1-\frac{\lambda_s B}{\lambda}\right)^2}\ln\left(\frac{\lambda}{B\lambda_s}\right) - \frac{B+1}{2} - \frac{B-1}{1-\frac{\lambda_s B}{\lambda}}\right] \tag{242}$$

$$\lambda_{as} = \frac{\mathrm{Pe}}{u_s \rho_s d_b c_p} \tag{243}$$

with the Peclet number expressed as:

$$\mathrm{Pe} = \frac{\mathrm{Re}\,\mathrm{Pr}}{0.73\varepsilon} + \frac{\left(1+\frac{9.7\varepsilon}{\mathrm{Re}\,\mathrm{Pr}}\right)}{0.5} \simeq 2 \tag{244}$$

and

$$B = C\left(\frac{1-\varepsilon}{\varepsilon}\right)^{10/9} \quad (245)$$

Where, C equals 1.25 for spheres and they use a Peclet number of approximately two in calculating axial fluid conductivity with h equal the fluid to/from solid heat transfer coefficient.

The following year, Kulkarni and Doraiswamy present a detailed review on the estimation of the transport properties in packed bed reactors [237]. They state that the effective thermal conductivity has a definite value when there is no flow and it rises sharply when flow begins. Therefore, there are two distinct contributors to the effective thermal conductivity in a packed bed catalytic reactor, namely static and dynamic. Static contributes to the thermal conductivity when there is not any fluid motion; whereas, the dynamic contribution is a function of the heat exchange due to a moving fluid. They mention that the heat transfer coefficient at the wall does not require consideration in the pseudo-homogeneous model. Moreover, they give an expression for the overall heat transfer coefficient, U, as:

$$\frac{UD}{\lambda_s}\exp\left(6\,d_b/D\right) = 1.26\,\mathrm{Re}^{0.95} \quad (246)$$

when the Reynolds number is between 20 and 7600 and d_b/D is between values of 0.05 and 0.3.

In 1988, Opris and Johnson [238] describe an effective thermal conductivity for fluid flow through porous media such as a diesel particulate traps:

$$\lambda^{eff} = \lambda_s\left[1+\frac{3(1-\varepsilon)\left(\frac{\lambda}{\lambda_s}-1\right)}{3+\varepsilon\left(\frac{\lambda}{\lambda_s}-1\right)}\right] \quad (247)$$

While this model is not expressly utilized for a packed bed reactor, it is important to illustrate the effective diffusion coefficient dependency on the average porosity and fluid thermal conductivity.

In 2000, Winterberg et al. provide an expression for the effective axial thermal conductivity neglecting variation in bed porosity, radial thermal conductivity and radial mass dispersion [7]:

$$\lambda_r^{eff} = \lambda_0^{eff} + \frac{\mathrm{Pe}}{K_{ax}}\lambda_s \tag{248}$$

with the Peclet number now calculated as:

$$\mathrm{Pe} = \frac{u_s d_b \rho_s c_s}{\lambda_s} \tag{249}$$

and K_{ax} described in the effective diffusivity section as equal to two [229]. This model incorporates a detailed description of porosity and flow distribution by utilizing the static thermal conductivity and Peclet number terms.

Two years later, Elsari and Hughes [239] calculate the axial thermal conductivity for a pseudo-homogeneous model under steady-state conditions without including radiation heat transfer. Based on their experimental results using alumina and chromite/alumina pellets, they provide an effective axial thermal conductivity calculation for alumina spheres equal to six millimeters in diameter:

$$\lambda_I^{eff} = \left(8.63 + 3.12\,\mathrm{Re}\right)\lambda_s \tag{250}$$

They deduce the axial thermal conductivity in this model from the correlation determined by Vortmeyer and Schaefer [190]. It depends only on the Reynolds number because they find that the Prandtl number is constant at low flow rates and factored into the constants. Furthermore, the axial thermal conductivity indicates a strong dependence on the particle size, and they determine that the coefficients in the equation decrease with a diminishing pellet diameter size.

Recently, Younis [179] suggests an effective thermal conductivity for the packed bed at high temperatures above 500K by including the influence of fluid conductivity and heat transfer through conduction and radiation as given below:

$$\lambda^{eff} = \left[\varepsilon\lambda_s + (1-\varepsilon)\left(\lambda + \frac{16\sigma T^3}{3\beta} \right) \right] \quad (251)$$

where, β is the extinction coefficient and σ is the Stefan-Boltzmann constant involving the effect of radiation by the pellets in addition to the solid conductivity as formulated by the Rosseland diffusion approximation [240].

At the same time, Nield and Bejan [193] provide a thorough investigation into the energy equation and give a clear understanding of the thermal conductivity term for a wide range of temperature conditions, shown here as calculated via Eqn. (174) :

$$\lambda^{eff} = \varepsilon\lambda_s + (1-\varepsilon)\lambda \quad (252)$$

They consider that the pellets are parallel to the fluid flow even though the flow is tortuous. Hence, they use the weighted arithmetic mean of the conductivities as evident through the derivation of the energy equation [9,241]. However, for practical purposes, a weighted geometric mean also provides a good estimation of the thermal conductivity:

$$\lambda^{eff} = \lambda_s^{\varepsilon}\lambda^{1-\varepsilon} \quad (253)$$

This section described a historical perspective of methods for determining the effective thermal conductivity for incorporation into the energy equation. At this point, this paper gives a clear understanding of the species and energy equations with varying treatments of the diffusivity and thermal conductivities evident in a packed bed reactor. The next section details a finite difference approximation of the species and energy equations in order to obtain a numerical solution. By using this model, the author will explore the different diffusivity and

thermal conductivity models in parametric studies in order to suggest appropriate models depending on flow parameters.

4.7 NUMERICAL MODELING

The proposed species and energy equations are in differential equation format, and their solution is obtained using an appropriate numerical method [198]. The utilization of various numerical methods depends upon the type of differential equations used and the desired accuracy. There are two broad categories for solving the governing equations:

i.) Initial Value Problems (IVP) allow for solution of the packed bed reactor with known inlet concentration conditions while calculating the concentration of the reactor downstream until the reactor exit is reached [242,243].

ii.) Boundary Value Problems (BVP) solves the one-dimensional dispersion model of the packed bed reactor. Here, the value of the dependent variable, such as concentration or temperature or its derivative, is required at two different values of the spacial values (length). Dividing the domain into a finite number of nodes or a grid allows for a numerical solution of the BVP. A number of different finite difference methods are available for solution of this problem during steady-state and transient conditions. In addition, it is understood that the finite difference method is simple when compared to orthogonal collocation or the weighted residuals method which involves more computation for the species and energy equations [243].

The resulting species and energy equations of the packed bed reactor have to be treated using the appropriate finite difference discretization technique in order to study the temperature and concentration variations in the converter.

The first step towards numerical modeling involves the treatment of the species equation given in Eqn. (152). This equation involves advection of fluid flow, effective diffusivity and catalytic reaction rates. The molar concentration of the species is independent of time and dependent on space for both the advection and diffusion terms. The steady-state chemical species equation is numerically modeled based upon the convection-diffusion parabolic partial differential equation [242,244] as shown below:

$$u_s \frac{\partial \bar{\mathbf{C}}}{\partial x} = \mathbf{D}^{eff} \frac{\partial^2 \bar{\mathbf{C}}}{\partial x^2} - G\bar{\mathbf{R}} \quad (254)$$

Where, G is a constant that is equal to G_{ca}/ε.

The above chemical species equation can be solved using a modified centered differentiation for the first-order derivative in order to provide an upwind interpretation for the advective flow and a second-order centered differentiation for the second-order derivatives as given below respectively [245]:

$$\frac{\partial \bar{\mathbf{C}}^n}{\partial x} \rightarrow \frac{\bar{\mathbf{C}}_i^n - \bar{\mathbf{C}}_{i-1}^n}{\Delta x} \quad (255)$$

$$\frac{\partial^2 \bar{\mathbf{C}}^n}{\partial x^2} \rightarrow \frac{\bar{\mathbf{C}}_{i+1}^n - 2\bar{\mathbf{C}}_i^n + \bar{\mathbf{C}}_{i-1}^n}{\Delta x^2} \quad (256)$$

Evaluation of the reaction rate $\bar{\mathbf{R}}$ occurs at each axial step and at each new time-step, the solution of the chemical species equation occurs implicitly until convergence. This eventually computes the molar concentration of each species at the outlet of the reactor as a function of temperature. Hence, using the above representations, the species equation becomes:

$$u_s \left(\frac{\bar{\mathbf{C}}_i^n - \bar{\mathbf{C}}_{i-1}^n}{\Delta x} \right) = \mathbf{D}^{eff} \left(\frac{\bar{\mathbf{C}}_{i+1}^n - 2\bar{\mathbf{C}}_i^n + \bar{\mathbf{C}}_{i-1}^n}{\Delta x^2} \right) - G\bar{\mathbf{R}} \quad (257)$$

where $\bar{\mathbf{C}}_i^n$ is implicitly computed until convergence at each axial node before moving onto the next axial step and the implicit computation is explained in detail in the next section.

The next step is the numerical treatment for the energy equation as represented in Eqn. (175). It is in the form of a convection-diffusion parabolic PDE that is a function of time and space. Since it is time dependent, it must satisfy an initial condition at time $t = 0$. Consequently, two boundary conditions are required because of the second-order space variable dependency and are provided later in this chapter. Hence, the energy equation is dependent on time (t) and space or catalyst bed length (x) as shown below:

$$\frac{\partial T}{\partial t} + Bu_s \frac{\partial T}{\partial x} = \frac{\lambda^{eff}}{A} \frac{\partial^2 T}{\partial x^2} + \frac{1}{A}\left(G_{ca} \sum_{j=1}^{NM} \bar{\mathbf{R}}\bar{\mathbf{h}} \right) + \frac{\dot{q}_{ext}}{A} \tag{258}$$

where the constants are described as:

$$A = \left[(1-\varepsilon)\rho c + \varepsilon \rho_s c_p \right] \tag{259}$$

$$B = \frac{\varepsilon \rho_s c_p}{(1-\varepsilon)\rho c + \varepsilon \rho_s c_p} \tag{260}$$

Solution of the convection-diffusion equation, as given in Eqn. (258), can occur numerically by various methods. The first is the Forward-Time Centered-Space (FTCS) method that is explicit, single-step, conditionally stable, and convergent having a second order accuracy [245]. This method provides relatively good accuracy for the convection-diffusion equation when compared to the Richardson Leapfrog method, Lax method, implicit Backward-Time Centered-Space method (BTCS) and first-order upwind method [13,242]. Other options include the McCormack with Predictor and Corrector method, Crank-Nicolson approximation and explicit Hopscotch method that provide good accuracy with unconditional stability for solving the convection-diffusion equations [242]. However, the amount of information required for

finding the properties of the base point (i.e., the inlet of the reactor) through adjacent grid points increases greatly and thus, the amount of computational time increases over the FTCS method.

The only drawback for the FTCS method is the increase in computational effort in order to achieve desired accuracy by reducing the length between the nodes (Δx). This is due to the fact that the time step has to be decreased four times the space (Δx) in order to maintain the stability for FTCS method as discussed in a later section [242]. The numerical discretization of the FTCS method follows for the energy equation:

$\frac{\partial T}{\partial t} \rightarrow \frac{T_i^{n+1} - T_i^n}{\Delta t}$	(261)
$\frac{\partial T}{\partial x} \rightarrow \frac{T_{i+1}^n - T_{i-1}^n}{2\Delta x}$	(262)
$\frac{\partial^2 T}{\partial x^2} \rightarrow \frac{T_{i+1}^n - 2T_i^n + T_{i-1}^n}{\Delta x^2}$	(263)

Subsequently, using the above representations of the FTCS method, the energy equation becomes:

$\left(\frac{T_i^{n+1} - T_i^n}{\Delta t}\right) + Bu_s\left(\frac{T_{i+1}^n - T_{i-1}^n}{2\Delta x}\right) = \frac{\lambda^{eff}}{A}\left(\frac{T_{i+1}^n - 2T_i^n + T_{i-1}^n}{\Delta x^2}\right) + \frac{1}{A}\left(G_{ca}\sum_{j=1}^{NM}\bar{\mathbf{R}}\bar{\mathbf{h}}\right) + \frac{\dot{q}_{ext}}{A}$	(264)

As discussed earlier, the temperature in the energy equation is time dependent over the reactor length and it is essential to determine the stability of the above equation by figuring out the condition for the time-step in order provide a bounded solution.

4.7.1 Stability Analysis

The FTCS finite difference energy equation given in Eqn. (264) includes a time-dependency term, and it is necessary to perform a stability analysis in order to determine a stable time-step. This is required to prevent the growth or amplification of resulting errors, thus avoiding an unbounded solution. This stability analysis can be accomplished using a Fourier or

Von Neumann method [242] . In this method, the exact solution of the equation is denoted by *D* and the numerical solution with finite accuracy is *N* and the difference between the solution (*N* - *D*) is said to be the round-off error denoted by *E*. This round-off error is obtained from the approximation of the numerical solution at each grid point and its repetitive operation on the remaining grid points that can increase the round-off error magnitude substantially [244]. As a result, the computed numerical solution must satisfy the finite difference equation to yield:

$$\left\{\begin{array}{l}\left(\dfrac{D_i^{n+1}+E_i^{n+1}-D_i^n-E_i^n}{\Delta t}\right)\\ +Bu_s\left(\dfrac{D_{i+1}^n+E_{i+1}^n-D_{i-1}^n-E_{i-1}^n}{2\Delta x}\right)\end{array}\right\}=\left\{\begin{array}{l}\dfrac{\lambda^{eff}}{A}\left\{\dfrac{D_{i+1}^n+E_{i+1}^n-2D_i^n-2E_i^n+D_{i-1}^n+E_{i-1}^n}{\Delta x^2}\right\}\\ +\dfrac{G_{ca}}{A}\sum_{j=1}^{NM}\bar{\mathbf{R}}\bar{\mathbf{h}}+\dfrac{\dot{q}_{ext}}{A}\end{array}\right\} \quad (265)$$

Simultaneously, the exact solution must satisfy:

$$\left(\frac{D_i^{n+1}-D_i^n}{\Delta t}\right)+Bu_s\left(\frac{D_{i+1}^n-D_{i-1}^n}{2\Delta x}\right)=\left\{\frac{\lambda^{eff}}{A}\left\{\frac{D_{i+1}^n-2D_i^n+D_{i-1}^n}{\Delta x^2}\right\}+\frac{G_{ca}}{A}\sum_{j=1}^{NM}\bar{\mathbf{R}}\bar{\mathbf{h}}+\frac{\dot{q}_{ext}}{A}\right\} \quad (266)$$

Calculation of the round-off error occurs by subtracting Eqn. (266) from Eqn. (265):

$$\left(\frac{E_i^{n+1}-E_i^n}{\Delta t}\right)+Bu_s\left(\frac{E_{i+1}^n-E_{i-1}^n}{2\Delta x}\right)=\frac{\lambda^{eff}}{A}\left\{\frac{E_{i+1}^n-2E_i^n+E_{i-1}^n}{\Delta x^2}\right\} \quad (267)$$

The round-off error and the exact numerical solution possess the same growth properties as a function of time and either of the above equations can be used to examine stability [244]. The subsequent error term is expressed using a Fourier series written in terms of time and spatial wave number as exponentials:

$$E_i^n=e^{at}e^{ik_m x} \quad (268)$$

Where, *a* is a constant and k_m denotes a wavelength number based on the catalyst length and the number of space increments. Substituting Eqn. (268) into Eqn. (267):

$$\left\{\begin{array}{l}\left(\dfrac{e^{a(t+\Delta t)}e^{ik_m x}-e^{at}e^{ik_m x}}{\Delta t}\right)\\ +Bu_s\left(\dfrac{e^{at}e^{ik_m(x+\Delta x)}-e^{at}e^{ik_m(x-\Delta x)}}{2\Delta x}\right)\end{array}\right\}=\frac{\lambda^{eff}}{A}\left\{\frac{e^{at}e^{ik_m(x+\Delta x)}-2e^{at}e^{ik_m x}+e^{at}e^{ik_m(x-\Delta x)}}{\Delta x^2}\right\} \quad (269)$$

and dividing both sides of the resultant equation by $e^{at}e^{ik_m x}$ results in:

$$\frac{e^{a(\Delta t)}-1}{\Delta t}+Bu_s\left(\frac{e^{ik_m\Delta x}-e^{-ik_m\Delta x}}{2\Delta x}\right)=\frac{\lambda^{eff}}{A}\left(\frac{e^{ik_m\Delta x}-2+e^{-ik_m\Delta x}}{\Delta x^2}\right) \quad (270)$$

Further modification gives,

$$e^{a\Delta t}=1+\frac{\mathbf{d}}{A}\left(e^{ik_m\Delta x}-2+e^{-ik_m\Delta x}\right)-\frac{B\mathbf{c}}{2}\left(e^{ik_m\Delta x}-e^{-ik_m\Delta x}\right) \quad (271)$$

where the diffusion and advection numbers are given as:

$$\mathbf{d}=\frac{\lambda^{eff}\Delta t}{\Delta x^2} \quad \text{(Diffusion number)} \quad (272)$$

$$\mathbf{c}=\frac{u_s\Delta t}{\Delta x} \quad \text{(Advection number)} \quad (273)$$

Using trigonometric properties,

$$e^{a\Delta t}=1+\frac{2\mathbf{d}}{A}\left[\cos\left(k_m\Delta x\right)-1\right]-B\mathbf{c}\left[i\sin\left(k_m\Delta x\right)\right] \quad (274)$$

and modifying the equation results in:

$$e^{a\Delta t}=\left(1-\frac{2\mathbf{d}}{A}\right)+\frac{2\mathbf{d}}{A}\left[\cos\left(k_m\Delta x\right)\right]-iB\mathbf{c}\sin\left(k_m\Delta x\right) \quad (275)$$

This resulting equation represents an ellipse in the complex plane with real (*2**d**/A*) and imaginary axes (*B**c*) respectively. In order to attain stability, the real and imaginary axes must be less than or equal to one because stability constrains the ellipse to be within or lie on the unit circle. Hence, the round-off error in the forward time-step should be equal or less than the error at the previous time-step *n*:

$$\left|e^{a\Delta t}\right| = \left|\left(1-\frac{2\mathbf{d}}{A}\right)+\frac{2\mathbf{d}}{A}\left[\cos\left(k_m\Delta x\right)\right]-iB\mathbf{c}\sin\left(k_m\Delta x\right)\right| \le 1 \quad (276)$$

Furthermore, the curvature of the ellipse obtained by the above equation should be greater than the curvature of the unit circle and this condition is satisfied as follows:

$$\left(B\mathbf{c}\right)^2 \le \frac{2\mathbf{d}}{A} \text{ and } \frac{2\mathbf{d}}{A} \le 1 \quad (277)$$

Therefore, the stability criteria for the FTCS approximation of the energy equation and the solution for the time-step can be determined as follows:

$$\Delta t \le \frac{2\lambda^{eff}}{AB^2u_s^2} \quad (278)$$

$$\Delta t \le \frac{A\Delta x^2}{2\lambda^{eff}} \Rightarrow \Delta t \le \frac{\Delta x^2\left[\left(1-\varepsilon\right)\rho c+\varepsilon\rho_s c_p\right]}{2\lambda^{eff}} \quad (279)$$

As a result, numerical computation of the solution illustrates that the above time-step conditions should be satisfied in order to provide a stable solution. Both time-step criteria are checked and the lower value of the two is utilized for modeling purposes. Solution of the finite difference energy equation utilizes the corresponding boundary and initial conditions as described in the next section.

4.7.2 Initial and Boundary Conditions

The first boundary condition for the species equation is the inlet condition as given below:

$$\bar{\mathbf{C}}\Big|_{i=0}^{n} = Specified \quad (280)$$

Since the finite discretization contains second-order derivatives, Neumann boundary conditions should be utilized at the outlet [242]:

$$\left.\frac{\partial \bar{\mathbf{C}}}{\partial x}\right|_{i=N} = 0 \tag{281}$$

In order to calculate the concentrations of the species at the n^{th} node (exit) and $n+1^{th}$ node, we use the Neumann boundary condition to provide the concentration at $n-1^{th}$ node is equal to the concentrations at n^{th} and $n+1^{th}$ node.

Since the governing equations are second-order in nature, the Equilibrium Method provides the discretization of this boundary condition [176,198,242]. Using this method for the last node of the chemical species equation results in:

$$\left.\frac{\partial \bar{\mathbf{C}}}{\partial x}\right|_{i=N} = \frac{\bar{\mathbf{C}}_{N+1} - \bar{\mathbf{C}}_{N-1}}{2\Delta x} = 0 \rightarrow \bar{\mathbf{C}}_{N+1} = \bar{\mathbf{C}}_{N-1} \tag{282}$$

Since *N+1* is expected when solving the last node according to the discretization of Eqn. (256), the model substitutes Eqn. (282) in order to complete the solution of the entire domain.

At the start of the simulation, the temperature at the first node of the packed bed rector is specified and the rest of the nodes are set equal to the ambient temperature (or the temperature of the first node). Hence, the initial condition for the energy equation becomes:

$$T\big|_{i=1}^{n} = Specified \tag{283}$$

The second boundary condition for the last node of the reactor uses the assumption that the packed bed reactor is being modeled in an adiabatic manner [14,198,246]:

$$\left.\frac{\partial T}{\partial x}\right|_{i=N} = 0 \tag{284}$$

Similar to the species equation, the Equilibrium Method is utilized for the discretization of this boundary condition before substitution into the governing equation for energy. Therefore, the numerical treatment for the pseudo-homogeneous species and energy equations with

corresponding initial and boundary conditions are performed considering appropriate limitations as discussed in the previous sections.

In order to model chemical reactions within the packed bed, it is required to apply a reaction rate expression to the species and energy equations. In this case, the reduction reaction of nitric oxide (NO) by carbon monoxide (CO) over rhodium/ alumina catalysts is employed in order to study light-off characteristics of this interaction in a packed bed reactor. The reason for using this reaction is to make the initial modeling efforts less convoluted by considering only two species (NO and CO). Moreover, as the previous chapters elucidate, this reaction has been extensively studied for utilization in modeling aftertreatment devices [32]. As a result, the next section will simulate the above reduction reaction over rhodium under packed bed reactor conditions. The modeling will occur via a global reaction equation as in Eqn. (77) and eliminates the usage of detailed reaction kinetics in order to reduce the number of parameters that require calibration for each step and thus, lessen the difficulty of modeling the chemical kinetics.

4.7.3 Modeling Data

The data utilized in simulating a packed bed reactor, of length 3 mm, comes from results by Granger et al. as presented in Table 2 [247-250]. In the simulation, the values of specific heat and enthalpy of each species were calculated using thermodynamic data and the Chemkin curve-fit equations [251] with the detailed equations provided in APPENDIX A.

Table 2: Packed bed reactor properties and reactant properties [247-250].

Parameter	**Variable**	**Value**	**Units**
Diameter of the packed bed reactor	*D*	0.012	m
Length of packed reactor bed	*L*	0.06	m

Length of packed bed	Lcb	0.003	m
Pellet diameter	d_b	0.00008	m
Pore diameter of pellets	d_p	1.7×10^{-9}	m
Space velocity	SV	93000	hr^{-1}
Velocity of the reactants at the inlet of the reactor (calculated from space velocity)	u_s	1.55	m/s
Density of the pellets	ρ	1000	kg/m^3
Specific heat capacity of pellets	c	813.25	J/kg/K
Geometric surface area per unit volume	G_{ca}	1	m^2/m^3
Thermal conductivity of pellets	λ	0.22	W/m/K
Thermal conductivity of the working fluid	λ_s	0.14884	W/m/K

The tortuosity factor for the model is initially calculated from the Series Pore expression of Eqn. (215), and the porosity of the packed bed reactor is calculated from Muller's expression as given in Eqn. (218). Based on the above geometric data and reactants' thermodynamic properties, the criteria for one-dimensional modeling are met through the mass and heat Biot numbers respectively. The methodology for solving mass, wall heat and pellet heat Biot numbers are provided in the previous sections in detail. In specific, the wall heat Biot number treats external heat transfer and the radial gradient of the reactor, and pellet heat Biot number checks the radial gradient of the pellets.

Table 3 and Table 4 list the mass and heat Biot numbers calculated for the diffusion and thermal conductivity models considered in the study. The mass Biot number for each species demonstrate values less than ten, satisfying the condition for neglecting diffusion in the radial

direction [27,197]. The wall and pellet heat Biot numbers for the conductivity models studied are less than one and 0.1 respectively [27,170]. This satisfies the conditions for neglecting radial temperature gradient change in the reactor and external heat transfer while justifying the use of the lumped model for the energy equation [205].

Table 3: Mass Biot number for packed bed reactor modeled

Species	Mass Biot Number		
	Series Pore model [187]	**Parallel Pore model** [185,224]	**Random Pore model** [218]
NO	2.273	8.093	0.877
CO	2.249	8.006	0.885
CO_2	0	0	0.934
N_2	0	0	0.984
He	3.874	9.850	0.482

Table 4: Heat Biot number for packed bed reactor modeled

Model	Wall heat Biot Number	Pellet heat Biot Number
Parallel flow Model [193]	0.255	0.003
Zehner and Schlunder Model [231]	0.259	0.003
Younis Model [179]	0.255	0.003
Weighted G.M Model [9,241]	0.302	0.004
Opris and Johnson Model [238]	0.258	0.003

Furthermore, the axial dispersion effect in the energy equation can be neglected when the calculated Reynolds number of the packed bed reactor is greater than twenty [252]. In this case, the reactor Reynolds number is about 144. Thus, the Biot number limitations for the one-dimensional analysis, stability conditions for the energy equation and inlet conditions for the packed bed reactor can be modeled in MATLAB based on the above the geometric and transport data with the detailed MATLAB programming of the reactor provided in APPENDIX B.

The final modeling task is to calibrate the chemical kinetic parameters for NO reduction by CO over the rhodium/alumina catalysts and incorporate these values into the species and energy equations. The amount of rhodium used in the catalyst bed is 0.023 gm with 94% dispersion over the alumina substrate. The inlet partial pressures of the reactants are maintained at 0.005 atm ($p_{CO} = p_{NO} = 0.005$ atm) with helium acting as an inert gas [248]. The reactor is operated at a nominal pressure of 1 atm and the inlet temperature of the catalyst bed is increased by 2K/min from 423K until it reaches 573K.

At these partial pressures, the observed apparent activation energy for the rate-determining step under adsorption equilibrium is found to be 196,648 J/mol [248]and this value is relatively higher when compared to the corresponding apparent activation energy of rhodium crystals; Rh(111). This is due to the high dispersion of rhodium molecules over alumina substrate [61,248]. The above values of apparent activation energy and the amount of rhodium catalyst are effectively utilized in the estimation of the pre-exponential factors of the reaction rate expressions given in Table 5**.**

In order to improve the modeling efforts, values of the pre-exponential factors and adsorption enthalpies in the Arrhenius and equilibrium constants expressions,

$k_{NO} = A_{NO} \exp\left(-\frac{E_a}{R_u T}\right)$	(285)
$K_{NO} = f_{NO} \exp\left(-\frac{\Delta H_{NO}}{R_u T}\right)$	(286)
$K_{CO} = f_{CO} \exp\left(-\frac{\Delta H_{CO}}{R_u T}\right)$	(287)

are not calibrated in accordance with the experimental data given.

In particular, the adsorption enthalpies for carbon monoxide (CO) and nitric oxide (NO) are determined based on the influence of the partial pressures of the reactants over rhodium catalysts using the correlations provided by Granger et al. [249]:

$\Delta H_{NO} = -34.8 + 1.9 \ln p_{CO} + 0.7 \ln p_{NO}$	(288)
$\Delta H_{CO} = -10.3 + 2.3 \ln p_{CO} + 1.9 \ln p_{NO}$	(289)

The above semi-empirical equations for adsorption enthalpies of NO and CO are obtained respectively based on the coverage factor of the reactants along with experimental evidence. The rest of the values needed for reaction rate utilization are provided in Table 5.

Each species equation incorporates a corresponding reaction rate as a source term calculated based on the global rate reaction step as given in Eqn. (77). The concentration of each species attains steady-state at each axial node for the respective time step by using the embedded ODE15s MATLAB solver [253]. Since the reaction rate expression used in the source term of the species and energy equations is relatively numerically sensitive with respect to temperature and pressure; it is necessary to use the ODE15s solver that is of fifth-order accuracy. It solves stiff ordinary differential equations as given in Eqn. (257) by computing the concentrations of each species at relatively small time steps while attaining steady-state based on previous time step values. Similarly, the concentrations of other axial nodes are determined using the above

ODE15s solver and a while loop condition. Finally, the concentrations at each axial node are simultaneously calculated by using another while loop that provides accurate steady-state concentrations based on the previous values.

Table 5: NO-CO reaction kinetic parameters [248].

Parameter	**Variable**	**Value**	**Units**
Apparent activation energy	E_a	196.648	kJ/mol
Pre-exponential factor	A_{NO}	0.32×10^{21}	mol/m^2s
Adsorption enthalpy of NO	ΔH_{NO}	-48.576	kJ/mol
Adsorption enthalpy of CO	ΔH_{CO}	-32.554	kJ/mol
Proportionality constant of NO adsorption	f_{NO}	2.4×10^{-2}	atm^{-1}
Proportionality constant of CO adsorption	f_{CO}	1.4×10^{-2}	atm^{-1}

The above modeling efforts were carried out using Intel Xeon E3110 Processor at 3 GHz clock speed and 8 GB RAM. MATLAB R2008a is used for the numerical modeling of the packed bed reactor and the operating system in which MATLAB operates is Windows Vista 64-bit.

4.8 RESULTS AND PARAMETRIC STUDIES

This section presents the conversion profiles of NO and CO and their light-off characteristics over rhodium catalysts along a catalyst bed in a temperature range of 423K to 573K. These conversion profiles are compared to the experimental values of Granger et al. [249,250] in order to study the accuracy of the species and energy equations derived in the

previous sections. The predicted conversion profiles of NO and CO species is found to be of a good fit when comparing with the experimental results in Figure 13 as in the simulated light-off temperature (533.5K) is close to the experimental light-off temperature (535K).

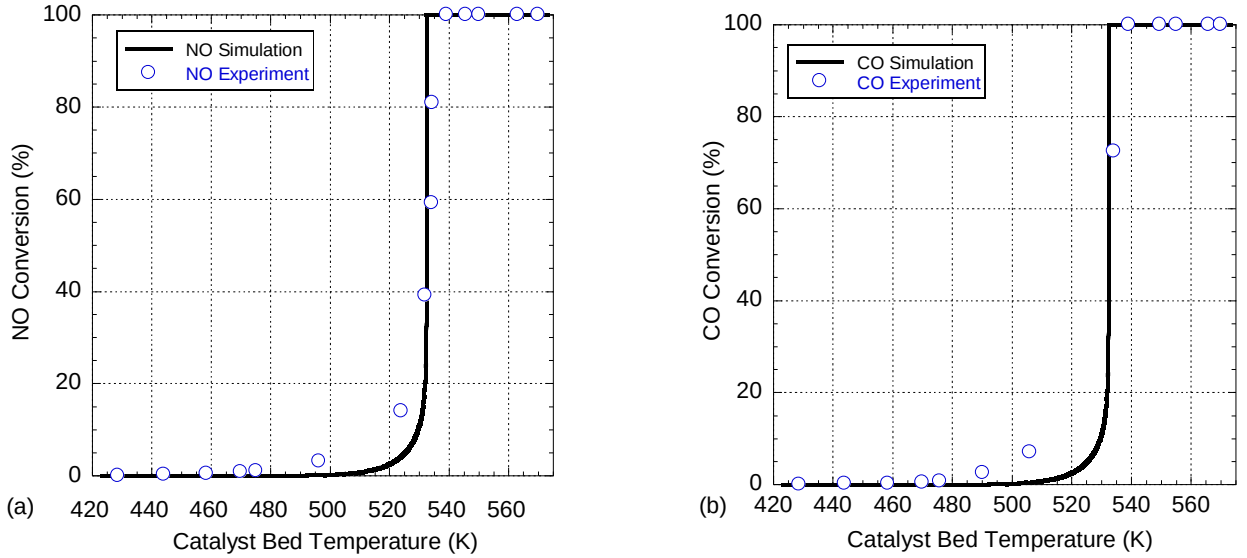

Figure 13: Comparison between experimental and simulated (a) NO and (b) CO conversion curves vs. temperature over rhodium/alumina catalysts [Series Pore Diffusion Model and Parallel Flow Conductivity Model with discretization equal to six]

To recap, for these simulations, the species equation uses the Series Pore Effective Diffusion model and the energy equation uses the Parallel Flow Effective Thermal Conductivity model with the global reaction rate expression as given in Eqn. (77). The NO light-off temperature is found to be 533.5K which is quite close to the experimental NO light-off temperature of 535K [250]. Since NO and CO are at stoichiometric inlet conditions and have equimolar conversion rate, the light-off temperature of CO is equal to that of NO. Thus, this model can be used for wide range of operating temperatures ranging from 300K to 800K and low (10 torr) to moderate pressures.

The discretization of the catalyst bed is based on the stability conditions presented in Eqns. (278) and (279). Since an increase in discretization (number of nodes) decreases the space

over which the equations are calculated, in order to maintain stability for the FTCS method, the time step has to decrease four times as much [242]. Based on the current geometric conditions, the maximum number of discretizations possible is proportional to the inlet temperature rise of the reactor and its corresponding time step. In the current modeling effort, the maximum number of discretizations considered is nine and this is due to considerable reduction in the computational time with good accuracy. The stability conditions for calculating the time step are highly sensitive towards the length of the catalyst bed and effective thermal conductivity. In this case, the length of the catalyst bed is small (3 mm), and so, the time step and the corresponding temperature rise for modeling the catalyst bed reduces significantly for a FTCS system and the value of time step reaches up to 0.27 second for the above conditions. Therefore, the temperature rise value used for the modeling, i.e., 0.00833 K rise in temperature of the reactor for every 0.25 second, should be less than the experimental temperature rise of 2 K/min and the corresponding time step is calculated based on stability conditions to avoid unbounded solutions. If the time step from the stability condition is further reduced by increasing the discretizations the model dynamically adjusts the temperature rise value for calculating the conversion profiles. This adjustment in reducing the temperature step from 0.00833 K rise for every 0.25 second to 0.001667 K for every 0.05 second significantly increases the computational time due to the calculation of species at each time step with the increased number of nodes. This increases the computational time exponentially with negligible increase in the accuracy of the model when compared with the experimental data.

Increasing the spatial discretization of the bed increases computational time while influencing model accuracy. This effect is due to the increase in the number of nodes that are used to attain steady-state for the species equation. The mean computational time and standard

deviation after 15 cycles for different discretizations are listed in Table 6 with corresponding error percentage values for the light-off temperatures when compared to the experimental values. The results show than an increase in the number of discretizations beyond six raises the computational time with a negligible increase in accuracy. Therefore, the following parametric studies for the species and energy equations are modeled using a discretization equal to six.

Table 6: Effect of discretization on the computational time and accuracy of the light-off temperature

Number of Nodes	Computational Time (sec)	Standard Deviation	Percentage Error
5	378	2.912	0.85%
6	498	7.057	0.61%
7	644	7.124	0.514%
8	760	8.260	0.514%
9	930	8.922	0.514%

In addition to the computational time studies, sensitivity study on the reaction kinetics is essential to check the model's dependency on the chemical kinetics parameters. The activation energy for the reaction modeled is constant for the given partial pressures, but the pre-exponential factor in the Arrhenius equation is a cure-fit. It is understood that the activation energy and pre-exponential factor is sensitive towards the conversion curves and the activation energy depends on partial pressures of the reactants [254] [255]. Effect of varying the pre-exponential factor on conversion characteristics is illustrated in the Figure 14. It is inferred that the value of the pre-exponential factor used in the reaction rate expression is relatively sensitive with respect to the conversion characteristics when compared to the change in the enthalpy of formation (ΔH_i) and the proportionality constant (f_i) of the adsorption step used in the kinetic rate

expression. However, when the pre-exponential factor is reduced by more than 50% of its original cure-fit value, the conversion characteristics of the species completely changes with a maximum of 10% conversion of the reactant species over the experimental temperature range.

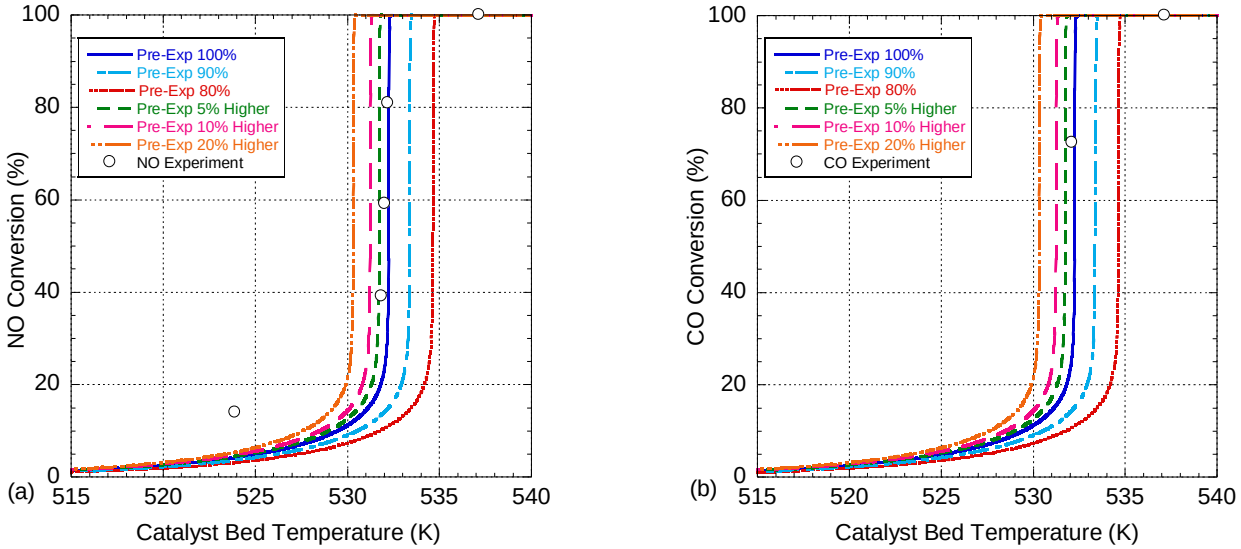

Figure 14: Comparison between experimental and simulated (a) NO and (b) CO conversion curves vs. temperature over rhodium/alumina catalysts for a range of Pre-exponential factors [Series Pore Diffusion Model and Parallel Flow Conductivity Model with discretization equal to six]

Now that the model accuracy and the kinetic rate parameter dependency has been verified, this work explores the dependency of the model on different diffusion and thermal conductivity models that can be used in a packed bed reactor simulation. This is accomplished in order to understand the influence and accuracy of different diffusion and thermal conductivity models on the species and energy equations of the packed bed reactor respectively.

The Series and Parallel Pore Diffusion models are constructed based on the molecular and Knudsen diffusivities acting in series and parallel respectively along the catalyst bed. In particular, the effective resistances on macro- and micro-pores of the pellets are considered when predicting the effective conversion of the species. Furthermore, the Random Pore model considers the detailed influence of micro- and macro-porosities of the pellets for the species

conversion. Based on the availability of experimental data and literature review of various diffusion models; it is important to understand the difference between the series pore model by Evans and Watson [187], the Parallel Pore model by Wheeler [185,224] and Random Pore model by Wakao and Smith [218]. Other models, such as the Cylindrical Pore and Axial Dispersion versions, are not considered. This is because the Cylindrical Pore model requires knowledge of the radial porosity of the catalyst bed, and the axial dispersion model is neglected due to the relatively high Reynolds number condition of the modeled experiment [243]. Thus, the effect of the three most widely used diffusion models, while keeping the thermal conductivity modeled in a parallel flow manner, is presented in Figure 15. These diffusion models are used when the flow is laminar and with negligible pressure drop.

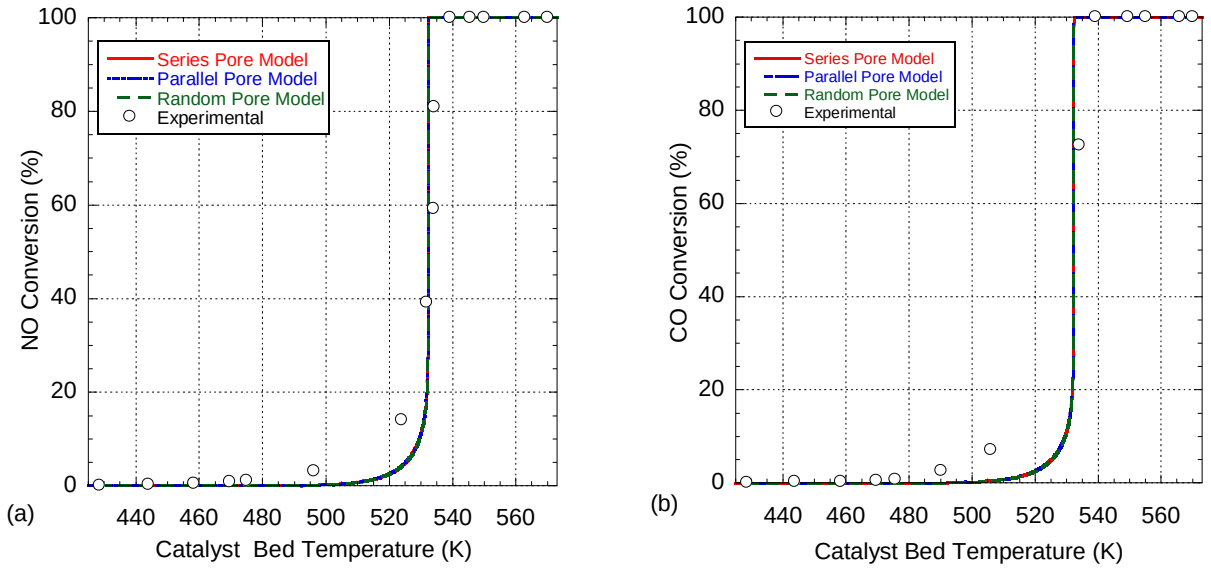

Figure 15: Comparison between experimental and simulated (a) NO and (b) CO conversion curves respectively, for Series, Parallel and Random Pore models vs. temperature over Rh/Al_2O_3 catalysts [Parallel Flow Conductivity model with discretization equal to six]

These figures demonstrate that the Parallel Pore (Eqn. (219)) and Random Pore (Eqn. (208)) models result in similar conversion profiles as that of the Series Pore model. This is

because all models end up calculating a similar effective diffusivity that has a minimal effect on the light-off characteristics when incorporated with porosity, concentrations and space velocity parameters of this particular experiment. The computational time for each diffusion model is presented in Table 7. The Random Pore model takes longer to run when compared to the other diffusion models because of the inclusion of micro-pore and macro-pore diffusion calculations at each node. As a result, since the Series Pore Diffusion model takes the least amount of time with minimum amount information needed to calculate the diffusion coefficients and has equivalent accuracy with respect to the NO-CO conversion profiles and the experimental data, this diffusion model is utilized to study the effect of different thermal conductivity models on the conversion curves.

Table 7: Comparison of computational time's average different diffusion models with the same effective thermal conductivity model (all models run using discretization value of six)

Diffusion Model	Computational Time (sec)	Standard Deviation	Percentage Error
Series Pore	644.00	6.124	0.514%
Parallel Pore	644.52	7.812	0.514%
Random Pore	649.20	6.473	0.514%

The axial effective thermal conductivity correlations suggested by Yagi et al. [189], Winterberg et al. [7], Elasri & Hughes [239], Dixon and Creswell [191] and Krupiczka [180] are neglected in the parametric studies due to the relatively high Reynolds number simulated [243] and insufficient experimental data corresponding to the calculation of the static thermal conductivity needed for these correlations. In addition, the influence of axial effective thermal conductivity decreases with a decrease in pellet particle size from 0.1 mm [239]. For the experiment modeled, pellet particle size is on the order of 10^{-5} m (powdered form) that should

result in a negligible impact of axial conductivity on the energy equation [239]. Thus, this work simulates the effective thermal conductivity models proposed by Zehner and Schlunder (Eqn. (236), Opris and Johnson (Eqn. (247), Younis (Eqn. (251), Tavman (Eqn. (253) and Nield and Bejan Eqn. (252). These correlations for a pseudo-homogeneous model provide an investigation into different forms of heat transfer such as conduction; convection and radiation involved between the pellets and reactor under appropriate heat Biot number considerations with temperature ranging from 350-800K. Moreover, these models incorporate fluid and pellet thermal conductivities and the porosity of the pellets.

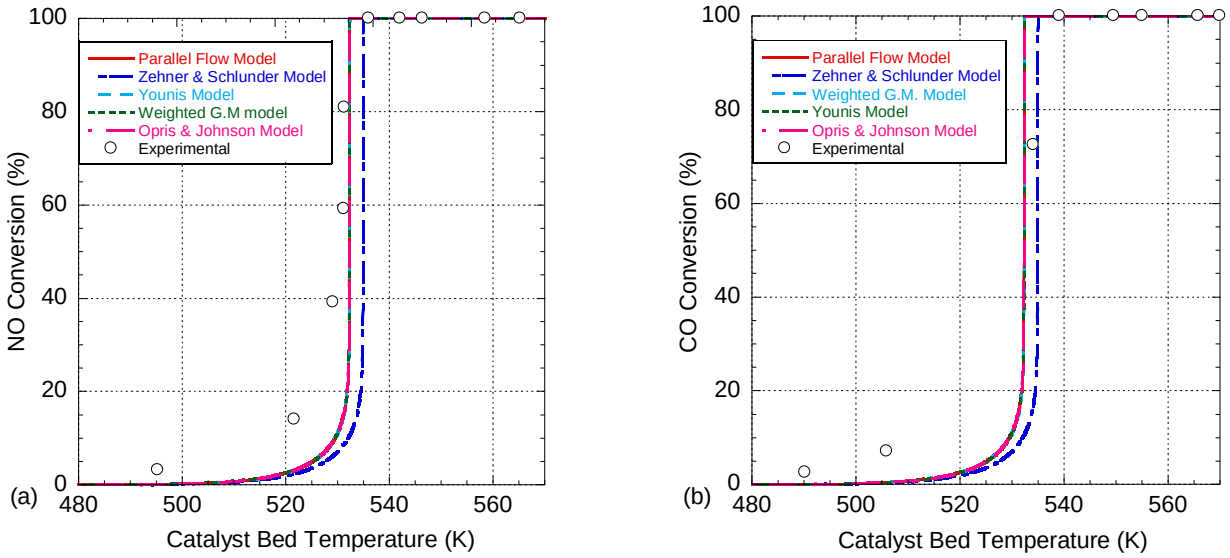

Figure 16: Comparison between experimental and simulated (a) NO and (b) CO conversion curves for Parallel, Zehner, Younis, Weighted G.M and Opris flow models vs. temperature over Rh/Al_2O_3 catalysts [Series Pore Diffusion model with discretization equal to six]

Figure 16 presents a comparison between the Opris and Johnson model, Younis model considering the effect of radiation between pellets, the Weighted Geometric Mean model, Parallel Flow model, and the Zehner and Schlunder model respectively in modeling the energy equation and species conversion characteristics. Similar to the various diffusion models, there is

negligible difference between the effective thermal conductivity models by the first three researchers and the Parallel Flow model on the conversion profiles and light-off temperatures. This is due to the calculation of a similar conductivity at the conditions employed in the reactor experiment. However, the Zehner and Schlunder model demonstrates slightly different light-off temperature characteristics due to their calculation of a higher thermal conductivity coefficient. Moreover, their correlation involves the calculation of the conductivity term using a point contact of the pellets in the direction of heat flow leading to a further deviation from the other researchers' models. Table 8 provides the values of the different effective thermal conductivities considering the influence of temperature. In the case of the Younis model, radiation of the pellets is calculated at each temperature and utilized in the temperature equation correspondingly. The rest of the models are calculated based on values of the thermal conductivity of fluid and pellets. The computational time for all models is around 640 seconds with a standard deviation of 7.145.

Table 8: Effective thermal conductivity values for different models and error percentage for NO with experimental light-off temperature

Thermal Conductivity Model	Effective Thermal Conductivity (W/m/K)	Percentage Error for NO
Parallel flow	0.1930	0.514%
Zehner and Schlunder	0.2199	0.018%
Younis model	0.2087	0.501%
Opris and Johnson	0.1930	0.514%
Weighted Geometric Mean	0.2081	0.504%

It is important to note that since the experiment occurred at a relatively moderate Space Velocity (SV) of 93,000 hr^{-1}, there is sufficient time for diffusion to occur through the pellets. This can be the reason why the different diffusion models all produced similar results. Whereas, the thermal conductivity models show small variations on their conversion profiles at this SV. This demonstrates a larger model dependency on velocity of the fluid and porosity of the medium. In order to study the effect of mass and heat transfer limitations on diffusion and thermal conductivity models, the simulations were repeated under high SV conditions.

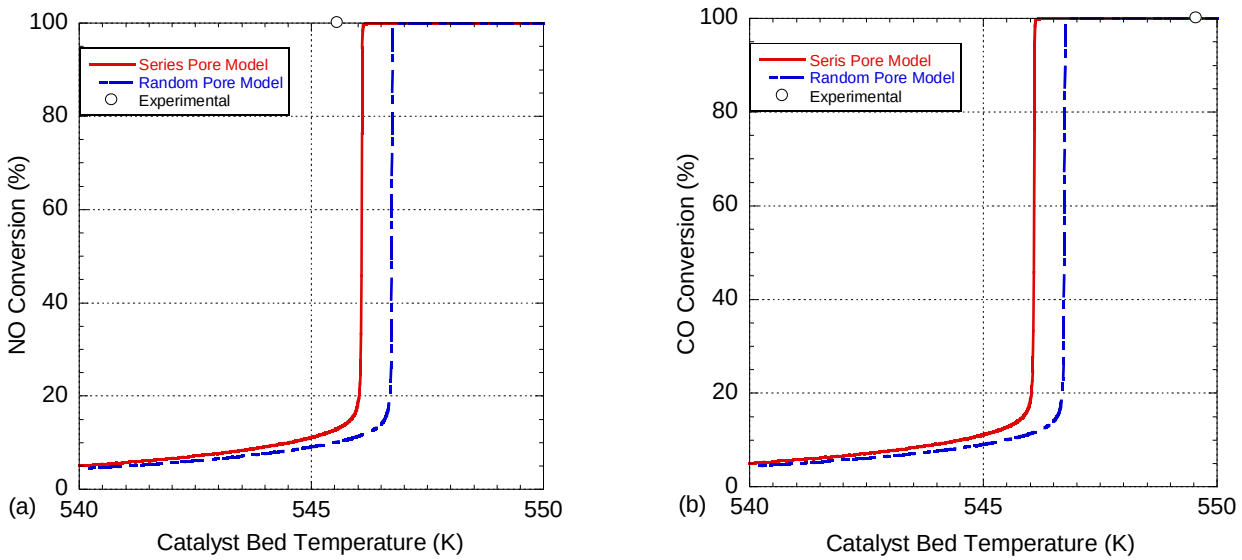

Figure 17: Comparison between experimental and simulated (a) NO and (b) CO conversion curves for various diffusion models versus temperature over Rh/Al_2O_3 catalyst at high SV conditions

Figure 17 presents the NO and CO conversion results respectively of the different diffusion models simulated under a high Space Velocity of 420,000 hr^{-1}. Both the Series and Random Pore models show a shift towards a higher light-off temperature because of the high species velocity through pellets resulting in a lower residence time for the reaction to take place. There is a offset in the light-off characteristics by the random pore model by 1 K due to a lower diffusion rate in the micro-pore region when compared to Series Pore model that considers the

summation of molecular and Knudsen diffusivities. Furthermore, the Parallel Pore model violates the mass Biot limitations at a SV greater than 125,000 hr^{-1}; hence, the latter model is not used for the mass transfer limitation studies.

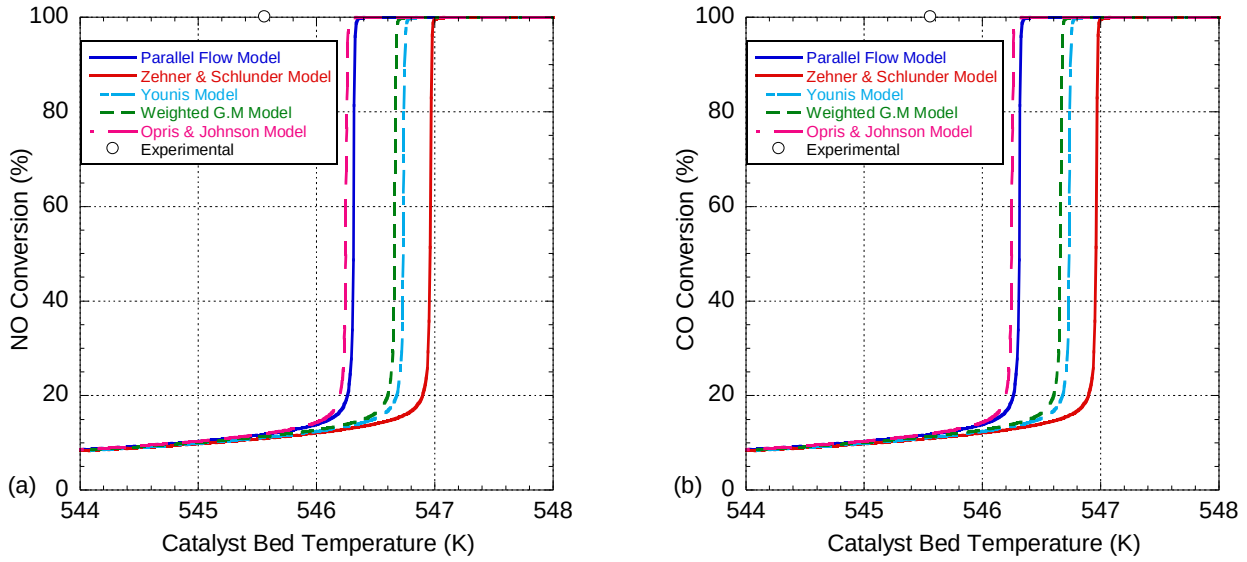

Figure 18: Comparison between experimental and simulated (a) NO and (b) CO conversion curves for various thermal conductivity models versus temperature over Rh/Al_2O_3 catalysts at high SV conditions

Similar to the diffusion models, thermal conductivity models are studied at a Space Velocity of 420,000 hr^{-1} as shown in Figure 18. The effective thermal conductivity predicted by all the models shows relatively small variations in their conversion profiles under appropriate heat Biot number limitations. Small variations in the light-off characteristics are due to the model dependence on the velocity of the species flowing through the reactor. Furthermore, the light-off temperature is increased by around 10 K when compared to the experimental values at this high Space Velocity due to the increase in the advective energy of the species travelling through the pellets.

As a result, based on an understanding of the literature, experimental data and parametric studies performed, the author suggests utilizing the Series Pore Diffusion model for effective

diffusivity. This is because it has equivalent accuracy as the other two models considered (Parallel and Random), runs slightly faster and does not violate the mass Biot limitation under high flow rate conditions.

Different thermal conductivity models are proposed in the literature, and one can investigate their differences based on the changes in particle size and porosities of the pellets. It has been found that no single model can explain the heat transfer phenomenon accurately for a wide range of catalyst materials and porosities [180,182,207,231,236,237,241]. In the case of a one-dimensional psuedo-homogeneous packed bed reactor model, the thermal conductivity models presented all provide a relatively good estimation of the thermal conductivity with the experimental findings and light-off temperature when compared to the experimental results. However, literature indicates that the Zehner and Schlunder model [231] typically provides a more accurate light-off temperature in comparison with experimental results while offering a better dependency on the porosity of the packed bed reactor [241]. The results in this work demonstrate an increased accuracy for CO conversion, but a decreased accuracy for NO conversion using this model. Therefore, further testing against experimental data of the models is needed that will be accomplished in the Chemical and Petroleum engineering laboratories at the University of Kansas.

4.9 CONCLUSION

A complete set of equations along with a detailed numerical scheme for one-dimensional modeling of a packed bed reactor has been presented following a comprehensive review of the literature, finite difference techniques and detailed reaction mechanisms. This work provides a full methodology in solving one-dimensional packed bed reactors to be used in estimating

conversion characteristics for a wide number of different chemical reactions. Furthermore, the history of detailed kinetic mechanisms of NO and CO reacting over rhodium and platinum catalysts are presented in order to provide global rate expressions for precisely predicting their light-off characteristics.

The results were obtained using a first principle basis of the species and energy equations by elaborating on all limiting conditions presented in the literature. The results illustrate that a careful consideration of source terms on species and energy equations with appropriate Biot number limitations are essential in modeling a packed bed reactor accurately. Moreover, the chapters are neatly summarized with criteria affecting one-dimensional modeling and parametric studies in order to provide the knowledge for researchers to build more complex packed bed models based upon this work. Parametric studies demonstrate that conversion characteristics do depend on the diffusion and thermal conductivity models; however, the specific choice of model does not largely influence the conversion profiles because of the similar effective transport values. Future work will employ this model in the simulation of NO oxidation over platinum catalysts in order to compare with experimental values measured in a packed bed reactor at the University of Kansas in the Department of Chemical and Petroleum Engineering.

APPENDICES

APPENDIX A: CHEMKIN DATA

In this appendix, various CHEMKIN thermodynamic data used in the modeling are provided. The thermodynamic data are stored as polynomial fits to find the constant pressure specific heat (c_p) and enthalpy (H_p) of the reactants [251].

$c_p = R_u \cdot \left(a_1 + a_2 \cdot T + a_3 \cdot T^2 + a_4 \cdot T^3 + a_5 \cdot T^4\right)$	(290)
$H_p = R_u \cdot \left(a_1 + \left(a_2 \cdot T^2\right)/2 + \left(a_3 \cdot T^3\right)/3 + \left(a_4 \cdot T^4\right)/4 + \left(a_5 \cdot T^5\right)/5 + a_6\right)$	(291)

The above correlations have coefficients numbered in front of the temperature terms and these coefficient values are based on the species used and the temperature range. In this case, the author used the coefficients ranging from 300 K to 1000 K of temperature for NO, CO, N_2, CO_2 and He species. The table below provides the list of polynomial coefficients for each species at temperature between 300 K and 1000 K.

Table 9: **Polynomial coefficients for the species in the packed bed reactor**

Species	**Polynomial coefficients for the specific heat and enthalpy**					
	a_1	**a_2**	**a_3**	**a_4**	**a_5**	**a_6**
NO	3.376541	0.0012530634	-3.302750×10^{-6}	5.217810×10^{-9}	$-2.446262 \times 10^{-12}$	9817.961
CO	3.262451	0.0015119409	-3.881755×10^{-6}	5.581944×10^{-9}	-2474951×10^{-12}	-14310.54
N_2	3.298677	0.0014082404	-3.963222×10^{-6}	5.641515×10^{-9}	$-2.444854 \times 10^{-12}$	-1020.89
CO_2	2.275724	0.009922072	-1.040911×10^{-5}	6.866686×10^{-9}	$-2.117280 \times 10^{-12}$	-48373.14
He	2.500000	0	0	0	0	-745.3750

APPENDIX B: MOLECULAR DIFFUSION COEFFICIENT

This section provides data for calculating molecular diffusion coefficient using the Chapman-Enskog diffusion equation [210]. The table below lists values of collision diameter and epsilon ratio for each species used in the modeling of NO-CO reaction over rhodium/alumina catalysts.

Table 10: Values of collision diameter and epsilon ratio for calculating molecular diffusion coefficients

Species	Collision Diameter (Å)	Epsilon ratio (K^{-1})
NO	3.492	116.7
CO	3.690	91.7
N_2	3.798	71.4
CO_2	3.941	195.2
He	2.551	10.22

APPENDIX C: MATLAB CODE FOR MODELING PACKED BED REACTOR

The MATLAB code presented in this section is to provide complete access to the modeling of the one-dimensional packed bed reactor and thus improve the modeling efforts accordingly.

C.1. Packed bed modeling for series pore diffusion and parallel flow thermal conductivity:

```
%%%%%%%%%%%%%%%%%%%%%%%%%%%%%%%%%%%%%%%%%%%%%%%%%%%%%%%%%%%%%%%%%%%%%%%%%%%%%%%
%%%%%  ONE DIMENSIONAL PACKED BED REACTOR MODELING FOR AFTERTREATMENT  %%%%
%%%%%%%%%%%%%%%%%     STUDIES IN LABORATORY SCALE    %%%%%%%%%%%%%%%%%%%%%%%%
%%%%%%    PROGRAM BY: ANAND SRINIVASAN, DR. CHRISTOPHER DEPCIK    %%%%%%%%%
%%%%%%%%%%%%%%%%%%%%%%%%%%%%%%%%%%%%%%%%%%%%%%%%%%%%%%%%%%%%%%%%%%%%%%%%%%%%%%%

%%%%%%%%%%%%%%%%%%%%%%%%%%%%%%%%%%%%%%%%%%%%%%%%%%%%%%%%%%%%%%%%%%%%%%%%%%%%%%%
%%%%% Modeling of Packed bed (or) Pellet type Catalytic Converter for %%%%%
%%%%% NO reduction reaction by CO over rhodium/alumina is performed  %%%%%%
%%%%%%%%%%%%%%%%%%%%%%%%%%%%%%%%%%%%%%%%%%%%%%%%%%%%%%%%%%%%%%%%%%%%%%%%%%%%%%%

%%%%%%%%%%%%%%%%%%%%%%%%%%%%%%%%%%%%%%%%%%%%%%%%%%%%%%%%%%%%%%%%%%%%%%%%%%%%%%%
% Finite Difference Method is used for modeling the species and energy
% equations. FTCS (Forward Time, Center Space method is used for the
% temperature modeling and Modified Central Difference method with forward
% upwind interpretation is used for species equation.
% Neumann Boundary Condition is used at the end of packed bed reactor
% with specified initial conditions for the species and energy equation.
%%%%%%%%%%%%%%%%%%%%%%%%%%%%%%%%%%%%%%%%%%%%%%%%%%%%%%%%%%%%%%%%%%%%%%%%%%%%%%%

%%%%%%%%%%%%%%%%%%%%%%%%%%%%%%%%%%%%%%%%%%%%%%%%%%%%%%%%%%%%%%%%%%%%%%%%%%%%%%%
%%%%% Pre-allocation of the variables are done to optimize the speed %%%%%%
%%%%%%%%%%%%%%%%%%%%%%%%%%%%%%%%%%%%%%%%%%%%%%%%%%%%%%%%%%%%%%%%%%%%%%%%%%%%%%%

%%%%%%%%%%%%%%%%%%%%%%%%%%%%%%%%%%%%%%%%%%%%%%%%%%%%%%%%%%%%%%%%%%%%%%%%%%%%%%%
% Parametric studies are made for various effective diffusivity and
% thermal conductivity models and, compared with the experimental values.
%%%%%%%%%%%%%%%%%%%%%%%%%%%%%%%%%%%%%%%%%%%%%%%%%%%%%%%%%%%%%%%%%%%%%%%%%%%%%%%

%%%%%%%%%%%%%%%%%%%%%%%%%%%%%%%%%%%%%%%%%%%%%%%%%%%%%%%%%%%%%%%%%%%%%%%%%%%%%%%
% Reaction Studied: CO + NO ----> (1/2) N2 + CO2
% from 423 K to 573 K at 2 degree K/min
%%%%%%%%%%%%%%%%%%%%%%%%%%%%%%%%%%%%%%%%%%%%%%%%%%%%%%%%%%%%%%%%%%%%%%%%%%%%%%%

% Assigning Numbers to Species
% 1:NO  - nitric oxide
% 2:CO - carbon monoxide
% 3:N2 - nitrogen
% 4:CO2 - carbon dioxide
% 5:He  - helium (Inert gas)

clc;            % Clear command window screen
```

```
clear all;      % Clear workspace data

tic             % Start Clock time

% Defining Global Variables
global E
global DiffMix
global Deff
global Tia
global i
global Ru
global Pres
global RR
global EffDia
global EffMol
global EffKBEp
global u
global L
global dx
global Concc
global h


%%%%%%%%%%%%%%%%%%%%%%%%   MODELING PARAMETERS      %%%%%%%%%%%%%%%%%%%%%%%%%%
%%%%%%%%%%%%%%%%%%%%%%%%%%%%%%%%%%%%%%%%%%%%%%%%%%%%%%%%%%%%%%%%%%%%%%%%%%%%%%%

% Universal Gas Constant (J/K/mol)
% Ref: From Fundamentals of Heat and Mass Transfer by Frank Incorporation
Ru=8.314;

% Defining values of coefficients from Chemkin thermodynamics data which
% needs to be incorporated for the calculation of CP and Enthalpy
% The values given below can be used when the temperatures are from 300 to
% 1000K for the respective species
a11=3.376541;              a12=0.0012530634;              a13=-0.000003302750;
a14=0.000000005217810; a15=-0.000000000002446262; a16=9817.961;
% Coefficients of NO
a21=3.262451;              a22=0.0015119409;              a23=-0.000003881755;
a24=0.000000005581944; a25=-0.000000000002474951; a26=-14310.539;
% Coefficients of CO
a31=3.298677;              a32=0.0014082404;              a33=-0.000003963222;
a34=0.000000005641515; a35=-0.000000000002444854; a36=-1020.8999;
% Coefficients of N2
a41=2.275724;             a42=0.009922072;                a43=-0.000010409113;
a44=0.000000006866686; a45=-0.000000000002117280; a46=-48373.14;
% Coefficients of CO2
a51=2.500000;             a52=0.000000000;                a53=0.0000000000000;
a54=0.0000000000000; a55=0.0000000000000; a56=-745.3750;
% Coefficients of He

% Ref: Granger et al.2001_TPDstudiesofNO-CORn_Topicsofcatalysis_V16-17_394.
% Granger et al.1998_KineticsofNO-CORnoverRh/Al2O3_J.Catal.V175_194-203
% Density of particle density (kg/m^3)
DenP = 1000;
```

```
% Thermal Conductivity of the pellets based on Prater Number (W/m/k)
Kp=0.22;
% Thermal Conductivity of the gas (NO+CO+He) at initial conditions (W/m/K)
Kg=0.14884;
% Constant Specific Heat for pellets at Constant Pressure (J/KgK)
Cpp = 813.25;
% Length of Pellet bed Reactor (m) -> (6 cm)
L=0.06;
% Length of Catalyst bed used for modeling (m) -> (3 mm)
Lcb = 0.003;
% Diameter of Packed bed reactor (m) -> (1.2 cm)
D=0.012;
% Space velocity (per hour)
SV = 93000;
% Diameter of the pellets (m)
db = 8*10^-5;
% Pore Diameter of the pellets (m)
dp = 1.7*10^-9;
% Pressure of the packed bed reactor (N/m^2) (or) 1 atm
Pres=101325;
% Geometric Surface area per unit volume (m^2/m^3)
Gca= 1;
% Inlet Velocity for packed bed calculated from space velocity (m/s)
u = (SV/3600)*L;
% Porosity of the packed bed reactor from Muller's Expression
E = 0.379 + (0.078/((D/db)-1.80));
% Since, we don't have data for the tortuous path. We can use Ho and
% Strider expression for finding out tortuosity factor
TorF = 1- (0.5*log(E));
% Since, we don't have data for the tortuous path. We can use Ho and
% Strieder expression for finding out Knusden tortuosity factor
KnTorF = (9/8)-(0.5*ln(E))+(((13/8)-(9/8))*((E)^0.4));
% Tortuosity of the flow in packed bed reactor
Tor = sqrt (TorF);
% dynamic viscosity of the fluid in (Kg/m.s)
DyVis= 2.1974*10^-5;

% Values for calculating molecular diffusivity
% Ref: Diffusion Mass Transfer in Fluid System by Cussler
% Collision diameter in angstroms
Dia(1)=3.492;               % Diameter of NO
Dia(2)=3.690;               % Diameter of CO
Dia(3)=3.798;               % Diameter of N2
Dia(4)=3.941;               % Diameter of CO2
Dia(5)=2.551;               % Diameter of He

% Ratio of Epsilon by kb in degree Kelvin
EpKB(1)=116.7;              % Epsilon by Kb for NO
EpKB(2)=91.7;               % Epsilon by Kb for CO
EpKB(3)=71.4;               % Epsilon by Kb for N2
EpKB(4)=195.2;              % Epsilon by Kb for CO2
EpKB(5)=10.22;              % Epsilon by Kb for He

% Molecular weight of the species
Mol(1)=30.0061;             % Molecular Weight of NO (Kg/Kmol)
```

```
Mol(2)=28.01;                % Molecular Weight of CO (Kg/Kmol)
Mol(3)=28.01348;             % Molecular Weight of N2 (Kg/kmol)
Mol(4)=44.0095;              % Molecular Weight of CO2 (Kg/Kmol)
Mol(5)=4.003;                % Molecular Weight of He (Kg/Kmol)
%%%%%%%%%%%%%%%%%%%%%%%%%%%%%%%%%%%%%%%%%%%%%%%%%%%%%%%%%%%%%%%%%%%%%%%%%%%%%%%


%%%%%%%%%%%%%%%%    DISCRETIZATION OF THE REACTOR    %%%%%%%%%%%%%%%%%%%%%%
%%%%%%%%%%%%%%%%%%%%%%%%%%%%%%%%%%%%%%%%%%%%%%%%%%%%%%%%%%%%%%%%%%%%%%%%%%%%%%%

disp('Welcome to 1-D Packed Bed Modeling for NO reduction reaction by CO over
rhodium/alumina catalysts');
disp('Length of the catalyst bed in 0.003 m');
h=input('Enter the Discretization number:');
while h > 10
    disp('For this modeling the length of the catalyst bed is 0.003 m and so,
please discritize accordingly to reduce computational time');
    h=input('Enter the Discretization number:');
    if isempty(h)
    h=input('Please enter the Discretization number less than 10:');
    end
end

% Discretization Length of the reactor (m)
dx = Lcb/(h-1);

%%%%%%%% INITIALIZE MOLE FRACTIONS AND TEMPERATURE OF THE REACTOR  %%%%%%%%
%%%%%%%%%%%%%%%%%%%%%%%%%%%%%%%%%%%%%%%%%%%%%%%%%%%%%%%%%%%%%%%%%%%%%%%%%%%%%%%

% Initial Mole fractions are equal to the initial partial pressures of
% NO and CO provided as the reactor operates at 1 atm pressure condition

% Partial Pressure of the reactants (atm)
P(1)=0.005;                  % Inlet NO partial pressure
P(2)=0.005;                  % Inlet CO partial pressure
P(3)=0;                      % Inlet N2 partial pressure
P(4)=0;                      % Inlet CO2 partial pressure
P(5)=0.99;                   % Inlet He partial pressure

% Initial Mole fractions of the reactants to check Biot Number limitations
X(1,1)=0.005;                % Inlet NO Mole fraction
X(1,2)=0.005;                % Inlet CO Mole fraction
X(1,3)=0;                    % Inlet N2 Mole fraction
X(1,4)=0;                    % Inlet CO2 Mole fraction
X(1,5)=0.99;                 % Inlet He Mole fraction

% Initial Temperature across the reactor bed (K)
Tin=303;


%%%%%%%%%%%%%%%%%% CALCULATION OF MOLECULAR DIFFUSIVITY   %%%%%%%%%%%%%%%%%%
%%%%%%%%%%%%%%%%%%%%%%%%%%%%%%%%%%%%%%%%%%%%%%%%%%%%%%%%%%%%%%%%%%%%%%%%%%%%%%%
```

```
% Initialization Molecular mass mixture (Kg/Kmol)
MolMassMix=0;
MolMass = zeros(5);
for j=1:5
    MolMass(j)=0;
    for k=1:5
        % Calculation of Effective Collision Diameter
        EffDia(j,k)=0.5*(Dia(j)+Dia(k));
        % Calculation of Effective Molecular Weight
        EffMol(j,k)=((Mol(j)+Mol(k))/(Mol(j)*Mol(k)))^0.5;
        if j~=k
            % Effective Energy Calculation
            EffKBEp(j,k)=(1/((EpKB(j)*EpKB(k))^0.5));
        end
    end
    % Molecular Mass of individual Species in 1 kmol of mixture (Kg/Kmol)
    MolMass(j)= X(1,j)*Mol(j);
    % Calculation of Molecular Mass of Mixture (Kg/Kmol)
    MolMassMix=MolMassMix+MolMass(j);
end

% Gas Constant of Mixture (J/Kg/K)
Rmass=(Ru*1000)/MolMassMix;

% Density of the fluid (Kg/m^3)
DenF=Pres/(Rmass*Tin);

 % Initializing inlet concentrations and mass fractions for all species
 % at the initial condition
 Cin = zeros(1,5);
 Y = zeros(1,5);
 KBTEp = zeros(5,5);
 Ohm = zeros(5,5);
 Diff = zeros(5,5);
 DiffMix = zeros(5);
 Dm = zeros(5);
 DKn = zeros(5);

 for j=1:5
    % Inlet Concentration of Individual Species at first node (mol/m^3)
    Cin(1,j)=(DenF/MolMassMix)*X(1,j)*1000;
    % Mass Fraction of Individual Species at first node
    Y(1,j)=(X(1,j)*Mol(j))/MolMassMix;
 end

% Calculating Binary Molecular diffusivity of the species
for j=1:5
    for k=1:5
        % Inverse Energies
        KBTEp(j,k)=(EffKBEp(j,k)*Tin);
        % Calculation of Omega
        if KBTEp(j,k)<5
            Ohm(j,k)=1.4803*(KBTEp(j,k)^-0.397);
        else
            Ohm(j,k)=1.0765*(KBTEp(j,k)^-0.16);
```

```
        end
        % Calculation of Indiviual Diffusion (m^2/sec)
        Diff(j,k)=(0.000000186*Tin^1.5*EffMol(j,k))/(Pres*(9.87*10^-
6)*EffDia(j,k)^2*Ohm(j,k));
        % Assign binary diffusions equal to zero when it goes to infinity
        if Diff(j,k)==inf
            Diff(j,k)=0;
        end
        Naa=isnan(Diff(j,k));
        if Naa==1
        Diff (j,k)=0;
        end
    end
end

% Calculating Molecular Diffusivity of the species in mixture
 for j=1:5
    for k=1:5
        if j~=k
            % Diffusion in Mixture
            DiffMix(j)= DiffMix(j)+(X(1,k)/Diff(j,k));
        end
    end
     DiffMix(j)=((1-Y(1,j))/DiffMix(j));
     if DiffMix(j)==inf
         DiffMix(j)=0;
     end
     Na=isnan(DiffMix(j));
     if Na==1
         DiffMix(j)=0;
     end
 end

% Molecular diffusivity of each species (m^2/sec)

 for j=1:5
 Dm(j) = DiffMix(j);
 end


%%%%%%%%%%%%%%%%% CALCULATION OF KNUDSEN DIFFUSIVITY   %%%%%%%%%%%%%%%%%%%
%%%%%%%%%%%%%%%%%%%%%%%%%%%%%%%%%%%%%%%%%%%%%%%%%%%%%%%%%%%%%%%%%%%%%%%%%%

% Calculation of Knudsen Diffusivity of each species (m^2/sec)
% Ref: Hayes and Kolaczkowski_ Introduction to catalytic combustion

for j=1:5
DKn(j) = (dp/3)*sqrt((8* Ru * 10^3 * Tin)/(3.14* MolMass(j)));
if DKn(j)==inf
   DKn(j)=0;
end
Na=isnan(DKn(j));
if Na==1
    DKn(j)=0;
```

```
end
end
%%%%%%%%%%%%%%%%%%%%%%%%%%%%%%%%%%%%%%%%%%%%%%%%%%%%%%%%%%%%%%%%%%%%%%%%%%%%%%%%


% To check the ratio of the diffusivities of each species less than 0.1 for
% having reasonably very less deviation on the radial direction
% Ref: Desmet et al.2003_Chem.Eng.Sci_V58_3203
e(j)=0;
for j=1:5
e(j) = DKn(j) /Dm(j);
end
if e(j) < 0.1
    disp ('The ratio of diffusivity is less than 0.1 and lumped model of the
species equation can be used');
end

%%%%%%%%%%%%%%%%% CALCULATION OF EFFECTIVE DIFFUSIVITY   %%%%%%%%%%%%%%%%%%%
%%%%%%%%%%%%%%%%%%%%%%%%%%%%%%%%%%%%%%%%%%%%%%%%%%%%%%%%%%%%%%%%%%%%%%%%%%%%%%%%

% Effective diffusivities of the species in m^2/sec (series Pore Model)
Deff(j)=0;
for j=1:5
    Deff(j) = ((DKn(j)*Dm(j))*E)/((DKn(j)*TorF)+(KnTorF*Dm(j)));
end

% Schmidt number for each species
Sc(j)=0;
for j=1:5
    Sc(j) = (DyVis)/(DenF*Deff(j));
    if Sc(j)==inf
         Sc(j)=0;
     end
     Na=isnan(Sc(j));
     if Na==1
         Sc(j)=0;
     end
end


%%%%%%%%%%%%%%%%  CALCULATION OF REYNOLDS NUMBER   %%%%%%%%%%%%%%%%%%%%%%%%%

% Reynolds number for packed bed reactor
% When Reynolds number of the reactor is greater than 50, we can neglect
% axial dispersion of heat in the energy equation. Ref: Borkink,J.G.H_1991

Re = (D*u*DenF)/(DyVis);
if Re > 20
    disp('Neglect Axial dispersion effect in the energy equation');
end

% Reynolds number for packed bed particles
Rep = (db*u*DenF)/(DyVis);
```

```
%%%%%%%%%%%%%%%%  CALCULATION OF MASS BIOT NUMBER  %%%%%%%%%%%%%%%%%%%%%%%%
%%%%%%%%%%%%%%%%%%%%%%%%%%%%%%%%%%%%%%%%%%%%%%%%%%%%%%%%%%%%%%%%%%%%%%%%%%%

% Calculation of j-factor for finding species mass transfer
jD =  (0.667)/(E*((Rep)^0.481));

% Calculation of Species mass transfer for each species (m/s)
km = zeros(5);
for j=1:5
km(j) = (jD*E*u)/((Sc(j))^0.66667);
if km(j)==inf
   km(j)=0;
end
   Na=isnan(km(j));
   if Na==1
      km(j)=0;
   end
end

% Characteristic length (m)
Lm = (Tor*(db/2));

% To ensure the model validity - Checking Mass Transfer Biot number for
% each species
Bim = zeros(5);
for j=1:5
Bim(j) = ((km(j) * Lm)/Deff(j));
Na=isnan(Bim(j));
if Na==1
    Bim(j)=0;
end
end

% Mass Biot number for each species should be less than 10 for neglecting
% radial diffusion effect-Ref: Venderbosch et al.Chem.Eng.Sci._V53_19_3355.

if Bim(j) < 10
    disp ('Mass Transfer Biot number is less than 10');
    disp ('Neglect diffusion effect of the species in the radial direction');
else
    disp ('1-D model is invalid')
    disp ('Please use 2-D model with radial effect')
    pause(30)
end


%%%%%%%%%%%%%%%%  CALCULATION OF HEAT BIOT NUMBER  %%%%%%%%%%%%%%%%%%%%%%%%
%%%%%%%%%%%%%%%%%%%%%%%%%%%%%%%%%%%%%%%%%%%%%%%%%%%%%%%%%%%%%%%%%%%%%%%%%%%

% Characteristic length for finding thermal biot number in (m)
Lt = D/4;
```

```
% Nusselt number for finding heat transfer coefficient using Li and
% Finlayson Correlation (1977)
Nu = 0.17*(Rep)^0.79;

% Heat transfer coefficient on outside of the reactor (W/m2/K)
hcoff = (Nu*Kg)/Lt;

% Parallel flow model to find effective conductivity (W/m/K)
% Ref: Nield and Bejan_2006_Convection in Porous Media
Keff = Kg*(1+(3*(1-E)*((Kp/Kg)-1))/(3+E*((Kp/Kg)-1)));
% Keff = (E*Kg)+((1-E)*Kp);

% To neglect the external heat transfer term check thermal Biot number
% Ref: Finlayson1971_Packedbedanalysis_Chem.Eng.Sci_V26_1081, Ref: Ferguson
% andFinlayson1974_NO-COmodeling_AIChE_V20_3_539
Bih = (hcoff*D)/(2*Keff);

if Bih < 1
    disp ('Wall Heat transfer Biot Number is less than 1 and so, neglect the
radial effect of temperature change in the reactor');
else
    disp ('1-D model is invalid')
    disp ('Please use 2-D model with radial effect')
    pause(30)
end

% To neglect intraparticle gradients (or) lumping pellets and bulk into
% same temperature. The Particle Biot number condition will check this
% statement. Ref: Ruud.J.Wijngaarden and
% K.RoelWesterterp1993_Chem.Eng.Technol.V16_363
Bihp = (hcoff*db)/Kp;

if Bihp < 0.1
    disp('Temperature in bulk and pellet surface can be lumped in the energy
equation')
else
    disp('Two phase temperatures for pellet and bulk should be used for the
energy equation')
    pause(30)
end

% If the Biot number ratios of mass and heat transfer is approximately
% equal to ten, then the concentration and temperature profiles over the
% catalyst radius have very less gradients. ref: Venderbosch et al.
% Chem.Eng.Sci._V53_19_3355.

Biratio(j)=0;
for j=1:5
Biratio(j) = Bim(j)/Bih;
Biratio(j)= round(Biratio(j));
end
if ((Biratio(1))&&(Biratio(2))) < 10
   disp ('The lumped model derived for the packed bed model can be used');
```

```
end

%%%%%%%%% Calculating Constant Specific Heat for Gas at Node 1: %%%%%%%%%%

Cp(1,1)=Ru*(a11+a12*Tin+a13*Tin*Tin+a14*Tin*Tin*Tin+a15*Tin*Tin*Tin*Tin);
Cp(1,2)=Ru*(a21+a22*Tin+a23*Tin*Tin+a24*Tin*Tin*Tin+a25*Tin*Tin*Tin*Tin);
Cp(1,3)=Ru*(a31+a32*Tin+a33*Tin*Tin+a34*Tin*Tin*Tin+a35*Tin*Tin*Tin*Tin);
Cp(1,4)=Ru*(a41+a42*Tin+a43*Tin*Tin+a44*Tin*Tin*Tin+a45*Tin*Tin*Tin*Tin);
Cp(1,5)=Ru*(a51+a52*Tin+a53*Tin*Tin+a54*Tin*Tin*Tin+a55*Tin*Tin*Tin*Tin);
Cpmix=0;

% Calculation of Constant Pressure Specific Heat Mol Basis (KJ/Kmol.K)
for j=1:5
   Cpmix=Cpmix+Cp(1,j)*X(1,j);
end

% Calculation of Constant Pressure Specific Heat kg basis (J/Kg.K)
Cpmixmass=Cpmix*1000/MolMassMix;

% Volumetric ratio of heat capacities by Ferguson
% andFinlayson1974_NO-COmodeling_AIChE_V20_3_539
Cr = (E*DenF*Cpmixmass)/((1-E)*DenP*Cpp);
if Cr < 0.002
    disp ('Fluid phase heat capacity term in the energy equation can be
neglected');
else
    disp ('Fluid phase heat capacity term in the energy equation is
considered in the energy equation and not neglected');
end

%%%%%%%%%%%%%%%%%%%%%%%%%%%%%%%%%%%%%%%%%%%%%%%%%%%%%%%%%%%%%%%%%%%%%%%%%%%%
disp('Simulation paused for 40 secs to view the limitation conditions used
for the model');
pause(40)
%%%%%%%%%%%%%%%%%%%%%%%%%%%%%%%%%%%%%%%%%%%%%%%%%%%%%%%%%%%%%%%%%%%%%%%%%%%%

% Initialization of various parameters of the reactor bed before simulation
for i=1:h
    % Initial Temperature Values Across the reactor in K
    Tia(i)= 303;
    % Initialization of Reaction Rate at Various Nodes
    RR(i)=0;

    % Partial Pressure of the reactants (atm)
    P(1)=0;          % Inlet NO partial pressure
    P(2)=0;          % Inlet CO partial pressure
    P(3)=0;          % Inlet N2 partial pressure
    P(4)=0;          % Inlet CO2 partial pressure
    P(5)=1;          % Inlet NO partial pressure

    % Initial Mole fractions of the reactants
    X(i,1)=0;        % Inlet NO Mole fraction
    X(i,2)=0;        % Inlet CO Mole fraction
    X(i,3)=0;        % Inlet N2 Mole fraction
```

```
    X(i,4)=0;         % Inlet CO2 Mole fraction
    X(i,5)=1;         % Inlet He Mole fraction

    % Initializing inlet concentrations and mass fractions for all
    % species at the initial condition
    MolMassMix=0;

    for j=1:5
    % Molecular Mass of Individual Species in 1 Kmol of Mixture(Kg/Kmol)
    MolMasss(i,j)= X(i,j)*Mol(j);
    % Calculation of Molecular Mass of Mixture (Kg/Kmol)
    MolMassMix=MolMassMix+MolMasss(i,j);
    end

    % Gas Constant of Mixture (J/Kg/K)
    Rmass=(Ru*1000)/MolMassMix;
    % Density of the fluid (Kg/m^3)
    DenF=Pres/(Rmass*Tin);

    % Inlet Concentration of Individual Species at first node (mol/m^3)
    for j=1:5
    Concc(i,j)=(DenF/MolMassMix)*X(i,j)*1000;
    Na=isnan(Cin(1,j));
    if Na==1
        Concc(i,j)=0;
    end

    % Mass Fraction of Individual Species at first node
    Y(i,j)=(X(i,j)*Mol(j))/MolMassMix;
    Na=isnan(Y(i,j));
    if Na==1
        Y(i,j)=0;
    end
    end
end

% Option for ODE Solver
options=odeset('RelTol',1e-6,'Stats','on');

%%%%%%%  Starting calculation for Initial time step at first node  %%%%%%%%
%%%%%%%%%%%%%%%%%%%%%%%%%%%%%%%%%%%%%%%%%%%%%%%%%%%%%%%%%%%%%%%%%%%%%%%%%%

% Initial Mole fractions of the reactants.
    X(1,1)=0.005;           % Inlet NO Mole fraction
    X(1,2)=0.005;           % Inlet CO Mole fraction
    X(1,3)=0;               % Inlet N2 Mole fraction
    X(1,4)=0;               % Inlet CO2 Mole fraction
    X(1,5)=0.99;            % Inlet He Mole fraction

    % Initializing inlet concentrations and mass fractions for all
    % species at the initial condition

    MolMassMix=0;
    Cinp = zeros(10,5);
```

```
    Cinpp = zeros(10,5);

    for j=1:5
    % Molecular Mass of Individual Species in 1 Kmol of mixture (Kg/Kmol)
    MolMasss(1,j)= X(1,j)*Mol(j);
    % Calculation of Molecular Mass of Mixture (Kg/Kmol)
    MolMassMix=MolMassMix+MolMasss(1,j);
    end

    % Temperature at node 1 (K)
    Tia(1)=423;
    % Gas Constant of Mixture (J/Kg/K)
    Rmass=(Ru*1000)/MolMassMix;
    % Density of the fluid (Kg/m^3)
    DenF=Pres/(Rmass*Tia(1));

    % Inlet Concentration of Individual Species at first node (mol/m^3)
    for  j=1:5
    Concc(1,j)=(DenF/MolMassMix)*X(1,j)*1000;
    Na=isnan(Cin(1,j));
    if Na==1
    Concc(1,j)=0;
    end
    end

    for i=2:h
        for j=1:5
          Cinp(i,j)=Concc(i,j);
          Cinpp(i,j)=Concc(i,j);
        end
    end
%%%%%%%% Calculating Constant Specific Heat for Gas at Node 1: %%%%%%%%%%

Cp(1,1)=Ru*(a11+a12*Tia(1)+a13*Tia(1)*Tia(1)+a14*Tia(1)*Tia(1)*Tia(1)+a15*Tia
(1)*Tia(1)*Tia(1)*Tia(1));
Cp(1,2)=Ru*(a21+a22*Tia(1)+a23*Tia(1)*Tia(1)+a24*Tia(1)*Tia(1)*Tia(1)+a25*Tia
(1)*Tia(1)*Tia(1)*Tia(1));
Cp(1,3)=Ru*(a31+a32*Tia(1)+a33*Tia(1)*Tia(1)+a34*Tia(1)*Tia(1)*Tia(1)+a35*Tia
(1)*Tia(1)*Tia(1)*Tia(1));
Cp(1,4)=Ru*(a41+a42*Tia(1)+a43*Tia(1)*Tia(1)+a44*Tia(1)*Tia(1)*Tia(1)+a45*Tia
(1)*Tia(1)*Tia(1)*Tia(1));
Cp(1,5)=Ru*(a51+a52*Tia(1)+a53*Tia(1)*Tia(1)+a54*Tia(1)*Tia(1)*Tia(1)+a55*Tia
(1)*Tia(1)*Tia(1)*Tia(1));
Cpmix=0;

% Calculation of Constant Pressure Specific Heat Mol Basis (KJ/Kmol.K)
for j=1:5
   Cpmix=Cpmix+Cp(1,j)*X(1,j);
end

% Calculation of Constant Pressure Specific Heat kg basis (J/Kg.K)
Cpmixmass=Cpmix*1000/MolMassMix;

% 'AConstant' is used in the energy equation
```

```
Aconstant = ((1- E)* DenP * Cpp)+(E*DenF*Cpmixmass);
% 'Bconstant' for finding time step in energy equation
Bconstant = (E*DenF*Cpmixmass)/(((1- E)* DenP * Cpp)+(E*DenF*Cpmixmass));

%%%%%%%%%% Defining the Time Difference for Temperature Modeling %%%%%%%%%%
delt=(2*Keff)/(Aconstant*(Bconstant^2)*(u^2));
delt1 = ((dx^2)*(Aconstant))/(Keff);

% The above equation is used for finding time step which provides the
% minimum value for the time step and thus, used for modeling purposes
% Defining the Time Step as Per Input File
 if delt1 > 0.25
  TimeStep=0.25;
 else
    TimeStep=0.1;
    TempStep = (2/60)* TimeStep;
    disp ('Change the Temperature step value to:');
    disp(TempStep);
    pause(30)
 end
 if (TimeStep < delt)&&(TimeStep < delt1)
  dt=TimeStep;
 else
   disp ('Check the time step for stability conditions');
   pause (100)
 end

% Defining the Initial Value for Time
a=1;

%%%%%%%%%%%%%%%%%%%%%%%%%%%%%%%%%%%%%%%%%%%%%%%%%%%%%%%%%%%%%%%%%%%%%%%%%%%%
%%%%%   TEMPERATURE AND SPECIES MODELING FROM NODES '2' to 'h' FOR    %%%%%
%%%%%   EACH TIME STEP - INCREMENT BASED ON STABILITY CONDITIONS      %%%%%
%%%%%%%%%%%%%%%%%%%%%%%%%%%%%%%%%%%%%%%%%%%%%%%%%%%%%%%%%%%%%%%%%%%%%%%%%%%%

 % Pre-allocate variables for the maximum possible time and space steps
 Hp = zeros(10,5);
 THR = zeros(10,1);
 Hcond = zeros(10,1);
 Hconv = zeros(10,1);
 Tf = zeros(10,1);
 Cinn = zeros(10,5);
 B = zeros(5);
 C = zeros(10,5);
 MolMasss = zeros(10,5);
 Dm = zeros(10,5);
 DKn = zeros(10,5);

for T=423:0.0083333:573                                    % 2 degree K/min
    % If the time step(dt) is 0.1, then use temperature rise step as 0.0033

    % Initial Mole fractions is equal to the initial partial pressures of
    % NO and CO provided and the reactor operates at 1 atm pressure
```

```
    % Calculation of Pellet Temperature at Next Time Step.
    for i=2:h

        % Calculation of Enthalpy for each species (J/kg)
        % Calculation of Enthalpy for NO

Hp(i,1)=Ru*Tia(i)*(a11+((a12*Tia(i))/2)+(a13*Tia(i)*Tia(i)/3)+(a14*Tia(i)*Tia
(i)*Tia(i)/4)+(a15*Tia(i)*Tia(i)*Tia(i)*Tia(i)/5)+(a16/Tia(i)));
        % Calculation of Enthalpy for CO

Hp(i,2)=Ru*Tia(i)*(a21+((a22*Tia(i))/2)+(a23*Tia(i)*Tia(i)/3)+(a24*Tia(i)*Tia
(i)*Tia(i)/4)+(a25*Tia(i)*Tia(i)*Tia(i)*Tia(i)/5)+(a26/Tia(i)));
        % Calculation of Enthalpy for N2

Hp(i,3)=Ru*Tia(i)*(a31+((a32*Tia(i))/2)+(a33*Tia(i)*Tia(i)/3)+(a34*Tia(i)*Tia
(i)*Tia(i)/4)+(a35*Tia(i)*Tia(i)*Tia(i)*Tia(i)/5)+(a36/Tia(i)));
        % Calculation of Enthalpy for CO2

Hp(i,4)=Ru*Tia(i)*(a41+((a42*Tia(i))/2)+(a43*Tia(i)*Tia(i)/3)+(a44*Tia(i)*Tia
(i)*Tia(i)/4)+(a45*Tia(i)*Tia(i)*Tia(i)*Tia(i)/5)+(a46/Tia(i)));
        % Calculation of Enthalpy for He

Hp(i,5)=Ru*Tia(i)*(a51+((a52*Tia(i))/2)+(a53*Tia(i)*Tia(i)/3)+(a54*Tia(i)*Tia
(i)*Tia(i)/4)+(a55*Tia(i)*Tia(i)*Tia(i)*Tia(i)/5)+(a56/Tia(i)));

        % Total Heat Released from NO - CO reaction
        THR(i)=(-Hp(i,1)*RR(i))-
(Hp(i,2)*RR(i))+(Hp(i,3)*RR(i)*0.5)+(Hp(i,4)*RR(i));

        if i<h
            % Heat From Conduction
            Hcond(i)=(((Keff*dt)/(Aconstant*dx*dx))*(Tia(i+1)-
(2*Tia(i))+(Tia(i-1))));
            % Heat From Convection
            Hconv(i)=(((u*Bconstant*dt)/(2*dx))*(Tia(i+1)-Tia(i-1)));
            % Calculations of pellet reactor at new node
            Tf(i)=Tia(i)-Hconv(i)+ Hcond(i)-((dt/Aconstant)*THR(i));
        else
            % Heat From Conduction
            Hcond(i)=(((2*Keff*dt)/(Aconstant*dx*dx))*(Tia(i-1)-Tia(i)));
            % Heat From Convection
            Hconv(i)=0;
            % End Boundary Condition for pellet reactor at the end
            Tf(i)=Tia(i)-Hconv(i)+ Hcond(i)-((dt/Aconstant)*THR(i));
        end
    end

    Tia(1)=T;
    for i=2:h
        Tia(i)=Tf(i);
    end

%%%%%%%%%%%%%%%%%%%%%%%%%     SPECIES MODELING      %%%%%%%%%%%%%%%%%%%%%%%%%%
```

```
  % While loop to make the species concentrations from nodes '2' to 'h'
  % steady state for the corresponding temperature

delc = 1;
while delc > 0.0000000001
  for i=2:h

     for j=1:5
     % Molecular Mass of Individual Species in 1 Kmol of Mixture (Kg/Kmol)
     MolMasss(i,j)= X(i,j)*Mol(j);
     % Calculation of Molecular Mass of Mixture (Kg/Kmol)
     MolMassMix=MolMassMix+MolMasss(i,j);
     end

  % Calling Molecular diffusivity calculator Function
  [DiffMix]=MolecularDiffusion(Tia,X,Y);

  for j=1:5
      % Molecular diffusivity of each species at each node (m^2/sec)
      Dm(i,j)=DiffMix(j);

      % Knudsen Diffussivity of each species at each node (m^2/sec)
      DKn(i,j) = (dp/3)*sqrt((8* Ru * 10^3 * Tia(i))/(3.14* MolMasss(i,j)));
      if DKn(i,j)==inf
        DKn(i,j)=0;
      end
        Na=isnan(DKn(i,j));
      if Na==1
        DKn(i,j)=0;
      end

      % Effective diffusivity of each species  at each node (m^2/sec)
      Deff(i,j) = ((DKn(i,j)*Dm(i,j))*E)/(DKn(i,j)*TorF)+(KnTorF*Dm(i,j));
  end

  % Solving Concentration at each nodes for the corresponding temperature
  delb = 1;
  % While loop used to obtain steady state solution
  while delb > 0.0000000001
       % Calling ODE Solver for the corresponding node
       [t,Z]=ode15s(@SpeciesODE, [0 dt],Cinp(i,:), options);
       [m,n]=size(Z);
           % Putting the Values back in designated species
           Cinn(i,1)=Z(m,1);
           Cinn(i,2)=Z(m,2);
           Cinn(i,3)=Z(m,3);
           Cinn(i,4)=Z(m,4);
           Cinn(i,5)=Z(m,5);
       for j=1:5
       % Calculate error to make concentration steady state at that node
           B(j)=abs(Cinn(i,j)-Cinp(i,j));
           Concc(i,j)=Cinn(i,j);
           Cinp(i,j)=Cinn(i,j);
       end
```

```
        % The maximum value in the array is compared with 'delb'
        delb=max(B);
    end

   end

   for i=2:h
    for j=1:5
        % Calculate error to make concentration steady state at all nodes
        C(i,j)=abs(Concc(i,j)-Cinpp(i,j));
        Cinpp(i,j)=Concc(i,j);
    end
   end
   % The maximum value in the array is compared with 'delc'
   delc=max(C);

 end
    % Store Temperature each cycle
    Tempp(a,1)=T;
    % Store: NO and CO conversions of the packed bed reactor (%)
    NOConv(a,1)=((Concc(1,1)-Cinpp(h,1))/Concc(1,1))*100;
    COConv(a,2)=((Concc(1,2)-Cinpp(h,2))/Concc(1,2))*100;

    % Increment the counter step by 1
    a = a + 1;
end

% Plot for Temperature Vs Concentration of NO
    figure;
    plot(Tempp(:,1),NOConv(:,1))
    xlabel('Inlet Temperature (K)')
    ylabel('Conversion of NO in (%)')
    legend('NO Conversion Curve')
    axis([423 573 0 100])
    title('Conversion Curve for NO reduction by CO')

% Plot for Temperature Vs Concenration of CO
    figure;
    plot(Tempp(:,1),COConv(:,2))
    xlabel('Inlet Temperature (K)')
    ylabel('Conversion of CO in (%)')
    legend('CO Conversion Curve')
    axis([423 573 0 100])
    title('Conversion Curve for NO reduction by CO')

% Provides total process time of the model
SimulationTime = toc;

%End Program
```

C.2. ODE15s sub-routine for calculating species concentrations:

```
%%%%%%%%%%%%%%%%%%%%%%%%%%%%%%%%%%%%%%%%%%%%%%%%%%%%%%%%%%%%%%%%%%%%%%%%%%%%
%%%%%%%%%%%%%%%%%%%%  ODE SOLVER FOR SPECIES EQUATION   %%%%%%%%%%%%%%%%%%%%
%%%%%%%%%%%%%%%%%%%%%%%%%%%%%%%%%%%%%%%%%%%%%%%%%%%%%%%%%%%%%%%%%%%%%%%%%%%%


% ODE Function to solve concentration of the species for the corresponding
% node and temperature
function dZdt = SpeciesODE(t,Z)

% Defining Global Variables
  global E
  global Deff
  global Tia
  global i
  global u
  global Concc
  global Ru
  global dx
  global RR
  global h
  global Pres

% Assigning Numbers to Species
% 1:NO
% 2:CO
% 3:N2
% 4:CO2
% 5:He

% Getting the Initial Values from array
Cs(1)=Z(1);
Cs(2)=Z(2);
Cs(3)=Z(3);
Cs(4)=Z(4);
Cs(5)=Z(5);

% Values from Granger et. al.
% Pre-Exponential factor (mol/m^2.sec) => Conversion from (mol/gm/hr)
% ((7.4453657*10^21)*0.023)/(3600*3.14*0.012*0.003)
PreExp=0.33*10^21;
% Activation Energy in J/mol which is 47kcal/mol for NO dissociation step
Ea =196648;
% Per Atmosphere
ANO=2.4*10^-2;
% The Enthalpy is calculated using the equation given by Granger et al.
% 2001_TPDstudies_Topicsofcatalysis_V16-17_394.
% Enthalpy for NO and CO are calculated based on their partial pressures
% and correlation factors given in Granger et al.2001. This correlation
% takes care of the influence of partial pressures and temperature on the
% reactor

% Enthalpy of NO in J/mol
HNO=-48576;
% Equilibrium Constant of NO
```

```
KNO=ANO*exp(((-1)*(HNO))/(Ru*Tia(i)));
% Per Atmosphere
ACO=1.4*10^-2;
% Enthalpy of CO in J/mol
HCO=-32554;
% Equilibrium Constant of CO
KCO=ACO*exp(((-1)*(HCO))/(Ru*Tia(i)));

%Partial pressures for calculating reaction rates
Ctot = 0;
for j=1:5
    Ctot = Ctot + Cs(j);
end

PP(1)=(9.86923*(10^-6)*Pres)*(Cs(1)/Ctot);
PP(2)=(9.86923*(10^-6)*Pres)*(Cs(2)/Ctot);
if PP(1)<0
    PP(1)=0;
end
if PP(2)<0
    PP(2)=0;
end

% Reaction Rate Expression for NO dissociation step
% Ref: AnandSrinivasanandDr.Depcik2010_Cat.Rev.Sci.Eng._V52_1-32
RR(i)=((PreExp * exp(-1*((Ea)/(Ru*Tia(i))))
*(KNO*PP(1)))/((1+(KNO*PP(1))+(KCO*PP(2)))^2));

%Calculation of Concentrations for the corresponding time step
if i<h

dZdt(1)=-((((Cs(1))-(Concc((i-1),1)))*E*u)/(dx))
+(Deff(i,1)*E*((Concc((i+1),1))-(2*Cs(1))+(Concc((i-1),1)))/(dx^2))-(RR(i));
dZdt(2)=-((((Cs(2))-(Concc((i-1),2)))*E*u)/(dx))
+(Deff(i,2)*E*((Concc((i+1),2))-(2*Cs(2))+(Concc((i-1),2)))/(dx^2))-(RR(i));
dZdt(3)=-((((Cs(3))-(Concc((i-1),3)))*E*u)/(dx))+(Deff(i,3)*E*
((Concc((i+1),3))-(2*Cs(3))+(Concc((i-1),3)))/(dx^2))+(0.5*RR(i));
dZdt(4)=-((((Cs(4))-(Concc((i-1),4)))*E*u)/(dx))+(Deff(i,4)*E*
((Concc((i+1),4))-(2*Cs(4))+(Concc((i-1),4)))/(dx^2))+(RR(i));
dZdt(5)=-((((Cs(5))-(Concc((i-1),5)))*E*u)/(dx))+(Deff(i,5)*E*
((Concc((i+1),5))-(2*Cs(5))+(Concc((i-1),5)))/(dx^2));

% Concentration calculation for the node i=h (or) last node of
% the reactor using Neumann boundary condition
else

dZdt(1)=-((((Cs(1))-(Concc((i-1),1)))*E*u)/(dx))+(Deff(i,1)*E*((2*Concc((i-
1),1))-(2*Cs(1)))/(dx^2))-(RR(i));
dZdt(2)=-((((Cs(2))-(Concc((i-1),2)))*E*u)/(dx))+(Deff(i,2)*E*((2*Concc((i-
1),2))-(2*Cs(2)))/(dx^2))-(RR(i));
dZdt(3)=-((((Cs(3))-(Concc((i-1),3)))*E*u)/(dx))+(Deff(i,3)*E*((2*Concc((i-
1),3))-(2*Cs(3)))/(dx^2))+(0.5*RR(i));
dZdt(4)=-((((Cs(4))-(Concc((i-1),4)))*E*u)/(dx))+(Deff(i,4)*E*((2*Concc((i-
1),4))-(2*Cs(4)))/(dx^2))+(RR(i));
```

```
dZdt(5)=-((((Cs(5))-(Concc((i-1),5)))*E*u)/(dx))+(Deff(i,5)*E*((2*Concc((i-
1),5))-(2*Cs(5)))/(dx^2));

end

dZdt=dZdt';
```

C.3. Sub-routine for calculating molecular diffusivity of the species:

```
%%%%%%%%%%%%%%%%%%%%%%%%%%%%%%%%%%%%%%%%%%%%%%%%%%%%%%%%%%%%%%%%%%%%%%%%%%%%
%%%%%%%%%%%%%%%%%%%%%%%%  MOLECULAR DIFFUSIVITY   %%%%%%%%%%%%%%%%%%%%%%%%%%
%%%%%%%%%%%%%%%%%%%%%%%%%%%%%%%%%%%%%%%%%%%%%%%%%%%%%%%%%%%%%%%%%%%%%%%%%%%%


% Function for calculating Molecular Diffusion for NO-CO species
function [DiffMix]=MolecularDiffusion(Tia,X,Y)

global i
global EffDia
global EffMol
global EffKBEp
global Pres

KBTEp=zeros(5,5);
Ohm=zeros(5,5);
Diff=zeros(5,5);
DiffMix=zeros(5);

% Binary Diffusion of Species (m^2/sec)

for n=1:5
    for k=1:5
        % Inverse Energies
        KBTEp(n,k)=(EffKBEp(n,k)*Tia(i));
        % Calculation of Omega
        if KBTEp(n,k)<5
            % Equation from Curve Fitting in Excel
            Ohm(n,k)=1.4803*(KBTEp(n,k)^-0.397);
        else
            % Equation from Curve Fitting in Excel
            Ohm(n,k)=1.0765*(KBTEp(n,k)^-0.16);
        end
        % Calculation of Binary Diffusion (m^2/sec)
        Diff(n,k)=(0.000000186*Tia(i)^1.5*EffMol(n,k))/(Pres*(9.87*10^-
6)*EffDia(n,k)^2*Ohm(n,k));
        % 'Not-a-number' values are checked in the array and assigned to be
        % zero
        if Diff(n,k)==inf
            Diff(n,k)=0;
        end
        Naa=isnan(Diff(n,k));
        if Naa==1
         Diff (n,k)=0;
        end
    end
```

```
end

% Diffusion of Species in mixture

  for n=1:5
     % Initialization
     DiffMix(n)=0;
     for k=1:5
        if n~=k
            % Diffusion in Mixture
            DiffMix(n)= DiffMix(n)+(X(i,k)/Diff(n,k));
        end
    end
     DiffMix(n)=((1-Y(i,n))/DiffMix(n));
     % 'Not-a-number' values are checked in the array and assigned to be zero
     if DiffMix(n)==inf
         DiffMix(n)=0;
     end
     Na=isnan(DiffMix(n));
     if Na==1
         DiffMix(n)=0;
     end
 end
end
```

REFERENCES

[1] Schlatter, J. C.; Sinkevitch, R. M.; Mitchell, P. J. Laboratory reactor system for three-way automotive catalyst evaluation. Ind. Eng. Chem. Prod. Res. Dev., **1983**, *22* (1), 51-56.

[2] Kaspar, J.; Fornasiero, P.; Hickey, N. Automotive catalytic converters: current status and some perspectives. Catal. Today **2003**, *77*, 419-449.

[3] EPA. National summary of carbon monoxide emissions. **2008** U.S. EPA

[4] EPA. National Summary of Nitrogen Oxides Emissions. **2008** http://www.epa.gov/air/emissions/nox.htm

[5] Iordanidis, A. A. Ph. D. Thesis, Chemical Engineering, University of Twente, Enschede, 2002.

[6] Bourane, A.; Bianchi, D. Oxidation of CO on A Pt/Al_2O_3 Catalyst: From the Surface Elementary Steps to Light-Off Tests - V. Experimental and Kinetic Model for light-off tests in excess of O_2. Journal of Catalysis **2004**, *222* (2), 499-510.

[7] Winterberg, M.; Tsotsas, E.; Krischke, A.; Vortmeyer, D. A simple and coherent set of coefficients for modelling of heat and mass transport with and without chemical reaction in tubes filled with spheres. Chem. Eng. Sci. **2000**, *55*, 967-979.

[8] Desmet, G.; De Greef, J.; Verelst, H.; Baron, G. V. Performance limits of isothermal packed bed and perforated monolithic bed reactors operated under laminar flow conditions. Part II. Performance comparsion and design considerations. Chem. Eng. Sci. **2003**, *58*, 3203-3214.

[9] Antwerpen, W. V.; Toit, C. G.; Rousseau, P. G. A review of correlations to model the packing structure and effective thermal conductivity in packed beds of mono-sized spherical particles. Nuclear Engineering and Design **2010**, *240*, 1803-1818.

[10] Kaspar, J.; Leitenburg, C.; Fornasiero, P.; Trovarelli, A.; Graziani, M. NO reduction by CO over Rh/Al_2O_3. Effects of rhodium dispersion on the catalytic properties. J. Catal. **1994**, *146*, 136-147.

[11] Olsson, L.; Andersson, B. Kinetic modeling in automotive catalysis. Topics in Catalysis **2004**, *28* (1), 89-98.

[12] Heck, R. H.; Wei, J.; Katzer, J. R. Mathematical modeling of monolithic catalysts. A.I.Ch.E. Journal **1976**, *22* (3), 477-484.

[13] Harned, J. L. Analytical evaluation of a catalytic converter system. SAE Paper 720520 **1972**.

[14] Oh, S. H.; Cavendish, J. C. Transients of Monolithic Catalytic Converters: Response to step Changes in Feedstream temperature as related to controlling automobile emissions. Industrial and Engineering Chemistry Research **1982**, *21* (1), 29-37.

[15] Shelef, M.; Graham, G. W. Why rhodium in automotive three-way catalysts? Cat. Rev. Sci. Eng. **1994**, *36* (3), 433-457.

[16] Cant, W. N.; Angove, E. D.; Chambers, C. D. Nitrous oxide formation during the reaction of simulated exhaust streams over rhodium, platinum and palladium catalysts. Appl. Catal., B **1998**, *17*, 63-73.

[17] Granger, P.; Parvulescua, V. I.; Delmon, B. Catalytic removal of NO. Catal. Today **1998**, *46*, 233-316.

[18] Zaera, F.; Gopinath, S. C. Evidence for an N_2O intermediate in the catalytic reduction of NO to N_2 on rhodium surfaces. Chem. Phys. Lett. **2000**, *332*, 209-214.

[19] Granger, P.; Dhainaut, F.; Pietrzik, S.; Malfoy, P.; Mamede, A. S.; Leclercq, L.; Leclercq, G. An overview: Comparative kinetic behaviour of Pt, Rh and Pd in the NO+CO and NO+H_2 reactions. Top. Catal. **2006**, *39* (1-2), 65-77.

[20] Na-Ranong, D.; Yuangsawad, R.; Kitchaiya, P.; Aida, T. Application of periodic operation to kinetic study of NO–CO reaction over Rh/Al_2O_3. Chem. Eng. J. **2009**, *146*, 275–286.

[21] Zhdanov, V. P. Kinetic oscillations on nm-sized catalyst particles: NO reduction by CO on Pt. Catal. Lett. **2004**, *93* (3-4).

[22] B.Mantri, D.; Aghalayam, P. Micro-Kinetic Study of Reduction of NO on Pt Group Catalysts. Int. J. Chem. Reactor Eng. **2007**, *5*, 1-27.

[23] Depcik, C.; Loya, S.; Srinivasan, A. In *ASME International Mechanical Engineering Congress & Exposition*; ASME, Ed.; IMECE: Lake Buena Vista, Florida, USA, 2009; Vol. IMECE2009-11173.

[24] Jiang, Y.; Khandilkar, M. R.; Al-Dahnan, M. H.; Dudukovic, M. P. CFD of Multiphase flow in Packed-Bed Reactors. AIChE **2002**, *48*, 701.

[25] Wakao, N.; Kaguei, S. Heat and mass transfer in packed beds. Top. in Chem. Engg. **1982**, *1* (1), 1-360.

[26] Summers, J.; Hegedus, L. Effects of platinum and palladium impregnation on the performance and durability of automobile exhaust oxidizing catalysts. J. Catal. **1978**, *51*, 185.

[27] Ferguson, N. B.; Finlayson, B. A. Transient modeling of a catalytic converter to reduce nitric oxide in automobile exhaust. AIChE **1974**, *20* (3), 539-545.

[28] Froment, G. F.; Bischoff, K. B. Chemical Reactor Analysis and Design; John Wiley & Sons, **1990**; pp.

[29] Smith, J. M. Chemical Engineering Kinetics; Mc-Graw-Hill, **1981**; pp.

[30] Depcik, C.; Assanis, D. One-dimensional automotive catalyst modeling. Progress in Energy and Combustion Science **2005**, *31* (4), 308-369.

[31] Koltsakis, G. C.; Konstantinidis, P. A.; Stamatelos, A. M. Development and application range of mathematical models for TWC. Appl. Catal., B **1997**, *12*, 161-191.

[32] Srinivasan, A.; Depcik, C. Review of chemical reactions in the NO reduction by CO on rhodium/alumina catalysts. Chem. Rev. Sci. Eng. **2010**, *52* (4), 462-493.

[33] Srinivasan, A.; Depcik, C. In *Surface Reviews and Letters*; Unpublished, 2011.

[34] KITCO. Historical prices of platinum per ounce based on yearly average from 1960-2010 in US dollars **2010** http://www.kitco.com/charts/historicalplatinum.html

[35] Taylor, K. C. Nitric oxide catalysis in automotive exhaust systems. Cat. Rev. - Sci. Eng. **1993**, *35* (4), 457-481.

[36] Farrauto, R. J.; Heck, R. H.; Gulati, S. Catalytic Air Pollution Control: Commercial Technology; John Wiley & Sons, Inc.: New York, NY, **2009**; pp.

[37] Inflation-Data. Historical Consumer Price Index. **2009** InflationData.com

[38] KITCO. Historical Precious Metal Price Chart. **2009.** http://www.kitco.com/charts/historicalplatinum.html

[39] Montreuil, C. N.; Wiliams, S. C.; Adamczyk, A. A. Modeling current generation catalytic converters: laboratory experiments and kinetic parameter optimization - steady state kinetics. SAE paper 920096, **1992**.

[40] Voltz, S. Kinetic study of carbon monoxide and propylene oxidation on platinum catalyst. Ind. Eng. Chem. Prod. Res. Dev. **1973**, *12* (4), 294-303.

[41] Yang, C.; Garl, W. C. Infrared studies of carbon monoxide chemisorbed on rhodium. J. Phys. Chem. **1957**, *61* (11), 1504-1512.

[42] George, L. B.; Gregg, R. S.; Ken, N. Catalytic reduction of nitric oxide with carbon monoxide effect of oxygen. Ind. Eng. Chem. Prod. Res. Dev. **1972**, *11* (1), 54-59.

[43] Unland, M. L.; Barker, G. E. Rhodium and ruthenium catalysts in NO_x reduction; U.S. Patents: 3809743, **1974**

[44] William, H. L. Nitrogen oxides removal; Park Ridge: N.J, **1975**; 255 pp.

[45] Bevan, K. E.; William, T. Simulated performance of a diesel aftertreatment system for U.S. 2010 application. SAE 2006-01-3551, 73-81.

[46] Honda-Worldwide-Site. Next-Generation Clean Diesel Engine Capable of Meeting Stringent Tier II Bin 5 Emission Requirements in the U.S. **2006** Honda Motor Co., Ltd

[47] Johnson, T. V. Diesel emission control in review. SAE - 2006-01-0030.

[48] Kobylinski, T. P. The catalytic chemistry of NO II.Reduction of NO over noble metal catalysts. J. Catal. **1974**, *33* (3), 376-384.

[49] Hiromichi, A.; Hiroo, T. IR study of NO adsorbed on Rh/Al_2O_3 catalyst. J. Catal. **1976**, *43* (1), 131-142.

[50] Campbell, C. T.; White, J. M. Chemisorption and reactions of nitric oxide on rhodium. Appl. Surf. Sci. **1978**, *1* (3), 347.

[51] Kroeker, R. M.; Kaska, W. C.; Hansma, P. K. How CO bonds to alumina-supported rhodium particles. J. Catal. **1978**, *57*, 72-79.

[52] Solymosi, F.; Sarkany, J. An IR study of the surface interaction between NO and CO on Rh/Al_2O_3 catalyst. Appl. Surf. Sci. **1978**, *3*, 68-82.

[53] Yates Jr., J. T.; Williams, E. D.; Weinberg, W. H. Does chemisorbed carbon monoxide dissociate on rhodium? Surf. Sci. **1980**, *91* (2-3), 562-570.

[54] Baird, R. J.; Ku, R. C.; Wynblatt, P. The chemisorption of CO and NO on Rh(100). Surf. Sci. **1980**, *97* (2-3), 346-364.

[55] Dubois, L. H.; Hansma, P. K.; Somorjai, G. A. Evidence for an oxygen intermediate in the catalytic reduction of NO by CO on rhodium surfaces. J. Catal. **1980**, *65* (2), 318-327.

[56] Worley, S. D.; Rice, C. A.; Mattson, G. A.; Curtis, C. W.; Guin, J. A.; Tarrer, A. R. Effect of support material on rhodium catalysts. J. Phys. Chem. **1982**, *86* (14), 2714-2717.

[57] Edward, A. H.; Robert, R. Infrared study of the interactions between NO and CO on Rh/Al_2O_3 catalysts. J. Chem. Soc., Faraday Trans. **1984**, *80*, 531-547.

[58] Hendershot, E. R.; Hansen, S. R. Reduction of nitric oxide with carbon monoxide on the Rh(100) single-crystal surface. J. Catal. **1986**, *98* (1), 150-165.

[59] Dictor, R. An infrared study of the behavior of CO, NO and CO + NO over Rh/Al_2O_3 catalysts. J. Catal. **1988**, *109* (1), 89-99.

[60] Root, T. W.; Schmidt, L. D.; Fisher, G. B. Adsorption and reaction of nitric oxide and oxygen on Rh(111). Surf. Sci. **1983**, *134* (1), 30-45.

[61] Oh, S. H.; Fisher, G. B.; Carpenter, J. E.; Goodman, D. W. Comparative kinetic studies of carbon monoxide-oxygen and carbon monoxide-nitric oxide reactions over single crystal and supported rhodium catalysts. J. Catal. **1986**, *100* (2), 360-376.

[62] Peden, C. H. F.; Goodman, D. W.; Blair, D. S.; Berlowitz, P. J.; Fisher, G. B.; Oh, S. H. Kinetics of carbon monoxide oxidation by oxygen or nitric oxide on rhodium(111) and rhodium(100) single crystals. J. Phys. Chem. **1988**, *92* (6), 1563-1567.

[63] Schwartz, B. S.; Fisher, B. G.; Schmidt, L. D. Nitric oxide + carbon monoxide on rhodium(111): steady-state rates and adsorbate coverages. J. Phys. Chem. **1988**, *92* (2), 389-395.

[64] Carballo L. M , H. T., Lintz H. G. The low-pressure reaction of carbon monoxide with nitrogen monoxide in the presence of oxygen on polycrystalline platinum, palladium and rhodium. . Applied surface science **1989**, *40* (1-2), 53.

[65] Cho, K. B.; Shank, H. B.; Bailey, E. J. Kinetics of NO reduction by CO over supported rhodium catalysts: Isotopic cycling experiments. J. Catal. **1989**, *115* (2), 486-499.

[66] Anderson, A. J.; Millar, J. G.; Rochester, H. C. Infrared study of the adsorption of NO, NO_2 and CO on Rh/Al_2O_3 catalysts. J. Chem. Soc., Faraday Trans. **1990**, *86* (3), 571-576.

[67] Bowker, M.; Guo, Q.; Joyner, W. R. The CO/NO reaction on Rh(110). Catal. Today **1991**, *10* (3), 409-412.

[68] Donald, D. B.; Constance, J. C. Effects of high-temperature aging on the dispersion of Rh/Al_2O_3. J. Catal. **1993**, *144*, 296-310.

[69] Baraldi, A.; Dhanak, V. R.; Comelli, G.; M.Kiskinova, M.; Rosei, R. NO dissociation and NO + CO reaction in Rh(110): influence of the surface structure and composition on the reaction rates. Appl. Surf. Sci. **1993**, *68*, 395-405.

[70] Byong, K. C. Mechanistic importance of intermediate N_2O + CO reaction in overall NO + CO reaction system. J. Catal. **1994**, *148*, 697-708.

[71] Belton, N. D.; DiMaggio, L. D. C.; Schmieg, J. S.; Simon Ng, K. Y. Reaction of coadsorbed nitric oxide and nitrogen Atoms on Rh(111). J. Catal. **1995**, *157*, 559-568.

[72] Charles, H. F. P.; Belton, N. D.; Schemieg, J. S. Structure sensitive selectivty of the NO - CO reaction over Rh (110) and Rh (111). J. Catal. **1995**, *155*, 204-218.

[73] Zhdanov, V. P.; Kasemo, B. Steady-state kinetics of the NO-CO reaction on Rh(111): extrapolation from 0.001 to 1 bar. Catal. Lett. **1996**, *40* (3), 197-202.

[74] Permana, H.; Simon Ng, K. Y.; Peden, H. F. C.; Schmieg, J. S.; Lambert, K. D.; Belton, N. D. Adsorbed species and reaction rates for NO–CO over Rh(111). J. Catal. **1996**, *164*, 194–206.

[75] Zhdanov, V. P. Does the N_2O–CO subreaction play an important role in the NO–CO reaction on Rh? J. Catal. **1996**, *162*, 147-148.

[76] McCabe, R. W.; Wong, C. Steady-state kinetics of the carbon monoxide-nitrous oxide reaction over an alumina-supported rhodium catalyst. J. Catal. **1990**, *121* (2), 422-431.

[77] Permana, H.; Simon Ng, K. Y.; Peden, H. F. C.; Schmieg, J. S.; Lambert, K. D.; Belton, N. D. Adsorbed species and reaction rates for NO-CO-O_2 over Rh (111). Catal. Lett. **1997**, *47*, 5-15.

[78] Novak, E.; Sprinceana, D.; Solymosi, F. CO-induced structural changes of supported Rh promoted by NO. Appl. Catal., A **1997**, *149*, 89-101.

[79] Teuvo, M.; Ahola, J.; Salmi, T.; Haario, H.; Harkonen, M.; Luoma, M.; Pohjola, J. V. Investigation of CO oxidation and NO reduction on three-way monolith catalysts with transient response techniques. Appl. Catal., B **1997**, *12*, 287-308.

[80] Zhdanov, V. P.; Kasemo, B. Mechansim and kinetics of the NO - CO reaction on Rh. Surf. Sci. Rep. **1997**, *29*, 31-90.

[81] Chuang, S. C. S.; Tan, C. D. Mechanistic studies of the NO–CO Reaction on Rh/Al_2O_3 under net-oxidizing conditions. J. Catal. **1998**, *173*, 95-104.

[82] Kiss, J.; Solymosi, F. The effect of adsorbed oxygen on the stability of NCO on Rh(111) studied by Reflection Absorption Infrared Spectroscopy. J. Catal. **1998**, *179*, 277-282.

[83] Herman, G. S.; Peden, C. H. F.; Schmieg, S. J.; Belton, D. N. A comparison of the NO–CO reaction over Rh(100), Rh(110) and Rh(111). Catal. Lett. **1999**, *62*, 131-138.

[84] Chuang, S. C. S.; Almusaiteer, A. K.; Tan, C. Reactivity of $Rh^{+}(CO)_2$ during the NO–CO and $CO–O_2$ reactions over Rh/Al_2O_3. J. Catal. **2000**, *189*, 247–252.

[85] Bustos, V.; Gopinath, C. S.; Unac, R.; Zaera, F.; Zgrablich, G. Lattice-gas study of the kinetics of catalytic conversion of NO–CO mixtures on rhodium surfaces. J. Chem. Phys. **2001**, *114* (24), 10927-10931.

[86] Harmsen, J. M. A.; Hoebink, J. H. B. J.; Schouten, J. C. NO reduction by CO over automotive exhaust gas catalysts in the presence of O_2. Catal. Lett. **2001**, *71* (1-2), 81-91.

[87] Zaera, F.; Gopinath, S. C. NO + CO + O_2 reaction kinetics on Rh(111): A molecular beam study. J. Catal. **2001**, *200*, 270-287.

[88] Baumer, M.; Mavrikakis, M.; Freund, H. J.; Norskov, J. K. Structure sensitivity of CO dissociation of Rh surfaces. Catal. Lett. **2002**, *81* (3-4), 153-157.

[89] Loffreda, D.; Simon, D.; Sautet, P. Structure sensitivity for NO dissociation on palladium and rhodium surfaces. J. Catal. **2003**, *213*, 211-225.

[90] Avalos, L. A.; Bustos, V.; Unac, R.; Zaera, F.; Zgrablich, G. Toward a realistic model for the kinetics of the NO+CO reaction on rhodium surfaces. J. Mol. Catal. A: Chem. **2005**, *228*, 89-95.

[91] Granger, P.; Dujardin, C.; Paul, J. F.; Leclercq, G. An overview of kinetic and spectroscopic investigations on three-way catalysts: mechanistic aspects of the CO+NO and $CO+N_2O$ reactions. J. Mol. Cat. A: Chem. **2005**, *228*, 241-253.

[92] Ricart, J. M.; Ample, F.; Clotet, A.; Curulla, D.; Niemantsverdriet, J. W.; Paul, J. F.; Pérez-Ramírez, J. Structure and catalytic processes of N-containing species on Rh(111) from first principles. J. Catal. **2005**, *232*, 179–185.

[93] Dent, J. A.; Evans, J.; Fiddy, G. S.; Jyoti, B.; Newton, A. M.; Tromp, M. Rhodium dispersion during NO/CO Conversions. Angew. Chem. Int. Ed. **2007**, *46*, 5356 – 5358.

[94] Na-Ranong, D.; Niiyama, H.; Aida, T. Application of periodic operation to kinetic study for NO–CO reaction over Pt/Al_2O_3. Appl .Catal., A **2002**, *234*, 103-110.

[95] Gopinath, S. C.; Zaera, F. Transient kinetics during the Isothermal reduction of NO by CO on Rh(111) as studied with effusive collimated molecular beams. J. Phys. Chem. B **2000**, *104*, 3194-3203.

[96] Bowker, M.; Guo, Q.; Joyner, R. CO and O_2 adsorption on Rh(110). Surf. Sci. **1991**, *253* (1-3), 33-43.

[97] Matsushima, T.; Imamura, K.; Horino, H.; A. Hiratsuka; Ma, Y. S.; Rzeznicka, I. I.; Nakagoe, O. Inclined N_2 desorption in N_2O decomposition on Rh(1 1 0). Appl. Surf. Sci. **2005**, *244* (1-4), 141-144.

[98] Burch, R.; Coleman, M. D. An Investigation of promoter effects in the reduction of NO by H_2 under lean-burn conditions. J. Catal. **2002**, *208* (2), 435-447.

[99] Borg, H. J.; Reijerse, J. F. C.; Van Santen, R. A.; Niemantsverdriet, J. W. The dissociation kinetics of NO on Rh(111) as studied by temperature programmed static secondary ion mass spectrometry and desorption. J. Chem. Phys. **1994**, *101* (11), 10052.

[100] Araya, P.; Cortes, J. Some aspects of the NO reduction reaction over rhodium catalysts. J. Chem. Soc., Faraday Trans. **1997**, *93* (4), 639-642.

[101] EPA. National summary of nitrogen oxides emissions. **2008** U.S. EPA

[102] UNEP/DEWA/GRID-Europe. Emission Database for global atmospheric research. **2010** UNEP/DEWA/GRID- Europe

[103] L.Unland, M. Isocyanate intermediates in the reaction NO+CO over a Pt/Al_2O_3 catalyst. J. Phys. Chem. **1973**, *77* (16), 1952-1957.

[104] Kobylinksi, T. P.; Taylor, B. W. The catalytic chemistry of nitric oxide II. Reduction of nitric oxide over noble metal catalysts. J. Catal. **1974**, *33*, 376-384.

[105] Lambert, R. M.; Comrie, C. M. The oxidation of CO by NO on Pt_{111} and Pt_{110}. Surf. Sci **1974**, *46* (1), 61-80.

[106] Niiyama, H.; Tanaka, M.; Iida, H.; Echigoya, E. Infrared studies of the isocyanate species formed in the reaction of NO with CO over Pt and Rh. Bull. Chem. Soc. Jpn. **1976**, *49* (8), 2047-2050.

[107] Solymosi, F.; Sarkany, J.; Schauer, A. Study of the formation of Isocyanate surface complexes on Pt/Al_2O_3 catalysts. J. Catal. **1977**, *46*, 297-307.

[108] Solymosi, F.; Volgyesi, L.; Sarkany, J. The Effect of the support on the formation and stability of surface isocyanate on platinum. J. Catal. **1978**, *54* (336-344), 336.

[109] Charles C. Chang; Hegedus, L. L. Surface Reactions of NO, CO and O_2 near the stoichiometric point 1.Pt-Alumina. J. Catal. **1979**, *57*, 361-371.

[110] Hegedus, L.; Chang, C. C.; McEwen, D. J.; Sloan, E. M. Response of catalyst surface concentrations to forced concentration oscillations in the gas phase. The NO, CO, O_2 system over Pt-Alumina. Ind. Eng. Chem. Fund. **1980**, *19* (4), 367-373.

[111] Singh-Boparai, S. P.; King, D. A. Molecular beam study of the catalytic reaction between NO and CO on Pt_{001}. Vide, Les Couches Minces **1980**, *201*, 403-407.

[112] Gorte, R. J.; Schmidt, L. D. Interactions between NO and CO on Pt_{111}. Surf. Sci. **1981**, *111* (2), 260-278.

[113] Banholzer, W. F.; Masel, R. I. A reflection-absorption infrared study of carbon monoxide and nitric oxide adsorption on $platinum_{100}$. Surf. Sci **1984**, *137* (1), 339-360.

[114] Lesley, M. W.; Schmidt, L. D. The NO + CO reaction on Pt_{100}. Surf. Sci **1985**, *155* (1), 215-240.

[115] Barteau, M. A.; Ko, E. I.; Madix, R. J. The adsorption of CO, O_2 and H_2 on Pt_{100}. Surf. Sci **1981**, *102* (1), 99-117.

[116] Schwartz, S. B.; Schmidt, L. D. Is there a single mechanism of catalytic rate oscillations on Pt. Surf. Sci **1987**, *183*, 269-278.

[117] Muraki, H.; Fujitani, Y. NO Reduction by CO over noble-metal catalysts under cycled feedstreams. Ind. Eng. Chem. Prod. Res. Dev. **1986**, *25*, 414-419.

[118] Matyshak, B. A. Interaction of carbon monoxide and nitric oxide in the presence of oxygen on a supported platinum catalyst. Kinetika i Kataliz **1988**, *29* (6), 1382-1389.

[119] Schwartz, S. B.; Schmidt, L. D. The NO+CO reaction on clean Pt_{100}: Multiple steady states and oscillations. Surf. Sci **1988**, *206* (1-2), 169-186.

[120] Banse, B. A.; Wickham, D. T.; Koel, B. E. Transient kinetics studies of the catalytic reduction of NO by CO on Platinum. J. Catal. **1989**, *119* (1), 238-248.

[121] Fink, T.; Dath, J. P.; Bassett, M. R.; Imbihl, R.; Ertl, G. The mechansim of the explosive NO + CO reaction on Pt_{100}: Experiments and mathematical modeling. Surf. Sci **1991**, *245*, 96-110.

[122] Yaldram, K.; Khan, M. A. NO-CO reaction on square and hexagonal surfaces: A monte carlo simulation. J. Catal. **1991**, *131*, 369-377.

[123] Fink, T.; Krischer, K.; Imbihl, R. Kinetic oscillations in the Pt_{100} NO+CO system: Bifurcation analysis. J. Vac. Sci. Technol. A **1992**, *10* (4).

[124] Scharpf, E. W.; Benziger, J. B. Kinetics of the CO/NO surface reactions by the direct observation of the adsorbed species. J. Catal. **1992**, *136* (342-360), 342.

[125] Klein, R. L.; Schwartz, S.; Schmidt, L. D. Kinetics of the NO+CO reaction on clean Pt: Steady-state rates. J. Phys. Chem. **1985**, *89* (23), 4908-4914.

[126] Uchida, Y.; Imbihl, R.; Lehmpfuhl, G. Surface topographical changes on Pt_{100} and Pt_{111} in the NO + CO reaction: A reflection electron microscopy study. Surf. Sci **1992**, *275*, 253-264.

[127] Vesser, G.; Imbihl, R. Spatial pattern formation in the oscillatory NO+CO reaction on a Pt_{100} surface and its vicinal orientations. J. Chem. Phys **1992**, *96* (9), 7155-7164.

[128] David, A. K. Nonlinear effects in adsorption and reaction dynamics at surfaces: Kinetic oscillations under scrutiny. Surf. Rev. Lett. **1994**, *1* (4), 435-442.

[129] Meng, B.; Weinberg, H. W.; Evans, J. W. Lattice-gas model mimicking the NO+CO reaction on Pt_{100}. J. Chem. Phys. **1994**, *101* (4), 3234-3243.

[130] Zagatta, G.; Muller, H.; Wehmeyer, O.; Brandt, M.; Bowering, N.; Heinzmann, U. Quantitative mass analysis of N_2, CO_2 and N_2O reaction products in the NO-CO reaction at Pt_{100}. Surf. Sci **1994**, *307-309*, 199-204.

[131] Vesser, G.; Imbihl, R. Synchronization and spatiotemporal self-organization in the NO+CO reaction on Pt_{100}. I. Unsynchronized oscillations on the 1x1 substrate. J. Chem. Phys **1994**, *100* (11), 8483-8491.

[132] D.Graham, M.; G. Kevrekidis, I. Dynamics of concentration patterns of the NO+CO reaction on Pt: Analysis with the Karhunen-Loeve decomposition. Chaos, Solitons & Fractals **1995**, *5* (10), 1817-1831.

[133] Svoronos, D. G.; Grigoropoulou, H. P.; Philippopoulos, C. J. Effect of Pt/Al_2O_3 catalyst preparation conditions upon its activity in nitric oxide reduction. Appl. Catal., B **1995**, *5*, 319-328.

[134] Mergler, Y. J.; Nieuwenhuys, B. E. NO Reduction by CO over Pt/Al_2O_3 and $Pt/CeO_x/Al_2O_3$: Oscillations and deactivation. J. Catal. **1996**, *161*, 292-303.

[135] Sadhankar, R. R.; Lynch, D. T. Slow convergence to cycle-invariance during forced oscillations of the NO+CO reaction over a Pt catalyst. Chem. Eng. Sci. **1996**, *51* (10), 2061-2068.

[136] Sadhankar, R. R.; Lynch, D. T. NO reduction by CO over a Pt/Al_2O_3 Catalyst: Reaction kinetics and experimental bifurcation behavior. Ind. Eng. Chem. Res. **1997**, *36*, 4609-4619.

[137] Miners, J. H.; Martin, R.; Gardner, P.; Nalezinski, R.; Bradshaw, A. M. Monitoring adsorbed species during oscillatory reactions using vibrational spectroscopy. Surf. Sci. **1997**, *377-379*, 791-795.

[138] Granger, P.; Dathy, C.; Lecomte, J. J.; Leclercq, L.; Prigent, M.; Mabilon, G.; Leclercq, G. Kinetics of the NO and CO reaction over platinum catalysts I. Influence of the support. J. Catal. **1998**, *173*, 304-314.

[139] Frank, B.; Renken, A. Kinetics and deactivation of the NO reduction by CO on Pt-supported catalysts. Chem. Eng. Technol. **1998**, *21* (6), 490-495.

[140] Miners, J. H.; Gardner, P. The defect-mediated mechanism of the high-temperature oscillatory NO + CO reaction on Pt_{100} as revealed by real-time in-situ vibrational spectroscopy. J. Phys. Chem. B **2000**, *104*, 10265-10270.

[141] Takeshima, S.; Ikeda, M.; Nagata, H.; Kishida, M.; Wakabayashi, K. NO-CO reaction over Pt/Al_2O_3 catalysts prepared by microemulsion method. J. Jpn. Pet. Inst. **1999**, *42* (3), 145-150.

[142] Granger, P.; Malfoy, P.; Leclercq, L.; Esteves, P.; Leclercq, G. Kinetics of the CO + N_2O reaction over noble metals I. Pt/Al_2O_3. J. Catal. **1999**, *187*, 321-331.

[143] Aida, T.; Na-Ranong, D.; Kobayashi, R.; Niiyama, H. Effect of diffusion and adsorption-desorption on periodic operation performance of NO-CO reaction over supported noble metal catalysts. Chem. Eng. Sci. **1999**, *54*, 4449-4457.

[144] Akama, H.; Matsushita, K. Recent lean NO_x catalyst technologies for automobile exhaust control. Catal. Surv. Jpn. **1999**, *3*, 139-146.

[145] Hartmann, N.; Kevrekidis, Y.; Imbihl, R. Pattern formation in restricted geometries: The NO + CO reaction on Pt_{100}. J. Chem. Phys. **2000**, *112* (15), 6795-6804.

[146] Bourane, A.; Dulaurent, O.; Salasc, S.; Sarda, C.; Bouly, C.; Bianchi, D. Heats of adsorption of linear NO species on a Pt/Al_2O_3 catalyst using in situ infrared spectroscopy under adsorption equilibrium. J. Catal. **2001**, *204*, 77-88.

[147] Ikeda, M.; Tago, T.; Kishida, M.; Wakabayashi, K. Thermal stability of Pt particles of Pt/Al_2O_3 catalysts prepared using microemulsion and catalytic activity in NO-CO reaction. Catal. Commun. **2001**, *2*, 261-267.

[148] Granger, P.; Praliaud, H.; Billy, J.; Leclercq, L.; Leclercq, G. Infrared investigation of the transformation of NO over supported Pt- and Rh-based three-way catalysts. Surf. Inter. Anal. **2002**, *34*, 92-96.

[149] Na-Ranong, D.; Aida, T.; Niiyama, H. Application of periodic operation to kinetic study for NO-CO reaction over Pt/Al_2O_3. Appl. Catal. A. **2002**, *234*, 103-110.

[150] P.Zhdanov, V. Oscillations in the NO-CO reaction on Pt_{100}: NO decompostion on island boundaries Catal. Lett. **2002**, *84* (3-4), 147-152.

[151] Zhdanov, V. P. Monte Carlo simulations of oscillations, chaos and pattern formation in heterogeneous catalytic reactions. Surf. Sci. Rep. **2002**, *45*, 231-326.

[152] Yu-Bing, J.; Shou-jia, S. Kinetic modelling of NO + CO reaction on $Pt/MoO_x/Al_2O_3$ catalyst. Journal of Harbin Institute of Technology **2003**, *10* (2), 151-153.

[153] Ohno, Y.; Sarawut, P.; Horino, H.; Kobal, I.; Hiratsuka, A.; Matsushima, T. Product desorption dynamics in explosive NO+CO reaction on Pt_{100}. Chem. Phys. Lett. **2003**, *373*, 161-166.

[154] Rienks, E. D. L.; Bakker, J. W.; Baraldi, A.; Carabineiro, S. A. C.; Lizzit, S.; Weststrate, C. J.; Nieuwenhuys, B. E. Synchrotron XPS study of the NO-CO reaction on Pt100. Surf. Sci **2003**, *532*, 120-125.

[155] Makeev, A. G.; Kevrekidis, I. G. Equation-free multiscale computations for a lattice-gas model: coarse-grained bifurcation analysis of the NO+CO reaction on Pt_{100}. Chem. Eng. Sci. **2004**, *59*, 1733-1743.

[156] Miners, J. H.; Gardner, P.; Bradshaw, A. M.; Woodruff, D. P. A real-time vibrational spectroscopic investigation of the low-temperature oscillatory regime of the reaction of NO with CO on Pt_{100}. J. Phys. Chem. B **2004**, *108*, 1708-1718.

[157] Alas, S. J.; Cordero, S.; Kornhauser, I.; Zgrablich, G. Kinetic oscillations in the NO+CO reaction on the Pt_{100} surface: An alternative reaction mechanism. J. Chem. Phys. **2005**, *122*, 144705-144712.

[158] Horino, H.; Matsushima, T. Inclined N_2 desorption in a steady-state NO + CO reaction on Pt_{100}. J. Phys. Chem. B **2005**, *109*, 675-677.

[159] Alas, S. J.; Zgrablich, G. Study of oscillations and pattern formation in the NO + CO reaction on Pt_{100} surfaces through dynamic Monte Carlo simulation: Toward a realistic model. J. Phys. Chem. B **2006**, *110*, 9499-9510.

[160] Derrouiche, S.; Bianchi, D. Modifications of the elementary steps involved in the O_2-oxidation of the adsorbed CO species over Pt/Al_2O_3 by co-adsorbed NO species. J. Catal. **2006**, *242*, 172-183.

[161] Liu, J.-j.; Hua, D.-y.; Jiang, L.-l. Effect of surface impurities on oscillation in $NO+CO/Pt_{100}$ reaction system. Chin. J. Chem. Phys. **2007**, *20* (3), 279-284.

[162] Mantri, D.; Mehta, V.; Aghalayam, P. Bifurcation Analysis on Pt and Ir for the reduction of NO by CO. Can. J. Chem. Eng. **2007**, *85*, 333-401.

[163] Alas, S. J.; Vicente, L. Study of the explosive NO+CO reaction on a Pt_{100} surface by dynamic Monte Carlo simulation. J. of Mol. Cat. A:Chem **2008**, *281*, 24-34.

[164] Voltz, S. E.; Morgan, C. R.; Liederman, D.; Jacob, S. M. Kinetic study of carbon monoxide and propylene oxidation on platinum catalysts. Ind. Eng. Chem. Prod. Res. Develop. **1973**, *12* (4), 294-301.

[165] Miners, J. H.; Bradshaw, A. M.; Gardner, P. Direct observation of surface isocyanate (NCO) formation during the CO + NO reaction on Pt_{100}. Phys. Chem. Chem. Phys. **1999**, *1*, 4909-4912.

[166] Epling, W. S.; Campbell, L. E.; Yezerets, A.; Currier, N. W.; Parks, E. J. Overview of the fundamental reactions and degradation mechanisms of NOx storage/reduction catalysts. Catal. Rev. Sci. Eng. **2004**, *46* (2), 163-245.

[167] Westerberg, B.; Fridell, E. A transient FTIR study of species formed during NO_x storage in the $Pt/BaO/Al_2O_3$ system. Journal of Molecular Catalysis A: Chemical **2001**, *165*, 249-263.

[168] Olsson, L.; Fridell, E. The influence of Pt oxide formation and Pt dispersion on the reactions over Pt/Al_2O_3 and $Pt/BaO/Al_2O_3$. J. Catal. **2002**, *210*, 340-353.

[169] Ergun, S. Fluid flow through packed columns. Chem. Eng. Proc. **1952**, *4* (2), 89.

[170] Finlayson, B. A. Packed bed reactor analysis by orthogonal collocation. Chem. Eng. Sci. **1971**, *26*, 1081-1091.

[171] Aris, R. On the dispersion of a solute in a fluid flowing through a tube. Proc. Roy. Soc. Lond. A **1956**, *235*, 67.

[172] Taylor, G. I. Dispersion of soluble matter in solvent flowing slowly through a tube. Proc. Roy. Soc. Lond. A **1953**, *219*, 186.

[173] McGuire, M. L.; Leon, L. On the stability of a detailed packed-bed reactor. AIChE **1965**, *11* (1), 85-97.

[174] Depcik, C.; Kobiera, A.; Assanis, D. Influence of density variation on one-dimensional modeling of exhaust assisted catalytic fuel reforming. Heat Transfer Engineering **2010**, *31* (13), 1098-1113.

[175] Wicke, E.; Kallenbach, R. kolloid Z **1941**, *135*.

[176] Eigenberger, G. On the dynamic behavior of the catalytic fixed-bed reactor in the region of multiple steady states Chem. Eng. Sci. **1972**, *27*, 1909-1915.

[177] Robertson, G. Description and verification of a transient model for packed-bed catalytic converters. AIChE **1980**, *76* (199), 335-354.

[178] Oh, S. H.; Cavendish, J. C.; Hegedus, L. L. Mathematical modeling of catalytic converter lightoff: Single-pellet studies. A.I.Ch.E. Journal **1980**, *26* (6), 935-943.

[179] Younis, L. B. Hydrogen oxidation within catalytic packed bed reactor. J. of Energy Instit. **2006**, *79* (4), 222-229.

[180] Krupiczka, R. Analysis of effective thermal conductivity of granular materials. Chimie & Industrie, **1966**, *95* (6), 1393-1396.

[181] Omata, H.; Brown, L. F. Using the dusty gas diffussion equation in catalyst pores smaller than 50^{o}A radius. AIChE **1972**, *18*, 967.

[182] Carberry, J. J.; Arvind, V. Chemical Reaction and Reactor Engineering; Marcel Dekker: Berkeley, California, **1987**; 1068 pp.

[183] Epstein, N. On tortuosity and the tortuosity factor in flow and diffusion through porous media. Chem. Eng. Sci. **1989**, *44* (3), 777-779.

[184] Mueller, G. Prediction of radial porosity distributions in randomely packed fixed beds of uniformly sized spheres in cylindrical containers. Chem. Eng. Sci. **1991**, *46* (2), 706-710.

[185] Sharma, R. K.; Cressweel, D. L.; Newson, E. J. Effective diffusion coefficients and tortuosity factors for commercial catalysts. Ind. Eng. Chem. **1991**, *30*, 1428-1433.

[186] Johnson, M. F. L.; Stewart, W. E. Pore structure and gaseous diffusion in solid catalysts. J. Catal. **1956**, *4*, 248-252.

[187] Evans, R. B.; Watson, G. M. Gaseous diffusion in porus media at uniform pressure. J. Chem. Phys. **1961**, *35* (6), 2076-2083.

[188] Nield, D. A.; Bejan, A. Convection in Porous Media; Springer: New York, **2006**; pp.

[189] Yagi, S.; Kunii, S.; Wakao, N. Effective thermal conductivites in packed beds. AIChE **1960**, *6*, 543-547.

[190] Vortmeyer, D.; Schaeffer, R. J. Equivalence of one- and two- phase models for heat transfer processes in packed bed: 1-D theory. Chem. Engng. Sci. **1974**, *29*, 485.

[191] Dixon, A.; Cresswell, D. L. Theoretical prediction of effective heat transfer parameters in packed beds. AIChE **1979**, *25* (4), 663-678.

[192] Depcik, C.; van Leer, B.; Assanis, D. The numerical simulation of variable-property reacting-gas dynamics: New insights and validation. Numerical Heat Transfer, Part A **2005**, *47* (1), 27-56.

[193] Nield, D. A.; Bejan, A. Convection in porous media; Springer-Verlag: New York, NY, **2006**; 290 pp.

[194] Kuo, J. C.; Morgan, C. R.; Lassen, H. G. Mathematical modeling of CO and HC catalytic converter systems. SAE Paper 710289 **1971**.

[195] Panton, R. L. Incompressible Flow; John Wiley & Sons: New York, NY, **1984**; 814 pp.

[196] Byrne, H.; Norbury, J. Mathematical Modelling of Catalytic Converters. Math. Engng. Ind. **1993**, *4* (1), 27-48.

[197] Venderbosch, R. H.; Prins, W.; Van Swaaij, W. P. M. Platinum catalyzed oxidation of carbon monoxide as a model reaction in mass transfer measurements. Chem. Eng. Sci **1998**, *53* (19), 12.

[198] Hayes, R. E.; Kolaczkowski, S. T. Introduction to catalytic combustion; CRC Press, **1997**; 645 pp.

[199] Gorring, R. L.; Churchill, S. W. Chem. Eng. Prog. **1961**, *57*, 53.

[200] Gopalarathnam, C. D.; Hoelscher, H. E.; Laddha, G. S. Effective thermal conductivity in packed beds. AIChE **1961**, *7*, 249.

[201] Fuentes, J.; Pironti, F.; Lopez, A. L. Effective thermal conductivity in a radial-flow packed-bed reactor. Int. J. Thermophys. **1998**, *19* (3), 781-792.

[202] Liu, S. L.; Amundson, N. R. Stability of adiabatic packed bed reactors. Industrial and Engineering Chemistry - Fundamentals **1962**, *1* (3), 200-208.

[203] Depcik, C.; Assanis, D. Simulating area conservation and the gas-wall interface for one-dimensional based diesel particulate filter models. ASME Journal of Engineering for Gas Turbines and Power **2008**, *130* (6), 062807/1-18

[204] Li, C.-H.; Finlayson, B. A. Heat transfer in packed beds. Chem. Eng. Sci **1977**, *32* (9), 1055-1066.

[205] Wijngaarden, R. J.; Westerterp, K. R. Pellet heat transfer coefficients in packed beds: Global and local values. Chem. Eng. Technol. **1993**, *16*, 363-372.

[206] Waede, H. Analysis of transient models for tubular reactors by orthogonal collocation. ibid **1971**, *26*, 1555-1569.

[207] Belfiore, A. L. Transport Phenomena for Chemical Reactor Design; Wiley, **2003**; 884 pp.

[208] Hirschfelder, J. O.; Curtiss, C. F.; Bird, R. B. Molecular Theory of Gases and Liquids; John Wiley and Sons: New York, NY, **1954**; 1280 pp.

[209] Kee, R. J.; Coltrin, M. E.; Glarborg, P. Chemically Reacting Flow: Theory and Practice; John Wiley & Sons, Inc.: Hoboken, New Jersey, **2003**; 928 pp.

[210] Cussler, E. L. Diffusion Mass Transfer in Fluid Systems; Cambridge, **1997**; pp.

[211] Darling, C. L.; Schlegel, H. B. Dipole moments, polarizabilities, and infrared intensities calculated with electric field dependent functions. Journal of Physical Chemistry **1994**, *98* (23), 5855-61.

[212] Ladd, M.; Ladd, M. F. C. Introduction to physical chemistry; Cambridge University Press: Cambridge, **1998**; 536 pp.

[213] Bird, R. B.; Stewart, W. E.; Lightfoot, E. N. Transport Phenomena; John Wiley & Sons, Inc.: Newyork, **1960**; 912 pp.

[214] Schettler, P. D.; Fuller, E. N.; Giddings, J. C. A new method for prediction of binary gas-phase diffusion coefficients. Ind. Eng. Chem. **1966**, *58*, 1-19.

[215] Knudsen, C. W.; Roberts, G. W.; Satterfield, C. N. Effect of geometry on catalyst effectiveness factor. Ind. Eng. Chem. Funda. **1966**, *5* (3), 325-326.

[216] Marvin, F. L.; Warren, E. S. Pore Structure and gaseous diffusion in solid catalysts. J. Catal. **1965**, *4* (2), 248-254.

[217] Beek, J. Measurements of gaseous diffusion through porous materials. Indus. Eng. Chem. Proc. Des. Dev. **1962**, *1* (1), 45-49.

[218] Wakao.N; Smith, J. M. Diffusion in Catalyst pellets. Chem. Eng. Sci. **1962**, *17* (11), 825-834.

[219] Carman, P. C. Flow of gases through porous media; Academic Press **1956**; 182 pp.

[220] Dullien, F. A. L. Porous media: Fluid transport and pore structure; Academic Press: New York, **1979**; 574 pp.

[221] Kalluri, R. R.; Cahela, D. R.; Tatarchuk, B. J. Comparative heterogeneous contacting efficiency in fixed bed reactors: Opportunities for new microstructured systems. Appl. Catal. B: Environ **2009**, *90*, 507-515.

[222] Satterfield, C. N. Mass transfer in Heterogeneous Catalysis; MIT press: Cambridge, **1970**; pp.

[223] Ho, F. G.; Strieder, W. Numerical evaluation of the porous medium effective diffusivity between the Knudsen and continuum limits. . J. Chem. Phys. **1980**, *73* (12), 6296-6300.

[224] Wheeler, A. Reaction rates and selectivity in catalyst pores. Advances in Catalysis **1951**, *3*, 249-327.

[225] Sharma, R. K.; Cresswell, D. L.; Newson, E. J. Effective diffusion coefficients and tortuosity factors for commercial catalysts. Industrial & Engineering Chemistry Research **1991**, *30* (7), 1428-1433.

[226] Hayes, R. E.; Kolaczkowski, S. T.; Li, P. K.; Awdry, C. S. Evaluating the effective diffusivity of methane in the washcoat of a honeycomb monolith. Applied Catalysis B: Environmental **2000**, *25* (2-3), 93-104.

[227] Kolaczkowski, S. T. Measurement of effective diffusivity in catalyst-coated monoliths. Catalysis Today **2003**, *83* (1-4), 85-95.

[228] Hayes, R. E.; Kolaczkowski, S. T.; Li, P. K. C.; Awdry, S. The palladium catalysed oxidation of methane: Reaction kinetics and the effect of diffusion barriers. Chemical Engineering Science **2001**, *56* (16), 4815-4835.

[229] Tsotsas, E.; Schlunder, E. U. Heat transfer in packed beds with fluid flow: Remarks on the meaning and the calculation of a heat transfer coefficient at the wall. Chem. Eng. Sci. **1990**, *45* (4), 819-873.

[230] Aris, R.; Amundson, N. R. Some remarks on longitudinal mixing or diffusion in fixed beds. AIChE **1957**, *3* (6), 280-282.

[231] Zehner, P.; Schlunder, E. U. Thermal conductivity of packings at moderate temperatures. Chemie-Ingr-Technik. **1970**, *42* (14), 933-941.

[232] Bosanquet, C. H. The diffusion at a front in gas chromatography. Gas Chromatog. Proc. Symp. **1958**, 107-114.

[233] Wicke, E.; Kallenbach, R. D. Counter diffusion through porous pellet. Kolloid Z **1941**, *97*, 135-138.

[234] Plautz, D.; Johnstone, H. F. Heat and mass transfer in packed beds. AIChE **1955**, *1* (2), 193-200.

[235] Yagi, S.; Kunii, D. Effective thermal conductivities in packed beds. AIChE **1957**, *3*, 373.

[236] Hsu, C. T.; Cheng, P.; Wong, K. W. Modified Zehner-Schlunder models for stagnant thermal conductivity of porous medium. Int. J. Heat and Mass Trans. **1994**, *37*, 2751-2759.

[237] Kulkarni, B. D.; Doraiswamy, L. K. Estimation of effective transport properties in packed bed reactors. Catal. Rev. Sci. Eng. **1980**, *22* (3), 431-483.

[238] Opris, C. N.; Johnson, J. H. A 2-D Computational model describing the heat transfer, reaction kinetics and regeneration characteristics of a ceramic diesel particulate trap. SAE **1998**, *980546*.

[239] Elsari, M.; Hughes, R. Axial effective thermal conductivities of packed beds. Appl. Thermal. Eng. **2002**, *22*, 1969-1980.

[240] Modest, M. F. Radiative heat transfer; McGrawHill: New York, **1993**; 860 pp.

[241] Tavman, I. H. Effective thermal conductivity of granular porous materials. Int. Comm. Heat Mass Transfer **1996**, *23* (2), 169-176.

[242] Hoffman, J. D. Numerical Methods for Engineers and Scientists; McGraw-Hill, Inc.: New York, **1992**; 704 pp.

[243] Khanna, R.; Seinfeld, J. H. Mathematical modeling of packed bed reactors: numerical solutions and control model development. Adv. Chem. Eng. **1987**, *13*, 113-193.

[244] Tannehill, J. C.; Anderson, D. A.; Pletcher, R. H. Computational fluid mechanics and heat transfer; Taylor & Francis: Washington, D.C, **1997**; 803 pp.

[245] Hoffman, J. D. Numerical Methods for Engineers and Scientists; McGraw-Hill, Inc.: New York, **1992**; pp.

[246] Balakotaiah, V.; Dommeti, S. M. S. Effective models for packed-bed catalytic reactors. Chem. Eng. Sci. **1999**, *54*, 1621-1638.

[247] Granger, P.; Lecomte, J. J.; Leclercq, L.; Leclercq, G. An attempt at modelling the activity of Pt-Rh/Al_2O_3 three-way catalysts in the CO + NO reaction. Appl. Catal. A **2001**, *208*, 369-380.

[248] Granger, P.; Leclercq, G.; Lecomte, J. J.; Dathy, C.; Leclercq, L. Kinetics of the CO+NO reaction over rhodium and platinum–rhodium on alumina II. Effect of Rh incorporation to Pt. J. Catal. **1998**, *175*, 194-203.

[249] Granger, P.; Lecomte, J. J.; Leclercq, L.; Leclercq, G. Modelling study of the temperature-programmed conversion curves of NO reduction by CO over supported Pt- and Rh-based catalysts. Top. in Catal. **2001**, *16/17* (1-4), 349-355.

[250] Granger, P.; Malfory, P.; Leclercq, G. Kinetics of the $CO+N_2O$ reaction over noble metals II. Rh/Al_2O_3 and $Pt–Rh/Al_2O_3$. J. Catal. **2004**, *223*, 142-151.

[251] Kee, R. J.; Dixon, L. G.; Warantz, J.; Coltrin, M. E.; Miller, J. A.; Moffat, H. K. In *CHEMKIN Collection*; Design, R., Ed.; Reaction Design, 2003, 66 pp.

[252] Borkink, J. G. H.; Westerterp, K. R. Determination of effective heat transport coefficients for wall-cooled packed beds. Chem. Eng. Sci. **1992**, *47* (9-11), 2237-42.

[253] Shampine, L. F. Numerical Solution of Ordinary Differential Equations; Chapman & Hall: New York, **1994**; 632 pp.

[254] Campbell, T.; Newton, M. A.; Boyd, V.; Lee, D. F.; Evans, J. Effects of precursor and support variation in the performance of uranium oxide catalysts for CO oxidation and selective reduction of NO. J. Mol. Catal. A: Chem. **2006**, *245* (1-2), 62-68.

[255] Oh, S. H.; Fisher, G. B.; Carpenter, J. E.; Goodman, D. W. Comparative kinetic studies of CO---O2 and CO---NO reactions over single crystal and supported rhodium catalysts. Journal of Catalysis **1986**, *100* (2), 360-376.